Fall 2018

Microstructural development and its effect on aqueous corrosion of a borosilicate glass ceramic for waste vitrification

Nicholas Stephen Roberts

Department:

Recommended Citation

Roberts, Nicholas Stephen, "Microstructural development and its effect on aqueous corrosion of a borosilicate glass ceramic for waste vitrification" (2018). *Masters Theses*. 7832.
https://scholarsmine.mst.edu/masters_theses/7832

MICROSTRUCTURAL DEVELOPMENT AND ITS EFFECT ON AQUEOUS CORROSION OF A BOROSILICATE GLASS CERAMIC FOR WASTE VITRIFICATION

by

NICHOLAS STEPHEN ROBERTS

A THESIS

presented to the faculty of the graduate school of the

MISSOURI UNIVERSITY OF SCIENCE AND TECHNOLOGY

in partial fulfillment of the requirements for the degree

MASTER OF SCIENCE

in

MATERIALS SCIENCE AND ENGINEERING

2018

Approved by

Richard K. Brow, Advisor
Jeffrey D. Smith
F. Scott Miller

PUBLICATION THESIS OPTION

This thesis consists of the following two articles which will be submitted for publication as follows:

Paper I: Pages 27- 86 are intended for submission to the *Journal of Nuclear Materials*.

Paper II: Pages 87 – 116 are intended for submission to the *Journal of Nuclear Materials*.

ABSTRACT

Waste loadings of reprocessed spent nuclear fuel vitrified into borosilicate glass can be increased by precipitating environmentally stable phases concentrated with waste components in a chemically stable glass matrix. The principal objective of this thesis was to characterize the development of crystalline powellite ($CaMoO_4$ and related phases) and oxyapatite ($Ca_2LN_8Si_6O_{26}$) in borosilicate glass-ceramics and to determine how the formation of those phases affected its chemical durability.

Borosilicate glasses provided by PNNL were re-melted and quenched at rates from over 300°C/s to ~0.05°C/s. Isothermal heat treatment experiments were conducted by quenching melts in a molten tin bath at various temperatures, holding for periods of time, and then quenching in a water bath. Analytical electron microscopy and x-ray diffraction provided information about the kinetics of the phase separation and crystallization processes responsible for microstructural development. Powellite and oxyapatite crystals formed during slower quench rates and longer isothermal times, and time-temperature-transformation (TTT) diagrams were developed from the latter experiments.

Corrosion tests were performed to understand how the individual phases in the glass-ceramic affect its overall chemical durability. Product consistency tests provided release rates of major elements from samples as a function of cooling rate, and atomic force microscopy and profilometry measurements of surface topology determined the relative corrosion rates of the residual glass and oxyapatite phases. Faster dissolution rates were measured from samples cooled more slowly and these were explained by the greater fractions of B_2O_3 in the residual glass phase after the formation of oxyapatite and powellite. Oxyapatite was found to be more durable than the residual glass.

ACKNOWLEDGMENTS

Firstly, I must thank Dr. Alexis Clare (Alfred University) for her suggestion to pursue a graduate degree at Missouri S&T, for without her advice I would not have been here. Secondly, I am very thankful for my advisor, Dr. Richard K. Brow, for not only providing me with everything I needed to succeed in this project but also for inspiring me about glass science and teaching me proper research practices and presentation skills. His leadership will drive me in future endeavors and I am forever grateful to have him as an advisor. I would also like to thank all funding partners. This work was supported by the Department of Energy and the Nuclear Energy University Program (Project 15-8112). I would like thank Jarrod Crum from Pacific Northwestern National Laboratories for providing materials and for discussing our results. In addition, I appreciate the support of the CGS Summer Graduate Research Fellowship program. I also need to thank my research partner, Paul Porter, for his contributions to this project. This work would also not have been accomplished without help and support from the Brow Research Group, including Jenhsien Hsu, Parker Freudenberger, Jincheng Bai, Eric Muskovin, and Han Zhang. Many members from the MSE department and the MRC at Missouri S&T, especially, but not limited to Dr. Jeffrey D. Smith, Dr. F. Scott Miller, Dr. Eric Bohannan, Dr. Clarissa Wisner, Jingjing Qing, Ron Haas, Todd Sanders, Derek Seymour, Chuang Qu, and Elizabeth Peterson, have been helpful in all aspects of this project. I would like to thank my parents, Julia and Andrew, and siblings, Jordan, Ashton, and Anika for their love and support from the beginning. Last, and not least, I appreciate the support from all my S&T friends, especially, Josephine Gass, Abhishek Singh, and the Miner rugby team.

TABLE OF CONTENTS

Page

PUBLICATION THESIS OPTION iii

ABSTRACT…… iv

ACKNOWLEDGMENTS v

LIST OF ILLUSTRATIONS x

LIST OF TABLES xiv

SECTION

1. INTRODUCTION 1

  1.1. BACKGROUND 1

  1.2. RADIOACTIVE WASTE 1

  1.3. BOROSILICATE GLASS-CERAMICS FOR WASTE VITRIFICATION 5

    1.3.1. Glass Structure. 7

    1.3.2. Glass-Crystal Transformations 10

    1.3.3. Glass-Crystal Transformations Experimental Methods 12

    1.3.4. JMAK Crystallization Model [23, 27-32]. 14

    1.3.5. Chemical Durability of Borosilicate Glasses. 17

    1.3.6. Chemical Durability Experimental Methods. 17

  1.4. BOROSILICATE GLASS-CERAMICS FOR IMMOBILIZING US COMMERCIAL REPROCESSED SNF 19

    1.4.1. Phase Development. 20

    1.4.2. Chemical Durability. 22

2. RESEARCH OBJECTIVE 25

PAPER

I. PHASE DEVELOPMENT IN A COMPLEX BOROSILICATE GLASS-CERAMIC WASTE FORM 27

ABSTRACT 27

1. INTRODUCTION 28

2. EXPERIMENTAL PROCEDURES 31

2.1. GLASS COMPOSITION 31

2.2. CONTINUOUS COOLING EXPERIMENTS - MELT QUENCHING TECHNIQUES 32

2.3. ISOTHERMAL EXPERIMENTS - MELT QUENCHING TECHNIQUES 35

2.4. SAMPLE CHARACTERIZATION 36

2.4.1. X-ray Diffraction. 36

2.4.2. Analytical Electron Microscopy. 37

2.4.3. Raman Spectroscopy. 39

2.4.4. Differential Thermal Analysis. 39

3. RESULTS AND DISCUSSION 39

3.1. SAMPLE OBSERVATIONS 39

3.2. TIME-TEMPERATURE PROFILES 40

3.3. PHASE IDENTIFICATION 42

3.3.1. Phases Identified in the Continuously Cooled Samples. 43

3.3.2. Phases Identified in the Isothermal Samples. 47

3.4. PHASE MORPHOLOGY AND COMPOSITION 50

3.4.1 Residual Glass Morphology and Composition. 51

3.4.2. Oxyapatite Morphology and Composition. 54

3.4.3 Oxyapatite Crystallization Kinetics. 59

3.4.4. Mo-rich Phase Morphology and Composition. 63

3.5. TIME-TEMPERATURE-TRANSFORMATION DIAGRAM 70

3.6. GLASS-CERAMIC FORMATION PATHWAYS 74

4. CONCLUSIONS 80

ACKNOWLEDGEMENTS 83

REFERENCES 84

II. THE EFFECTS OF MICROSTRUCTURE ON THE DISSOLUTION BEHAVIOR OF A COMPLEX GLASS-CERAMIC WASTE FORM 87

ABSTRACT.. 87

1. INTRODUCTION 88

2. EXPERIMENTAL METHODS 93

2.1. GLASS-CERAMIC COMPOSITION 93

2.2. THERMAL TREATMENTS 93

2.3. PRODUCT CONSISTENCY TEST 95

2.4. DIFFERENTIAL DISSOLUTION TEST 95

2.5. MICROSTRUCTURAL CHARACTERIZATION 97

3. RESULTS 97

3.1. EFFECTS OF THERMAL HISTORY ON MICROSTRUCTURE 97

3.2. ION RELEASE VALUES FROM PCT 98

3.3. RECESSION RATE VALUES FROM THE DIFFERENTIAL DISSOLUTION TESTS 99

4. DISCUSSION 105

5. CONCLUSION 113

ACKNOWLEDGEMENTS 114
REFERENCES 115

SECTION

3. CONCLUSION 117
  3.1. OVERALL SUMMARY 117
  3.2. FUTURE WORK 119

APPENDICES

A. SUPPLEMENTAL DATA FOR PAPER I 122
B. SUPPLEMENTAL DATA FOR PAPER II 143
BIBLIOGRAPHY 148
VITA………… 152

LIST OF ILLUSTRATIONS

SECTION Page

Figure 1.1. Atomic structure representations of (left) crystal and (right) glass 7

Figure 1.2. Crystal growth rate and nucleation rate as a function of temperature 11

Figure 1.3. TTT diagram for the C2-510 glass studied by Billings and Edwards 12

Figure 1.4. The double logarithmic plots obtained from DSC from Malek 16

Figure 1.5. Normalized z(a_n) function for crystallization of bulk $(GeS_2)_{0.3}(Sb_2S_3)_{0.7}$ from Malek 16

Figure 1.6. Long term dissolution processes of glass as a function of time 18

Figure 1.7. Proposed phase development 21

PAPER I

Figure 1. Schematic representations of isothermal experiments. 30

Figure 2. Optical image of the as-received glass. 31

Figure 3. Roller quenching system. 33

Figure 4. Schematic diagrams of assembled water-cooled copper wedge mold (left and center) and a photograph of the steel wedge mold (right). 34

Figure 5. Furnace cool experiment with embedded thermocouple. 34

Figure 6. a) Photograph and b) schematic illustration of the set-up for the small volume isothermal tin bath.. 38

Figure 7. Optical images of as-received glass melted in a stainless-steel tube at 1300°C for 90 seconds and then left) quenched into an isothermal tin bath at 800°C and held for 0.5 minutes before quenching in water; center) quenched into an isothermal tin bath at 800°C and held for 4 minutes before quenching in water; and right) quenched into an isothermal tin bath at 800°C and held for 60 minutes before quenching in water. 41

Figure 8. Cooling rate profiles for a thermocouple in a packed stainless-steel sample tube quenched in water bath (dotted line) and a thermocouple in a packed stainless-steel sample tube quenched in a tin bath set at 600°C, then quenched in water bath (solid line). 43

Figure 9. SEM micrographs of a) roller quench, b) 4.1°C/s, c) 3.4°C/s, and d) 0.1°C/s. 44

Figure 10. Scanning electron image (left) and Ru EDS map (right) of precious metal crystallites found in the roller quenched glass. 45

Figure 11. XRD patterns from the as-received glass cooled at various rates with the peaks assigned to the identified phases. 46

Figure 12. An SEM image and Nd, Ca, Mo, Ba, and Na X-ray maps collected from oxyapatite and powellite particles formed in a sample quenched at 3.4°C/s. . 47

Figure 13. Electron image and Mo, Ba, and Ca X-ray maps collected of a molybdate particle formed in a sample quenched at 3.4°C/s. 49

Figure 14. TEM electron image and selected area diffraction (SAD) pattern of a Mo-rich particle in the 4.1°C/s sample showing diffracted spots indicitive of crystalline materials. 50

Figure 15. XRD patterns of as-received glass, baseline quenched sample (~300°C/s), samples heat-treated for various temperatures at 900°C, and heat treated at 1100°C for 60 min. 51

Figure 16. a) SEM electron image of the sample heat treated at 1100°C for 60 min of a Mo-rich phase also containing lanthanides, b) Mo EDS map, and c) Nd EDS map. 52

Figure 17. Electron micrographs of the PNNL glass after different continuous cooling experiments. 52

Figure 18. SEM micrographs of the a) 900°C isothermal sample after 0.5 min, b) 900°C isothermal sample after 2 min, c) 1000°C isothermal sample after 0.5 min, and d) 900°C isothermal sample after 0.5 min.. 55

Figure 19. Size of phase-separated droplets in the PNNL glass quenched at different rates. 57

Figure 20. SEM micrograph of oxyapatite in samples heat treated at a) 1100°C for 4 min, b) 1000°C for 2 min, c) 900°C for 2 min, d) 800°C for 4 min, e) 700°C for 60 min, f) 900°C for 60 min, g) 3.4°C/s, h) 0.1°C/s and i) 0.008°C/s. 58

Figure 21. TTT and CCT diagrams for oxyapatite formation. 60

Figure 22. SEM micrograph and EDS maps showing the outward growth of oxyapatite from a RuO_2 crystal cluster in the sample heat treated at 1100°C for 32 minutes. 61

Figure 23. Crystal fraction of oxyapatite vs time for samples from the isothermal experiments. 63

Figure 24. Avrami plot for oxyapatite isothermally held at various temperatures. 64

Figure 25. ln(k_n) vs 1000/T for oxyapatite growth from isothermal hold experiments between 700 and 1000°C. 66

Figure 26. SEM images of powellite in samples continuously cooled a) 3.4°C/s, b) 0.1°C/s, and c) 0.008°C/s. 67

Figure 27. Molybdenum droplet diameter vs quench rate for samples from the continuous cooling experiments. 67

Figure 28. SEM images of Mo-rich phases in samples heat treated isothermally a) 900°C for 2 min, b) 1100°C for 4 min, c) 1100°C for 16 min. 68

Figure 29. TTT (black symbols) and CCT (blue lines) for the formation of different Mo-rich crystals. 72

Figure 30. µ-Raman spectra of (dashed lines) a powellite sphere and cross in the sample heat treated at 1000°C for 4 min and (solid lines) spectra of a powellite needle, oxyapatite, and the residual glass in the 1100°C 60 min sample. 73

Figure 31. Micrographs showing locations of where the Raman spectra in Figure 30 was collected. 74

Figure 32. TTT diagram describing the fraction of crystallized material that forms in the PNNL borosilicate waste glass. 77

Figure 33. Schematic figure of the effects of time and temperature on the development of microstructural features in the borosilicate waste glass-ceramic. 78

Figure 34. Phase transformation pathways of isothermal and continuous cooling experiments. 81

PAPER II

Figure 1. Long-term dissolution behavior of a waste glass 89

Figure 2. Top) schematic diagram of a sample from a differential dissolution test, with the titanium reference layer and a crystal exposed after dissolving away the surrounding glass. Bottom) an optical image of the air-cooled sample coated with ~150 nm of titanium before a dissolution test. 96

Figure 3. Electron images from samples quenched at different rates; a) roller quench (TEM), b) 4.1°C/s, c) 3.4°C/s, d) 0.1°C/s, and e) 0.008°C/s. 100

Figure 4. Seven-day PCT method “A” results for the centroid composition as a function of cooling rate. 101

Figure 5. SEM micrograph and EDS maps from a sample cooled at 3.4°C/s, then reacted for how long in deionized water at 90°C. 102

Figure 6. AFM scan of an oxyapatite crystal in the sample cooled at 3.4°C/s after 12.5 days in deionized water at 90°C. 103

Figure 7. Left, example measurement of sample cooled at 3.4°C/s showing crystal to the glass measurements and, right, Ti coating to the glass measurements for the sample after 12.5 days in deionized water at 90°C. .. 104

Figure 8. Example profilometry line scans of the sample quenched at 3.4°C/s before (dashed) and after (solid) reacting in 90°C deionized water for eight days. 105

Figure 9. Profilometry (solid symbols) and AFM (open symbols) results in Δh as a function of time. 106

Figure 10. Mass loss from sample weight measurements in grams. 107

Figure 11. SEM images of a CCC sample after seven days in 90°C deionized water, showing left) a powellite and a oxyapatite crystal and right) a lower magnification image showing more representative sizes of the powellite and oxyapatite crystals. 108

Figure 12. Profilometry scan of the CCC sample after 7 days in 90°C DI water. 108

Figure 13. Expanded regions from Figure 12. 109

Figure 14. B ion release rate vs B_2O_3 concentration in the residual glass. 112

LIST OF TABLES

SECTION Page

Table 1.1. Radioactive waste types [8]. 2

Table 1.2. The ten waste groups [11]. 3

Table 1.3. Composition of Collins CLT waste [13]. 4

Table 1.4. Oxide additions to develop borosilicate waste glasses [7, 15]. 5

Table 1.5. Centroid glass-ceramic target composition [15]. 6

Table 1.6. Effects of intermediate and modifier oxide additions on glass structure [17]. .. 9

Table 1.7. Glass corrosion processes [34]. 18

Table 1.8. Compositional effects on elemental release rates [25]. 24

Table 1.9. Normalized release rates from PCT of the centroid glass composition cooled with CCC (g/m^2) [25]. 24

PAPER I

Table 1. Centroid glass-ceramic target composition [13]. 32

Table 2. Treatment schedule comparable to the CCC of a waste storage canister [8]. 35

Table 3. Quench rates for continuously cooled and some isothermal samples, calculated from the time between the maximum recorded temperature and when the sample reached 590°C. 42

Table 4. Compositions of the different phases in the phase-seperated residual glass of the 4.1°C/s sample, determined by TEM EDS with oxygen normalized to 0. 56

Table 5. Cation fractions in oxyapatite crystals in samples with different heat treatments with oxygen normalized to 0, compared with those reported by Crum et al. [13]. 62

Table 6. Cation fractions of Mo-rich crystals in samples with different heat treatments with oxygen normalized to 0, compared with those reported by Crum et al. [13]. 71

Table 7. Estimated composition of the residual glass at various cooling rates. 82

PAPER II

Table 1. Composition of Collins CLT waste [9]... 90

Table 2. Treatment schedule comparable to the CCC of a waste storage canister [9]. 91

Table 3. Compositional effects on elemental release rates [16]. 93

Table 4. Glass composition [16]. 94

Table 5. Quench rates and phases for each sample [17]. 94

Table 6. Compositions of the major phases in the glass. 99

Table 7. Estimated compositions of the residual glass phase in glass-ceramic samples created with different quenching rates and the estimated composition reported by Asmussen et al. [15].. 111

1. INTRODUCTION

1.1. BACKGROUND

With the notable discoveries of x-rays by Wilhelm Conrad Roentgen in 1895, radioactivity in 1896 by Henri Becquerel, radioactive materials by Pierre and Marie Curie in the early 1900's, and the nuclear reactor in 1942 by Enrico Fermi, artificial radioactive materials have been available for over a century [1-3]. Many industries have greatly benefited from the use of radioactive materials including, but not limited to, the power generation, agriculture, and medicine [4]. However, a major challenge in the nuclear field is determining what to do with the long-lived radioactive waste.

Radioactive waste is described by the U.S. Environmental Protection Agency as a hazardous waste under the criteria in Title 40 of the Code of Federal Regulation, part 261, and becomes exempt from this code if the waste is compliant with Title 40 of the Code of Federal Regulation part 266, Subpart N [5]. Under Title 10 of the Code of Federal Regulation Part 961, the United States Department of Energy, DOE, is contracted to manage the proper disposal of nuclear waste [6]. To determine whether radioactive waste forms are compliant and environmentally safe, the DOE developed the Waste Acceptance Product Specifications (WAPS) [7]. The WAPS considers the radionuclide inventory, chemical composition, product consistency, and phase stability of the waste form [7].

1.2. RADIOACTIVE WASTE

The International Atomic Energy Agency, IAEA, has classified radioactive waste into six distinct categories based on safety guidelines, summarized in Table 1.1 [8]. The main source of radioactive wastes comes from the Nuclear Fuel Cycle, NFC, used for power generation and military purposes, which produces low level waste (LLW), intermediate level waste (ILW), and high-level waste (HLW) [4]. Reprocessing techniques recycle the radioactive waste, greatly reducing the amount of waste, and combine them into single HLW compositions for disposal.

Table 1.1. Radioactive waste types [8].

Waste Name	**Characteristics**	**Disposal**
Exempt Waste (EW)	Small concentrations of waste ≤10μSv/year	No disposal required
Very Short-Lived Waste (VSLW)	Waste with short half-life's ≤ 100 days.	Stored until acceptable
Very Low-Level Waste (VLLW)	Materials used in operating nuclear facilities that are slightly above EW waste concentrations	Landfill type storage
Low Level Waste (LLW)	Restricted waste with harmful levels	Near Surface Disposal
Intermediate Level Waste (ILW)	Higher concentrations than LLW that need more containment from the atmosphere.	Geological Disposal
High Level Waste (HLW)	Waste that generally produces 10^4 TBq/m^3 and generate significant quantities of heat.	Engineered Geological Disposal and Containment Canister

In the United States, programs such as the Fuel Cycle Research and Development, FCRD, program of the Office of Nuclear Energy in the DOE are tasked with developing spent nuclear fuel reprocessing technologies in efforts to greatly reduce the volume of radioactive waste. The fuel reprocessing technologies are intended to combine waste streams into groups based on composition to minimize volume [9]. To develop a single global waste form, long-lived, heat-generating, and volatile radioactive components would need to be further combined with lanthanides, minor actinides, and any remaining undissolved solids [9]. Existing HLWs, at sites like those in Hanford, WA, are generally from open nuclear cycles, unprocessed waste streams, which contain many different components. Future nuclear fuel cycles are intended to be close-ended systems in which the waste is to be reprocessed many times and separated into groups with similar components allowing waste forms with higher waste loadings and more desirable properties to be developed [9].

The DOE developed the Used Fuel Disposition Campaign (UFDC) to characterize all the Spent Nuclear Fuel (SNF) and HLW, both defense and commercial, in the United States and this is compiled into an on-line waste library (OWL) database [10, 11]. In the US, as of 2012, the UFDC listed 69,500 metric tons of heavy metal (MTHM) commercial SNF, totaling ~23 billion curies of long-lived radioactivity, stored at 75 sites in 33 states [11]. In 2048 there is projected to be 142,000 MTHM of SNF. The study determined that there are 43 different waste types, and 50 waste forms that can be combined into 10 different waste groups, based on disposal needs, to be stored in a geological disposal, summarized in Table 1.2 [11].

Table 1.2. The ten waste groups [11].

Waste Group and Description
1- SNF packaged in purpose-built disposal containers
2- SNF packaged in dual-purpose canisters of existing design
3- Vitrified HLW - all types of canistered HLW glass, existing and projected
4- Other engineered HLW waste forms
5- Metallic and non-oxide spent fuels
6- Sodium-bonded fuels
7- DOE oxide fuels
8- Salt, granular solids, and powders
9- Coated-particle spent fuel
10- Spent Naval fuel

Many HLWs from open or “once through” fuel cycles in the United States have already been studied [11]. In some cases, like the West Valley Demonstration Project (WVDP) in New York, the waste has been reprocessed into a borosilicate glass [11]. Due to advancements in the fuel cycle process, “once through” HLW waste can be recycled through the fuel cycle again to further produce energy and greatly reduce the amount of waste [12]. Once the products become nonfissionable, they are removed from the process stream using aqueous reprocessing techniques such as TRUEX$^+$ or UREX$^+$ and stored as secondary HLW. Nonfissionable waste streams from the reprocessing of a baseline “once through” HLW contain alkalis, alkaline earths, lanthanides, and transition metals. An approximation for a final secondary HLW composition containing large amounts of Mo, and Cs is shown in Table 1.3, and is denoted as Collins CLT [13]. The waste composition was determined from light-water reactor (LWR) fuel after a 40 GWd burn-up and a 10-year decay storage.

Table 1.3. Composition of Collins CLT waste [13].

Oxide	**Content [mol%]**	**Oxide**	**Content [mol%]**
MoO_3	19.719	CdO	0.621
ZrO_2	17.590	SeO_2	0.534
Nd_2O_3	11.279	Eu_2O_3	0.354
BaO	10.443	Ag_2O	0.353
Cs_2O	7.416	SnO_2	0.339
SrO	6.887	Gd_2O_3	0.322
Ce_2O_3	6.859	Rh_2O_3	0.226
La_2O_3	3.527	Br	0.205
Pr_2O_3	3.187	PdO	0.100
TeO_2	2.985	Pm_2O_3	0.036
Sm_2O_3	2.240	Sb_2O_3	0.028
Y_2O_3	2.019	In_2O_3	0.007
Rb_2O	1.641	Tb_2O_3	0.006
RuO_2	1.076	**Total**	**100.000**

1.3. BOROSILICATE GLASS-CERAMICS FOR WASTE VITRIFICATION

HLW produced by reprocessing SNF is intended to be stored as acceptable waste forms. The WAPS was designed by the DOE to ensure that the waste is acceptable and compliant with US Code of Federal Regulations [7]. The standard waste form defined by the WAPS is vitrified waste in a borosilicate glass. In the United States, the only waste form currently used for HLW immobilization is borosilicate glass. The West Valley Demonstration Project and Savannah River site have both successfully developed borosilicate glass compositions for vitrifying HLW that is compliant with the WAPS [11].

Borosilicate glasses have desirable properties for the immobilization of nuclear waste, including excellent chemical durability, thermal and radiation stability, and mechanical integrity [4]. Also, many waste elements are soluble in borosilicate glasses allowing high levels of waste loadings. However, some elements such as molybdenum, are insoluble at levels >3 mol% [13, 14]. Typical borosilicate glass compositions according to the WAPS, are listed in the Table 1.4 [7, 15], and compared to the PNNL glass used in this study (Table 1.5).

Table 1.4. Oxide additions to develop borosilicate waste glasses [7, 15].

Oxide Additions		**WAPS [wt.%]**	**PNNL [wt.%]**
Formers	SiO_2	33-65	30.99
	B_2O_3	3-20	8.53
Intermediates	Al_2O_3	3-20	4.80
Modifiers	Na_2O	4-22	2.73
	Metal Oxides	0-50, ~24	-
	Li_2O	-	1.05
	CaO	-	5.12

PNNL developed an alternative strategy to the use of homogeneous waste glass, and that was to use glass-ceramic materials with greater levels of CLT-loadings [15]. An example of one borosilicate glass-ceramic with 47.394 wt.%, Collins CLT is listed in Table 1.5 and this composition was used in this study [15]. Increasing the waste loading by allowing crystalline phases to form adds microstructural complexity which requires an understanding of phase separation and subsequent nucleation and growth of the crystals. Furthermore, the chemical durability of the individual phases in these new materials must be understood to ensure that the waste form meets corrosion requirements. The following sections outline relevant theories and studies from the literature related to this study on microstructural development and its effect on aqueous corrosion of a borosilicate glass-ceramic for waste vitrification.

Table 1.5. Centroid glass-ceramic target composition [15].

Oxide	**Content [mol%]**	**Oxide**	**Content [mol%]**
SiO_2	47.674	TeO_2	0.641
B_2O_3	11.329	Sm_2O_3	0.481
CaO	8.445	Y_2O_3	0.433
MoO_3	4.229	Rb_2O	0.353
Al_2O_3	3.789	RuO_2	0.232
Na_2O	4.069	CdO	0.135
ZrO_2	3.774	SeO_2	0.116
Li_2O	3.247	RhO_2	0.089
Nd_2O_3	2.427	Eu_2O_3	0.076
BaO	2.241	Ag_2O	0.075
Cs_2O	1.591	SnO_2	0.072
SrO	1.476	Gd_2O_3	0.070
Ce_2O_3	1.472	PdO	0.023
La_2O_3	0.757	**Total**	**100.000**
Pr_2O_3	0.684	**Waste Loading**	**21.447**

1.3.1. Glass Structure. Atomic arrangements affect the properties of a material, so it is important to understand the relationships between composition and structure. The materials under study here are glass-ceramics which possess both crystalline and amorphous phases [17]. Zachariasen described the structure of glass and related crystalline materials [18]. Crystalline materials possess periodic arrangements of unit cells with fixed atomic dimensions whereas glasses have an indefinitely large unit cell and lack atomic periodicity. These different arrangements are schematically shown in Figure 1.1. Zachariasen predicted that the local (polyhedral) arrangements of the atoms in a glass were similar to those of atoms in a crystal, and that the differences between the structure and morphologies of a glass and crystal result from how those polyhedra are arranged on large scales. He recognized that certain crystal structures were associated with ready glass formation when melts were quenched, and that these structures are relatively open [18]:

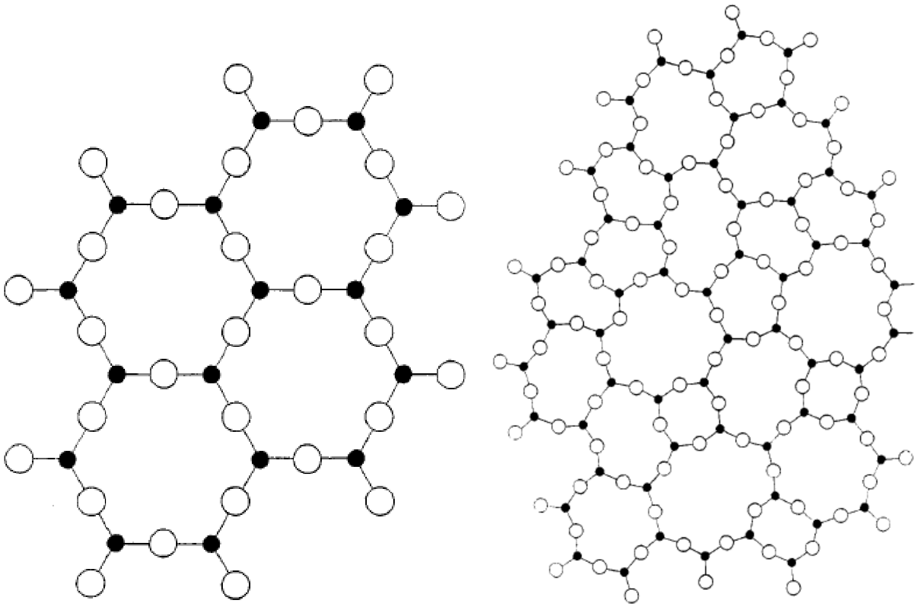

Figure 1.1. Atomic structure representations of (left) crystal and (right) glass [17].

Oxides with these open structures are classified as glass formers. In borosilicate glasses, silica and boron oxide are the glass formers. In silica glass, silicon is coordinated by four oxygen ions which then link to neighboring silica tetrahedra [17]. In vitreous B_2O_3, boron has a coordination number of 3, forming BO_3 triangular structural units.

Not all oxides are glass formers, and Sun associated the cation-oxygen bond strength with glass forming tendency [19]. Glass forming oxides have the highest cation-oxygen bond strength and are the backbone of the glass structure. Glass modifying oxides have the lowest bond strengths and do not form glasses when quenched from a melt. Instead, these oxides are incorporated into the glass network, modifying the glass properties. Intermediate oxides also do not form a glass structure by themselves, but when combined with other formers and modifiers, they tend to develop strong bonds similar to the glass formers.

Additions of modifier and intermediate oxides to a glass affect properties, generally by increasing or decreasing connectivity between network forming polyhedra. Connectivity relates to properties associated with mass-transport such as viscosity, diffusion, electrical conductivity, and corrosion [17]. The connectivity is increased when greater fractions of glass formers and intermediates are added to a composition and the connectivity in silicate glasses is decreased when modifying oxides are added. Modifying cations are linked to glass network through weak bonds with non-bridging oxygen (NBO), replacing strong bridging oxygens that link network forming polyhedra. In borate glasses, modifying oxides can be incorporated into the glass structure by transforming borate triangles into borate tetrahedra, increasing the fraction of bridging oxygens, with concomitant changes in glass properties. Table 1.6 summarizes the effects of the additions of intermediates and modifiers on the structures of simple glass systems [17]. It should be noted that the specific effects depend on particular composition ranges.

Table 1.6. Effects of intermediate and modifier oxide additions on glass structure [17].

Glass	**Effect**
Modifier Additions	
Alkali-Silicate	Creation of 1 NBO per alkali ion reducing connectivity.
Alkali-Alkaline Earth - Silicate	Creation of 2 NBO's per alkaline earth ion, which stabilizes alkaline-silicate glasses maintaining connectivity.
Alkali-Borate	Creation of NBOs, reducing connectivity, or the conversion of Boron from 3 to 4 coordination, increasing connectivity.
Alkali-Borosilicate	Creation of NBO's if the alkali associates with Si. Conversion of Boron coordination from 3 to 4 if alkali associates with B.
Intermediate Additions	
Alkali-Aluminosilicate	Al_2O_3/Alkali < 1 removes NBO/Al -ion Al_2O_3/Alkali = 1 no NBO's Al_2O_3/Alkali > 1 addition of 1, 2, or 3 NBO's

The borosilicate centroid composition shown in, Table 1.5, has intermediate (Al_2O_3) and glass network modifier oxides (Na_2O, CaO, and Li_2O) that are added to control the properties of the glass. Some high-level wastes will already contain significant amounts of aluminum and sodium [20, 21]. Aluminum increases the viscosity at high temperatures, increasing homogenization time but reducing volatilization [20, 22]. Aluminum also significantly increases the chemical durability of the glass [22]. Additions of sodium and lithium reduce melting temperatures to enable glass production [20]. Calcium is added to the glass to increase the chemical durability [20].

1.3.2. Glass-Crystal Transformations. A characteristic of a glass forming melt is its resistance to crystallization upon cooling. In fact, all liquids can be vitrified into a glass if the cooling rate of the melt is fast enough [17]. For macroscopic crystallization to occur, crystal nuclei must first form and then, crystals must grow from the nuclei [23]. It is important to understand the nucleation and crystallization pathways to develop glass-ceramics with controlled properties.

Nucleation and crystallization occurs when melts are undercooled below the equilibrium melting temperature, shown in Figure 1.2 from Varshneya [17]. The relative area overlapping the nucleation and crystallization rate curves relates to the ability of an undercooled melt to be quenched without crystallization and so to form a glass. If there is little or no overlap between the nucleation and crystallization rate curves, then the material will easily form a glass. A large overlap, however, means fast crystallization of the nuclei that form, increasing the difficulty of forming a homogeneous glass upon melt quenching.

For glass-ceramics, crystal growth and the onset of crystallization are widely described using time-temperature transformation and constant-cooling transformation diagrams. A time-temperature-transformation (TTT) diagram maps out the temperatures and times where crystals form. Similarly, constant-cooling-transformation (CCT) diagrams also map out crystallization conditions. The difference between the two is that TTT diagrams describe isothermal heat treatments, and CCT diagrams describe constant cooling heat treatments. Crystallization conditions depicted in CCT diagrams are shifted to slower times compared to TTT diagrams and only reproduce the top half of the crystallization curve. Billings and Edwards performed an extensive study developing TTT diagrams for glasses containing projected HLW at the Savannah River site [24]. Figure 1.3 is a TTT diagram for one of the borosilicate glasses they studied showing the times and temperatures when certain crystals have formed.

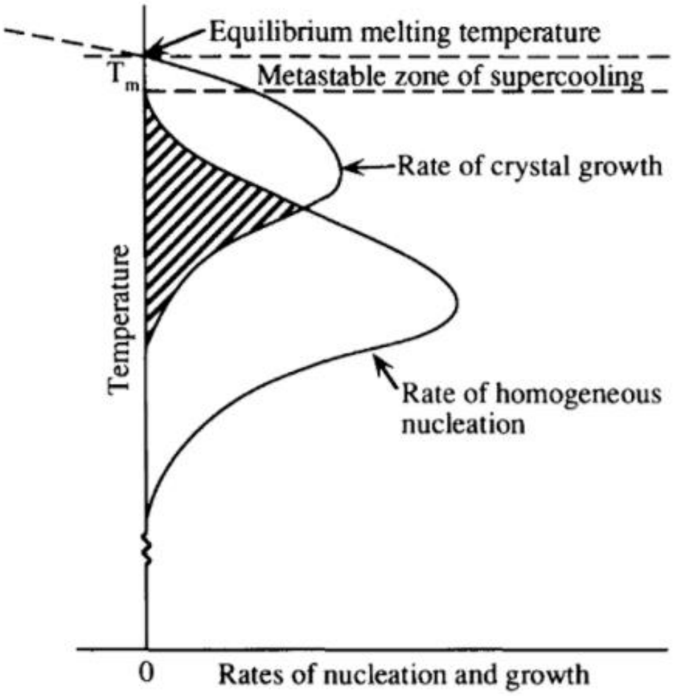

Figure 1.2. Crystal growth rate and nucleation rate as a function of temperature [17].

As stated by the Waste Acceptance Product Specifications (WAPS), TTT diagrams must be produced for waste forms [7]. The TTT diagram is needed to identify the times and temperatures where significant phase changes can occur. Along with the TTT diagram, the glass transition temperature for the waste glass must be known as well. Above the glass transition temperature, there is an increased likelihood for crystallization to occur, altering the properties of the waste form. A goal of the present study is to develop a TTT diagram, similar to the diagrams produced by Billings and Edwards, for the centroid composition shown in Table 1.5 [25].

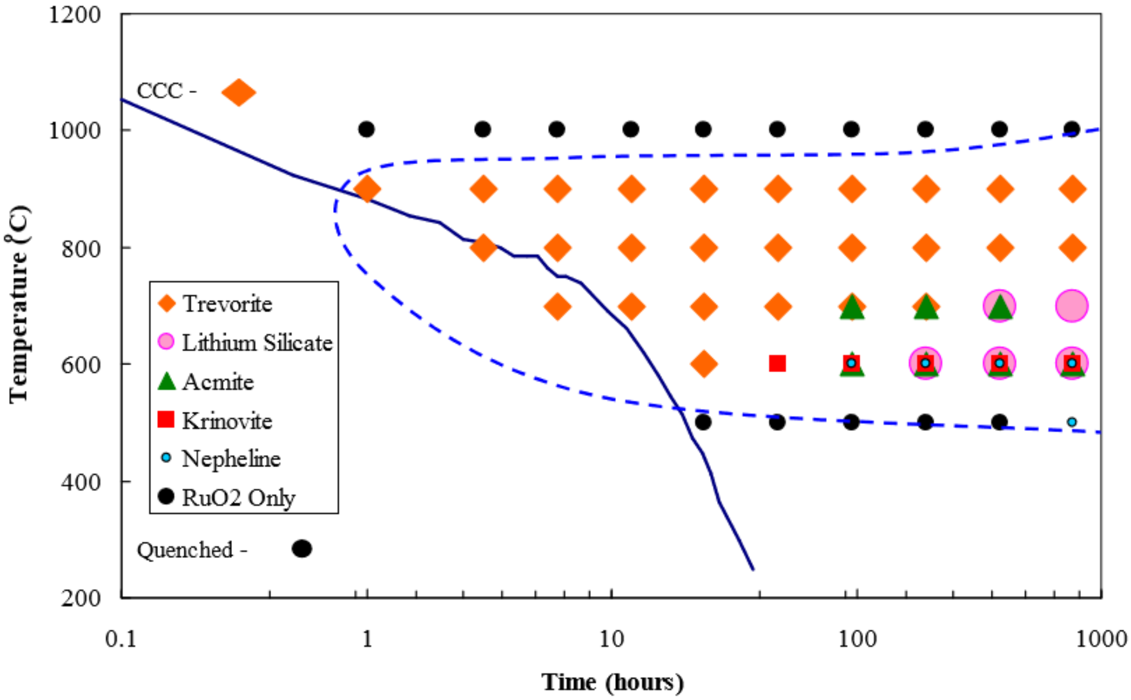

Figure 1.3. TTT diagram for the C2-510 glass studied by Billings and Edwards [24].

1.3.3. Glass-Crystal Transformations Experimental Methods. The temperature dependence of the phase stability of the waste form is important considering the amount of heat released from the radioactive components. The minimum limit for the glass transition temperature according to the WAPS is 400°C [7]. At the glass transition temperature, the structure relaxes, and heat is absorbed i.e., the glass transition is an endothermic process. Commonly used techniques for determining the glass transition temperature are differential scanning calorimetry (DSC) and differential thermal analysis (DTA) [17]. In both tests, the samples are heated or cooled through the transformation zones at fixed rates and compared to standards with known transitions. In DSC, the power supplied to the sample is varied to keep the sample at the same temperature as the reference. For DSC, the reference is usually just an empty pan. In DTA, the difference in temperature between the reference and the sample is measured. The reference material used is usually a material with no transitions in the desired temperature range, like α-alumina. Along with the glass transition temperature, DTA and DSC can determine the onset of crystallization and the maximum crystallization rate temperatures due to the processes being exothermic.

For the development of CCT curves, samples are commonly heated or cooled at designated rates and later analyzed using microscopy and x-ray diffraction. For TTT diagrams, samples are melted then quenched to a pre-determined temperature and held for various times before being quenched to room temperature to be analyzed. This latter technique is common to describe the crystallization of systems where the onset time of crystallization is much greater than the cooling time transferring from the melt to the isothermal temperature. As the sample is cooled from the melt to the isothermal holding temperature and later to room temperature, the sample is still nucleating and crystallizing so maximizing these cooling rates is important. In the Billings and Edwards experiments, 30 grams of glass was placed in a crucible that was melted and simply transferred to another furnace at the desired heat-treatment temperature [24]. For their glass-ceramics, crystals took hours to form so the cooling rate from the melt furnace would have a minimal effect on the results, with temperatures equilibrating within minutes. For melts that quickly crystallize, techniques that quickly quench the melt to the isothermal holding temperature are necessary. Peterson developed TTT diagrams for mold fluxes by quenching samples from a melt into a molten tin bath held at the desired heat-treating temperature [26]. The quenching step was necessary since some crystals formed within minutes. Peterson measured quench rates from the melt to the molten tin to be ~65°C/s and from the molten tin to the water bath at room temperature to be ~30°C/s.

1.3.4. JMAK Crystallization Model [23, 27-32]. The Johnson-Mehl-Avrami-Kolmogorov (JMAK) model can be used to characterize the time and temperature dependence of transformation processes, commonly but not limited to characterizing the time and temperature dependence on crystallization. The overall transformation process (e.g. crystallization) at a specific time ($\alpha_n(t)$) can be simply defined as

$$\alpha_n(t) = \frac{V_n(t)}{V_o} \qquad (1)$$

where $V_n(t)$ is the volume of crystals at time (t) and V_0 is the total volume. In the JMAK model, $\alpha_n(t)$ can be predicted knowing the nucleation rate (J), linear growth velocity (ν), and the geometric shape factor (ω_n) in which J, v, and ω_n are constants independent of time. Accounting for the decrease in available volume for potential crystallization with increasing crystallization, the classic JMAK equation is described as

$$\alpha_n(t) = 1 - e^{\left(-\frac{\omega_n}{n+1} J\, v^n\, t^{n+1}\right)} \qquad (2)$$

where n, the Avrami exponent of the transformation, relates to the different growth and nucleation mechanisms. Needle-like features grow when n=1, disc or plate like features form when n=2, and spherical features form when n=3. If

$$k_n = \frac{\omega_n}{n+1} J\, v^n \qquad (3)$$

then Equation (6) can be rewritten as

$$\ln[-\ln(\alpha_n(t))] = \ln(k_n) + (n+1)\ln(t) \qquad (4)$$

where in ln(k_n) is the intercept and n is the slope of a double logarithmic -ln(1- α_n(t)) versus t plot which can be extracted from the TTT diagrams. The Avrami kinetic coefficient (k_n) relates to the activation energy (E) using the Arrhenius equation,

$$k_n = k_o e^{\frac{-E}{RT}} \tag{5}$$

where k_o is a frequency factor and R is the gas constant. Equation 9 can be re-written as

$$\ln(k_n) = \ln(k_o) - \frac{E}{RT} \tag{6}$$

where the activation energy is obtained from the slope of the plot of ln(k_n) vs 1/T.

The applicability of the JMAK model to describe crystallization kinetics for glasses was investigated by Malek for both non-isothermal and isothermal conditions [32]. To understand the validity of the JMAK model it is important to understand the assumptions about the model. There are four main assumptions for the JMAK model:

1.) Isothermal crystallization
2.) Homogeneous nucleation (heterogeneous nucleation if the foreign sites are randomly and uniformly dispersed)
3.) Growth rate of the new phase is independent of time
4.) Spherical or low anisotropic growth of the new crystalline phase

When applying the JMAK model, it is important to verify that these conditions are met, as outlined by Malek [32]. A simple way to confirm the applicability of the JMAK model is to verify that the double log of crystallization ($\ln[-\ln(\alpha_n(t))]$) vs the ln(t) is linear, and that the Avrami kinetic coefficient (k_n) exhibits Arrhenius temperature dependence. Malek found linear dependencies for the crystallization of chalcogenide glass, $(GeS_2)_{0.3}(Sb_2S_3)_{0.7}$, shown in Figure 1.4.

Furthermore, the maximum of the z(α_n) vs α_n plot should occur when $\alpha_n \approx 0.632$, where

$$z(\alpha_n) = \phi t \text{ (isothermal test methods)} \qquad (7)$$

$$z(\alpha_n) = \phi T^2 \text{ (non-isothermal test methods)} \qquad (8)$$

and ϕ is the normalized specific heat flow per sample mass [32]. The maxima of the $z(a_n)$ function vs (a_n) was found to be within the range predicted using the JMA model, shown in Figure 1.5 from Malek.

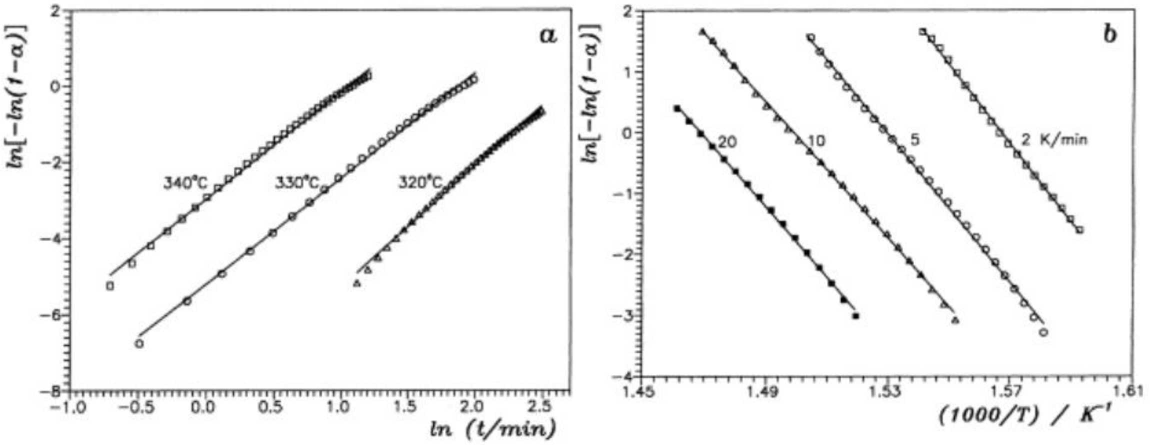

Figure 1.4. The double logarithmic plots obtained from DSC from Malek [32].

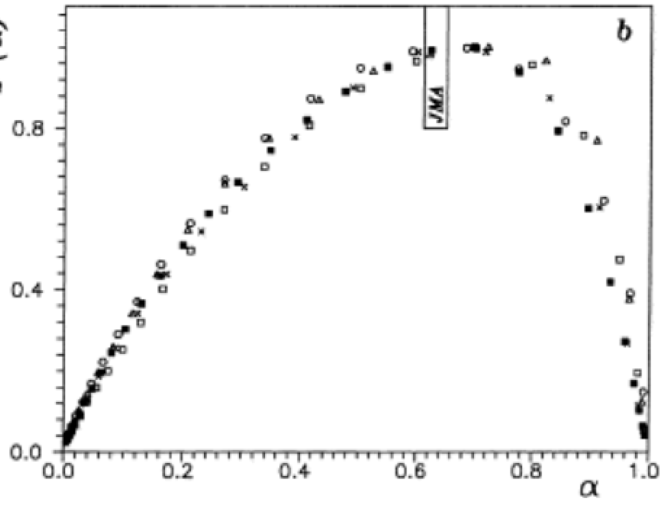

Figure 1.5. Normalized $z(a_n)$ function for crystallization of bulk $(GeS_2)_{0.3}(Sb_2S_3)_{0.7}$ from Malek [32].

1.3.5. Chemical Durability of Borosilicate Glasses. The chemical durability of waste glasses must be understood to ensure the hazardous ions are not released into the biosphere. Chemical durability of glasses refers to the resistance of the glass to dissolution in aqueous solutions [33]. The rate of the aqueous dissolution of glass can be expressed as a function of thermodynamic and kinetic stability. Thermodynamics suggests that the reaction will continue until equilibrium is reduced. Kinetically, the reaction will occur if the system has enough energy to overcome the activation barrier.

Gin et al. outlined state-of-the-art dissolution (corrosion) processes for glasses [34]. There are many intertwined corrosion processes when glass surfaces come in contact with aqueous solutions; some of these are listed in Table 1.7.

For the reaction of waste glasses with groundwater, certain processes dominate at certain reaction times as shown in Figure 1.6 [34]. Stage I, the initial rate, is dominated by interdiffusion and hydrolysis reactions. Over time a gel layer may form, reducing the interdiffusion rate since the ions now have to diffuse through this gel layer before exchanging into solution. The dissolution rate is also known to drop to the “residual rate” or Stage II due to saturation of silica in the surrounding aqueous environment. Stage II of the corrosion of glass is controlled by many competing processes. Over long times, a resumption of dissolution (Stage III) can occur when the precipitation of mineral phases on the glass surface reduces the activity of soluble silicates in solution.

1.3.6. Chemical Durability Experimental Methods. Understanding the chemical durability is important for optimizing waste form compositions. Simple pH and weight loss tests are commonly used to understand the dissolution of glasses and these are often combined with more advanced tests such as the analysis of reacted ions in leached solutions [33].

Table 1.7. Glass corrosion processes [34].

process	**description**
diffusion	diffusion of water into glass
interdiffusion	ion-exchange between ions in solution and weakly bound cations, usually alkali, in glass structure
hydrolysis	chemical breakdown of Si–O–M bonds (M = Si, Al, Zr, Fe, Zn, etc.)
condensation	condensation of the detached species
precipitation	crystallization of amorphous and soluble species

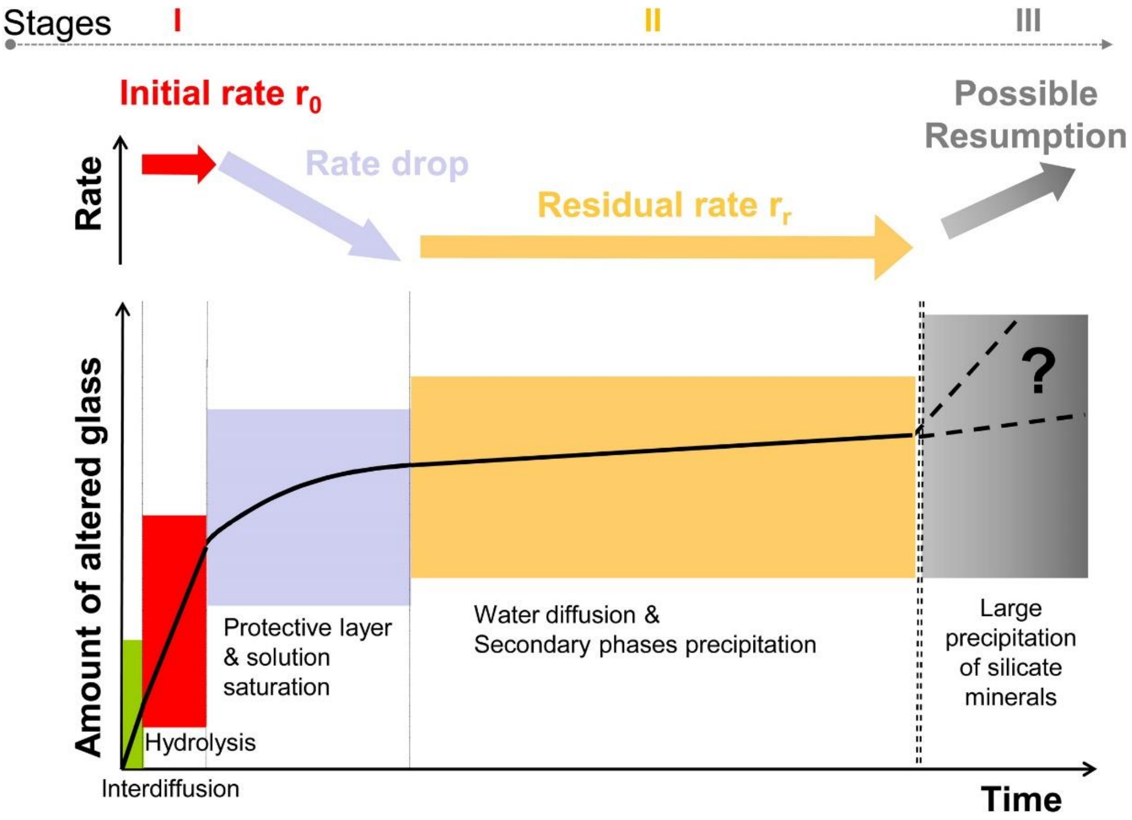

Figure 1.6. Long term dissolution processes of glass as a function of time [34].

The standard procedure for determining the chemical durability of waste glasses described by the waste acceptance product specifications, WAPS, is the Product Consistency Test, PCT [7, 35]. The PCT has rigorous test methods for determining the dissolution information in carefully controlled conditions. There are two versions of the PCT. Test method “A” is a specific seven-day test with no variability in experimental methods, allowing for cross-lab comparisons to be made. PCT test method “B” allows variability in test design to cater to the objectives of a study: for example, evaluating Stage I, II or III, dissolution behavior. As stated in the WAPS, the results of these tests are to be compared to the performance of the environmental assessment (EA) glass, the benchmark standard for acceptable waste glasses [36, 37].

1.4. BOROSILICATE GLASS-CERAMICS FOR IMMOBILIZING US COMMERCIAL REPROCESSED SNF

The current study is part of a much larger project that has been ongoing for over a decade involving many research groups to develop a borosilicate glass-ceramic for immobilizing the HLW stream generated from aqueous reprocessing of commercial SNF in the United States [25]. This section will review the previous work linked with this study, as well as other relevant literature.

The materials characterized in the present study and associated projects are intended to immobilize the Collins CLT waste stream from commercial reactors, Table 1.3. These studies have focused on immobilizing the waste using borosilicate glasses and glass-ceramics, although some other work has been done to evaluate other waste forms, such as iron-phosphate glasses [38].

PNNL has played a major role in the research on glass-ceramic development for immobilizing the Collins CLT waste [13, 15, 16, 25, 40-42]. Borosilicate glass-ceramics are of interest because they would allow greater loadings of insoluble components than would be possible for homogeneous glasses [39]. Compositions with up to 50 wt.% waste have been developed [16, 40]. These compositions have been melted using cold crucible induction melter technologies, demonstrating the possibility for full-scale processing of these glass-ceramics [41]. The initial experiments [13, 16, 40, 41] produced a compositional matrix for optimizing the glass-ceramics, considering both variations in the types and concentrations of glass components (Al_2O_3, B_2O_3, CaO, Li_2O, Na_2O, and SiO_2) and insoluble waste components, including lanthanide oxides (Ln_2O_3), ZrO_2, and MoO_3 [25].

1.4.1. Phase Development. The crystalline phases that form in the glass-ceramics developed at PNNL for vitrifying the Collins CLT waste, include oxyapatite ($Ca_2Nd_8Si_6O_{26}$), Ln-borosilicate ($Gd_3BSi_2O_{10}$), powellite ($(Ca,Sr)MoO_4$) or $(Ca,Ba)MoO_4$), $CsLiMoO_4$, $La_2Mo_3O_{12}$, pollucite ($CsAlSiO_4$), $Zr_{0.9}Ce_{0.1}O_2$, Y_2O_3, and RuO_2 [25]. The centroid composition in the matrix, the composition used in the present study and given in Table 1.5, produced oxyapatite and powellite as the major phases.

The development of phases from the borosilicate melts is summarized in Figure 1.7 from Crum et al. [41]. Upon cooling, molybdenum-rich droplets separate from the surrounding glass, and that glass itself separated into and aluminum-silicon–cesium-rich droplets and a borosilicate matrix. When cooled slowly, the molybdenum-rich droplets crystalize into $BaMoO_4$ and $CaMoO_4$, and oxyapatite crystallizes from the residual glass matrix. Quantitative x-ray diffraction determined that a sample with the centroid composition cooled along the centerline cooling temperature profile of a waste canister (~0.005°C/s) included 18.6 wt.% oxyapatite ($Ca_2Ln_8SiO_2$), 9.1 wt.% $Ca_xSr_{1-x}MoO_4$, and 0.4 wt.% $Ca_xBa_{1-x}MoO_4$ [15]. A goal of this study is to determine at which temperature the phases in Figure 1.7 are forming to develop an updated phase transformation diagram as a function of time and temperature.

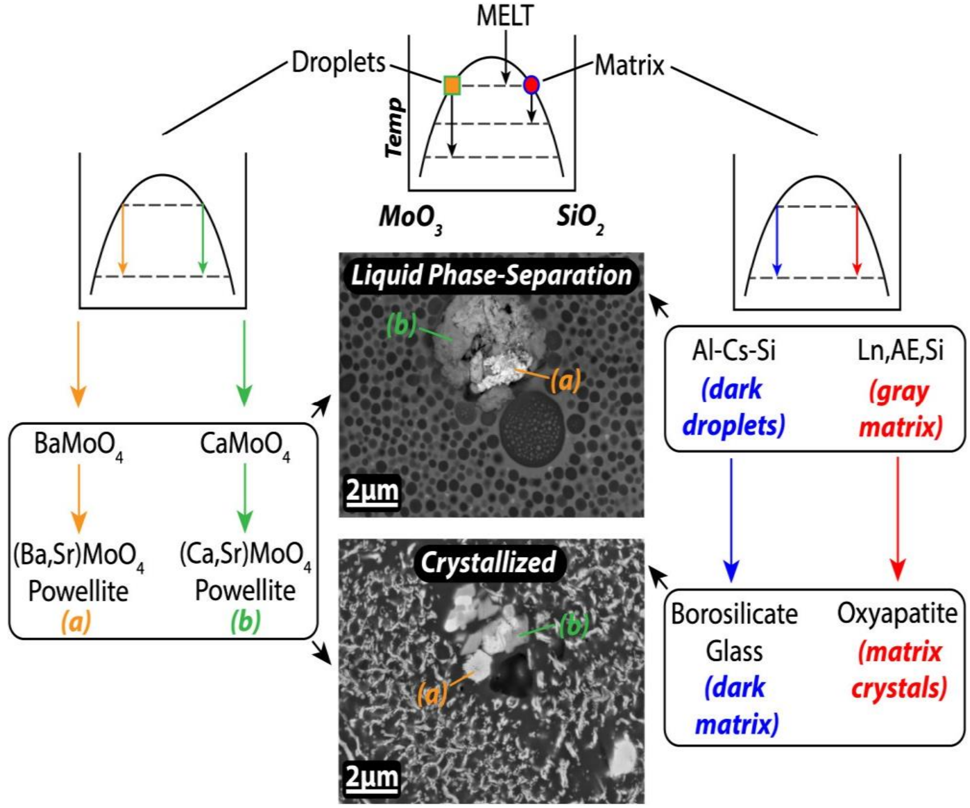

Figure 1.7. Proposed phase development [41].

Molybdates and oxyapatite crystals precipitate from the borosilicate waste glass due to the low solubilities of Mo and lanthanide oxides [13, 14, 43, 44]. Molybdate species like $[MoO_4]^{2-}$ are not strongly bonded to the silicate and borate network formers [14, 44].

Lanthanide ions are believed to be associated with the $[MoO_4]^{2-}$ units in the melts which are also found to slightly inhibit the crystallization of powellite [44, 45].

Depending on the glass composition, other molybdate phases can form, including Na_2MoO_4 [43]. Na_2MoO_4 has a lower chemical durability than $CaMoO_4$ and $BaMoO_4$, so avoiding Na_2MoO_4 in the waste forms is desired [46]. It was found that increasing the $[Ca^{2+}]/[Na^+]$ ratio in the glass favored the formation of $CaMoO_4$ over Na_2MoO_4 [45, 46]. In addition, increasing the B_2O_3 content reduced the formation of Na_2MoO_4 by sequestering the Na^+ ions to charge balance the $[BO_4]^-$ units [46].

1.4.2. Chemical Durability. PCT studies at PNNL of glass-ceramics with low waste loadings (< 25 mass%) Si, B, Na, and Li release rates that were all an order of magnitude below those from the EA reference glass [13]. The release rate of Mo from a glass with 3.5 mass% Mo was much greater (1.06 g/L) when the melt was cooled slowly, following the canister center-line cooling (CCC) protocol than when the glass was quenched on a steel plate (0.3 g/L) [13]. No crystalline phases were present in the plate quenched sample and crystalline oxyapatite ($Ca_2LN_8Si_6O_{26}$) and a molybdate phases were found in the slow cooled sample. It was believed that the increase in the Mo release rate from the slow cooled sample was due to the preferential dissolution of the Mo-rich crystalline phase.

Glasses with high waste loadings, up to 50 wt.%, were cooled using the CCC profile and were reacted in static dissolution conditions for various times [40]. Mo release rates significantly increased (0.05 to 0.4 g/L) when the MoO_3 composition increased from 6.25 wt.% to 6.95 wt.%. It was believed that Mo was mostly contained in the crystalline phase ($CaMoO_4$) in the samples with lower Mo concentrations (6.25 wt.% and less) and the increase in Mo leach rate from glasses with greater Mo-contents was due to the release of the residual Mo in the glass. Nd release rates were very low, indicating that oxyapatite is more durable than the residual glass. Also, in the higher waste loaded glass-ceramic, there was a significant increase in the release rates of boron and sodium, leading to the conclusion that the residual glass is less durable than the crystalline phases.

Dissolution tests were performed on the glasses from the test matrix study [25]. Three different dissolution tests were used to develop an understanding of the chemical durability of the glass-ceramic. One test, a modified PCT method "B", static dissolution test, was used to analyze samples cooled following the CCC protocol after 7, 28, 119, 448 days on test. The second test was a single-pass flow-through, SPFT, test used on samples cooled at 4, 1, and 0.25 times the CCC-cooling rates [25, 42]. The third test was a modified single-pass flow-through, MSPFT, test used to further analyze the CCC cooled samples, combining weight loss measurements with corrosion depth measurements made using scanning electron microscopy [15, 25]. From the PCT tests, the effects of composition on the release of various components from the glass were determined; these are summarized in Table 1.8 [25]. Alkali-rich molybdates corrode faster than alkaline earth molybdates. B_2O_3 and Al_2O_3 tend to sequester the alkali ions in the glass phase as charge compensators, reducing the concentration of the alkali rich molybdate phases, increasing the overall durability.

Table 1.9 shows the release rates of different elements reported in a PCT study of the centroid sample, with B, Na, and Mo having the fastest leach rates [25]. The high Mo leach rate was attributed to the presence of low durability powellite phases. The SPFT dissolution tests showed that powellite dissolved faster than the residual glass, which dissolved faster than the oxyapatite phases, regardless of thermal history, pH, or flow rate [25]. This conclusion was based on the relative release rates of Mo from powellite, B from the residual glass, and La from oxyapatite. On the other hand, the MSPFT dissolution test indicated that the residual glass dissolved fastest among these three microstructural features.

Table 1.8. Compositional effects on elemental release rates [25].

Glass Component	**Trend increasing/decreasing release rates**
Al_2O_3, ZrO_2	decreases B, Li, Na, Cs, Si
SiO_2	decreases B, Cs
B_2O_3, Na_2O, MoO_3	increases B, Li, Na, Cs, Si
Ln_2O_3	increases B, Li, Na, CS
Li	increases B, Si / decrease in Li
CaO	no effect

Table 1.9. Normalized release rates from PCT of the centroid glass composition cooled with CCC (g/m^2) [25].

days	**B**	**Ca**	**Na**	**Nd**	**Mo**	**Ba**	**Si**
7	0.179	0.032	0.172	-	0.172	0.070	0.051
28	0.223	0.038	0.191	-	0.223	0.089	0.051
119	0.217	0.045	0.223	-	0.255	0.070	-
448	0.140	0.064	0.274	-	0.274	0.045	-

2. RESEARCH OBJECTIVE

The focus of the present study was to characterize the effects of thermal history on the microstructural development and properties of a borosilicate glass-ceramic waste form. For this study a borosilicate glass-ceramic designed to immobilize an estimated US commercial waste composition was used. Prior studies on glass-ceramics for this estimated waste stream have thus far developed a matrix of compositions with waste loadings up to 50 wt.% that precipitate chemically durable phases [25]. This study analyzed the centroid composition from that test matrix to develop a better understanding of the processes for microstructural development.

Prior studies on the centroid composition of the test matrix have yet to develop a TTT diagram describing the temperatures and times required to form different crystals [25]. The development of a TTT diagram is also required per the waste acceptance product specifications [7]. Prior studies are also uncertain about the release rate of certain species, especially Molybdenum, and whether the ions are released from the crystalline species or the residual glass [13, 15, 25, 40, 42].

In this study, microstructures have been characterized as a function of time and temperature using isothermal and constant cooling rate experiments. The experimental procedures for developing and characterizing samples that have been quenched at different rates from a melt as well as samples that have been quenched from a melt, held at an isothermal temperature for a fixed time, then quenched again to room temperature, are described. Time-Temperature-Transformation (TTT) diagrams, Continuous-Cooling-Transformation (CCT) diagrams, and activation energies for the growth of major phases that form in these samples are reported.

Furthermore, the effects of thermal history on the microstructural development of the glass-ceramic have been related to corrosion behavior in water. Chemical durability was characterized using the product consistency test (PCT) and by characterizing changes in surface topology using atomic force microscopy and profilometry. The relations between microstructure and chemical durability are discussed and this information is intended to be used to help engineer an optimized waste-loaded glass-ceramic.

PAPER

I. PHASE DEVELOPMENT IN A COMPLEX BOROSILICATE GLASS-CERAMIC WASTE FORM

Nicholas Roberts, Paul Porter, and Richard K Brow

Department of Materials Science & Engineering, Missouri University of Science & Technology, Straumanis-James Hall, 1400N. Bishop Ave, Rolla, MO 65409-0330

ABSTRACT

A borosilicate glass provided by PNNL was melted and quenched with different thermal histories to produce samples with a range of microstructures that were then described by analytical electron microscopy and quantitative x-ray diffraction. Slower quench rates and longer isothermal treatment times produced samples with greater fractions of crystalline powellite ($CaMoO_4$ and related phases) and oxyapatite ($Ca_2LN_8Si_6O_{26}$). A time-temperature-transformation, TTT, diagram was developed which shows that the fastest crystallization on cooling occurs at ~1000°C. The growth of these crystalline phases is accompanied by changes in the composition and morphology of the residual glass. Oxyapatite was found to form hollow hexagonal crystals, more spaced out and larger at temperatures ≥1000°C, and these filled-in with time. Crystalline molybdate phases were present as lanthanide-containing needles in samples held above about 1000°C and as alkaline earth-containing droplets when grown from a phase separated residual glass at

lower temperatures and times that precede oxyapatite crystal formation. Subsequently to the formation of oxyapatite and from a more homogeneous residual glass, molybdates phases were present as alkaline earth-containing crosses.

1. INTRODUCTION

A goal of the U.S. Department of Energy, D.O.E., Global Nuclear Energy Partnership, GNEP, is to develop spent nuclear fuel reprocessing technologies, such as the UREX process, to greatly reduce the volume of spent fuel that must be treated as a waste material [1, 2]. The D.O.E. Fuel Cycle Research and Development (FCRD) program is tasked with developing viable storage options for the wastes resulting from fuel reprocessing [3]. There are manufacturing cost benefits in combining the reprocessed waste streams and incorporating them into a single waste glass formulation [4].

Borosilicate glasses are used worldwide and are understood by the FCRD to be a viable option to immobilize nuclear waste [3, 5]. Borosilicate glasses exhibit favorable properties regarding the immobilization of nuclear waste [6], including excellent chemically durability, thermal and radiation stability, and mechanical integrity. Also, many waste elements are soluble in borosilicate melts, allowing high waste loadings in the quenched glass. Some elements, such as molybdenum, however, have low solubility, <3 wt.%, in borosilicate melts [7, 8, 9], limiting loadings from Mo-rich combined waste streams into a homogeneous borosilicate glass. Waste loading levels can be increased in borosilicate glass-ceramics if precipitated phases and residual glass possess requisite chemical durability.

Recently, researchers at Pacific Northwest National Lab (PNNL) have developed a borosilicate glass-ceramic composition to immobilize a waste generated by aqueous spent nuclear fuel reprocessing techniques [8, 10-16]. One of the goals of this development program, described in the preliminary Technology Maturation Plan, TMP, is to develop processes for the full-scale production of glass-ceramics to immobilize high level waste [17]. One outcome of the TMP is to “predict the amounts, types, and compositions of phases formed in the final, canistered waste form [17].” More specifically, in order to improve formulation and processing to ensure that an optimized waste-loading glass-ceramic is developed, models accurately predicting phase growth and crystallization as a function of thermal history are needed [12, 17]. The Waste Acceptance Product Specifications (WAPS) also require the development of time-temperature-transformation (TTT) diagrams to fully understand the crystallization pathways [18]. The WAPS is a set of acceptance specifications for high-level nuclear waste developed by the DOE.

Researchers at PNNL have developed production scale melting techniques for borosilicate glasses and have described crystallization and phase formation as a function of cooling rate for compositions similar to that in the present study [12, 15]. In that work, it was proposed that the melt would separate into Mo-rich and silicate-rich phases. Crystalline $BaMoO_4$ ($(Ba, Sr) MoO_4$) and $CaMoO_4$ ($(Ca, Sr) MoO_4$) would precipitate from the Mo-rich phase. The silicate-rich phase would further separate into a Cs-alumino-borosilicate liquid and an alkaline earth-lanthanide-silicate liquid, the latter of which would crystallize into oxyapatite. The present study is intended to determine the effects of time and temperature on these morphological and compositional transformations.

Prior isothermal heat treatment studies [10] of these borosilicate glass-ceramics involved samples that were quenched from the melt to room temperature, and then reheated and isothermally held at different temperatures for various times, as shown schematically in Figure 1a. In the present work, samples were either quenched from the melt directly to the isothermal temperature, held for desired times, then quenched again to room temperature, or were continuously cooled from the melt to room temperature at different rates, as shown in Figure 1b. Quenching directly from the melt more closely simulates the thermal history of a waste glass which will follow a nucleation and crystallization pathway significantly different from the more conventional quench and reheat experiments.

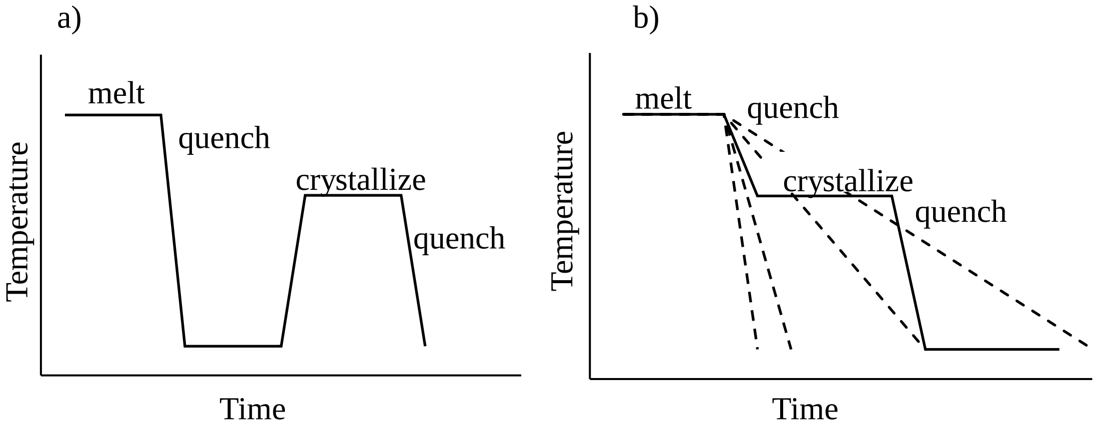

Figure 1. Schematic representations of isothermal experiments. a) Reheating quenched glasses to the treatment temperature. b) Quenching from the melt directly to the isothermal treatment temperature (solid lines) or quenching to room temperature at different fixed rates (dashed lines).

The focus of the present study is to characterize the effects of thermal history on the microstructural development of a borosilicate glass-ceramic waste form. Microstructures were characterized as a function of time and temperature through isothermal and constant cooling experiments. Time-Temperature-Transformation (TTT) and Continuous-Cooling-Transformation (CCT) diagrams, and activation energies for the growth of major phases that form in these samples, have been determined, with the intention of using this information to help engineer an optimized waste-loading glass-ceramic.

2. EXPERIMENTAL PROCEDURES

2.1. GLASS COMPOSITION

The glass-ceramic material used in these studies was produced at Pacific Northwestern National Lab (PNNL) as part of a larger material development program and was provided by Jarrod Crum (PNNL). Information about sample preparation can be found in reference [13]. Reagent grade raw materials were melted twice in covered Pt/10% Rh crucibles between 1250°C and 1450°C for an hour, then quenched on an Inconel plate in air. Figure 2 shows a picture of representative samples of these inhomogeneous materials, and Table 1 provides their nominal composition [13].

Figure 2. Optical image of the as-received glass. The darker side is the side of the melt that was in contact with the Inconel plate when the melt was quenched.

Table 1. Centroid glass-ceramic target composition [13].

Oxide	**Content [mol%]**	**Oxide**	**Content [mol%]**
SiO_2	47.674	TeO_2	0.641
B_2O_3	11.329	Sm_2O_3	0.481
CaO	8.445	Y_2O_3	0.433
MoO_3	4.229	Rb_2O	0.353
Al_2O_3	3.789	RuO_2	0.232
Na_2O	4.069	CdO	0.135
ZrO_2	3.774	SeO_2	0.116
Li_2O	3.247	RhO_2	0.089
Nd_2O_3	2.427	Eu_2O_3	0.076
BaO	2.241	Ag_2O	0.075
Cs_2O	1.591	SnO_2	0.072
SrO	1.476	Gd_2O_3	0.070
Ce_2O_3	1.472	PdO	0.023
La_2O_3	0.757	Total	100.000
Pr_2O_3	0.684	Waste Loading	47.394 wt.%

2.2. CONTINUOUS COOLING EXPERIMENTS - MELT QUENCHING TECHNIQUES

Fast quench rates, several hundred °C/s, were achieved using a custom-built dual roller system (Figure 3, left). The 8 inch (circumference), water-cooled stainless-steel rollers were set with a gap spacing of 0.25 mm and a rotation rate of 1140 rpm powered by a ½ HP motor. As-received glass was melted at 1300°C in a platinum crucible for 1 hour and the melt was poured directly between the rollers to produce glass ribbon ~0.25 mm thick (Figure 3, right).

Two wedge molds, made from different metals but with the same wedge dimensions, were used to quench melts at rates between about 4°C/s and 45°C/s, Figure 4. One mold was made from copper and was water-cooled to produce a faster range of quench rates than the second mold which was made of stainless steel and was air cooled. Sheathed type-K thermocouples were inserted through the sides of the mold to the centers of each of the steps. Further information about the wedge mold experiments is provided by Maldonado and Peterson [19, 20]. About 100 grams of as-received glass was melted at 1300°C in a platinum crucible for 1 hour and then the melt was immediately poured down the center of the mold, onto each of the eight thermocouples to record individual cooling rate profiles using a portable data logger (Graphtec midi logger GL 220) that recorded temperatures ten times every second. Once the sample was cooled, the mold was opened, and samples were collected near each thermocouple junction for microstructural analyses.

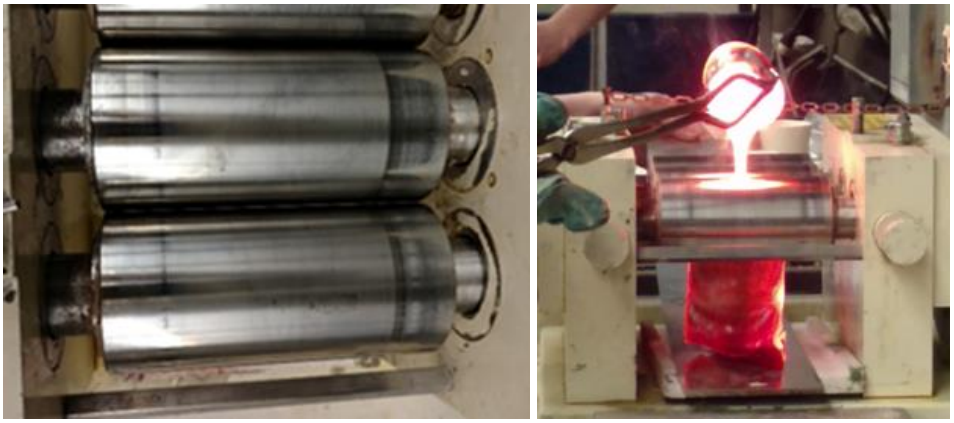

Figure 3. Roller quenching system.

In another set of experiments, about ~30 grams of as-received glass was melted for one hour at 1300°C in a platinum crucible. The crucible was removed from the melting furnace and a K-type thermocouple was then inserted into the melt (Figure 5). One crucible was then allowed to cool to room temperature in air at an average rate of ~3.5°C/s. The second crucible was transferred to a preheated annealing furnace at 1100°C that was then shut-off to allow the glass to cool at a much slower rate (~0.1°C/s). A third sample was transferred to an annealing furnace set at 1150°C that was programmed to cool following the canister centerline cooling (CCC) profile, summarized in Table 2 [8]. The CCC profile corresponded to an average cooling rate of ~0.005°C/s, from 1150°C to 600°C. At the completion of each of these three crucible experiments, material near the tip of the respective thermocouple was collected for microstructural characterization.

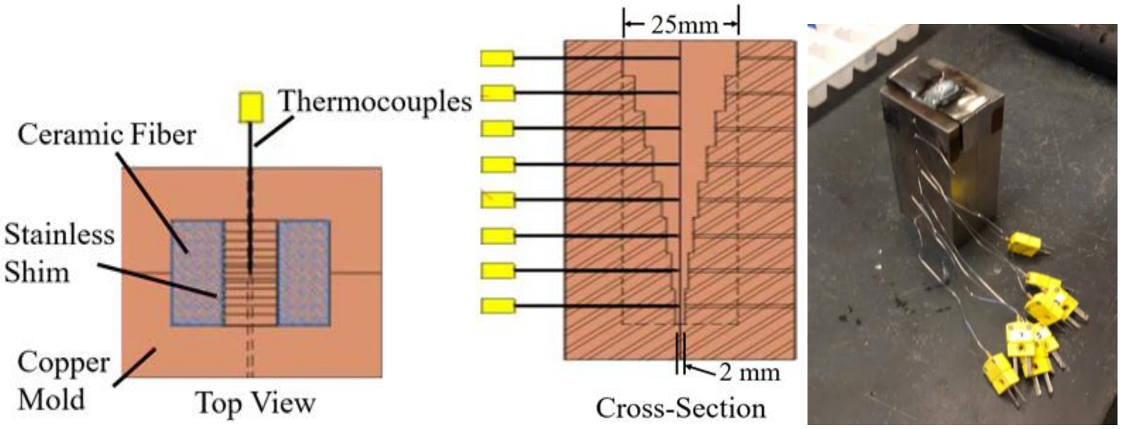

Figure 4. Schematic diagrams of assembled water-cooled copper wedge mold (left and center) and a photograph of the steel wedge mold (right).

Figure 5. Furnace cool experiment with embedded thermocouple.

Table 2. Treatment schedule comparable to the CCC of a waste storage canister [8].

Step	Start Temperature (°C)	Rate (°C/min)	Step Duration (hours)
1.	1200 - 1150	0	Preheat 0.5 hours then fast cool
2.	1150 - 1050	~ -7	0.2
3.	1050 - 950	-0.935	1.8
4.	950 - 886	-0.288	3.7
5.	886 - 845	-0.108	6.3
6.	845 - 626	-0.205	17.8
7.	626 - 400	-0.126	29.9
8.	400	0	Dwell 1 hour

2.3. ISOTHERMAL EXPERIMENTS - MELT QUENCHING TECHNIQUES

Molten tin was used to rapidly quench and thermally equilibrate melt samples in the isothermal experiments. The tin was contained in either an alumina or a graphite crucible that was then held in a furnace. Argon gas was flowed over the molten tin surface to minimize oxidation. A thermocouple in a closed-end alumina tube was immersed in the tin bath to record the temperature throughout the experiments. Tin bath temperatures changed with time when samples were first transferred from the melting furnace to the tin bath, and average temperatures over the course of an isothermal holding time are reported.

Three different tin bath configurations were used in these experiments, as shown in Figure 6. The four-crucible box furnace tin bath arrangement shown in Figures 6a and b, was used for isothermal experiments between 600 and 800°C. These alumina crucibles contained ~250 cm^3 of molten tin, and temperatures fluctuated up to 15°C in some experiments. This configuration was also used by Peterson [20]. The second configuration used a larger graphite crucible to hold a larger volume of molten tin (500 cm^3) to reduce temperature fluctuations and operated in a kiln that could go to temperatures as high as ~1050°C, Figure 6c and d. The third configuration used the same larger volume of tin but operated in an annealing furnace that reached 1100°C. Supplemental information about the different tin baths can be found in Appendix A.

As-received glass was crushed using a steel impact mortar and about 5 grams of powder was packed inside a crimped 304 stainless steel tube, 0.25” OD, 0.23” ID, ~6” length. These tubes were sealed at the open end with a stainless-steel rod which was then used to lower the tube into a melting furnace set at 1300°C and held here for 90 seconds to melt the glass. The tubes were removed from the furnace and immediately plunged into a molten tin bath set at the desired temperature and held for the specified treatment time, after which the sample tubes were then removed from the molten tin and immediately quenched in room temperature water. Once fully quenched, the tubes were sectioned using a diamond saw and material was prepared for characterization. Only material from the centers of the tube that were fully submerged in the tin bath were characterized.

In this report, samples that were held in tin baths between 600°C and 1100°C, from 0.5 to 60 minutes, are described. In addition, a sample that was quenched directly from 1300°C to room temperature water was prepared as a baseline against which the isothermally heat-treated samples are compared. Furthermore, a sample held at 900°C for 24 hours was prepared and characterized.

2.4. SAMPLE CHARACTERIZATION

2.4.1. X-ray Diffraction. Representative samples with different thermal histories from the continuous cooling and isothermal hold experiments were ground with a mortar and pestle and sieved to <45 µm. Some of these powders were mixed with 10% (by weight) SRM 674 standard rutile, (TiO_2), and used in the quantitative x-ray diffraction (XRD) study. Powders were pressed into standard 2.5 cm diameter powder mounts and analyzed using a Philips X’pert multipurpose diffractometer (PIXcel detector, Cu Kα radiation, at 45 kV and 40 mA, and a 0.38 fixed divergence slit). Hour long scans were taken from 9.995º to 70.000º 2θ with a step size of 0.026º. PANalytical HighScore software was used to identify crystalline phases. If required, MDI RIQAS software was used to perform Rietveld analysis to compare peak intensities with the known intensities of the rutile standard. Comparable peak broadening and subtracted baseline factors were used on all patterns to determine the relative weight fractions of different crystalline phases and the residual glass from the Rietveld analyses. Samples were collected from several repeated isothermal heat treatment experiments, and other samples were prepared and repeated at least twice to determine the uncertainties of the quantitative XRD analyses. These repeat experiments indicate a relative uncertainty in the quantitative phase analyses of about 20% (Table A.2, Appendix A). The difference between the Rietveld fit and the measured pattern shows very little peaks proving the fit to strongly match the measured pattern, Figure A.9 in Appendix A.

2.4.2. Analytical Electron Microscopy. An FEI Helios NanoLab 600 FIB/FESEM scanning electron microscope (SEM) equipped with an Oxford energy dispersive spectrometer (EDS) was used to characterize the various phases that formed in heat-treated samples. Representative samples were mounted in epoxy, polished to a 0.25 µm diamond suspension finish, masked with copper tape, and sputter coated with an Au/Pd film before loading into the SEM. Images were obtained at various magnifications, electron voltages, and beam currents. EDS spectra and maps were obtained using Oxford Instruments AZTEC software at various magnifications using 15 keV and 1.4 nA electron beam. ImageJ software was used to quantify microstructural features.

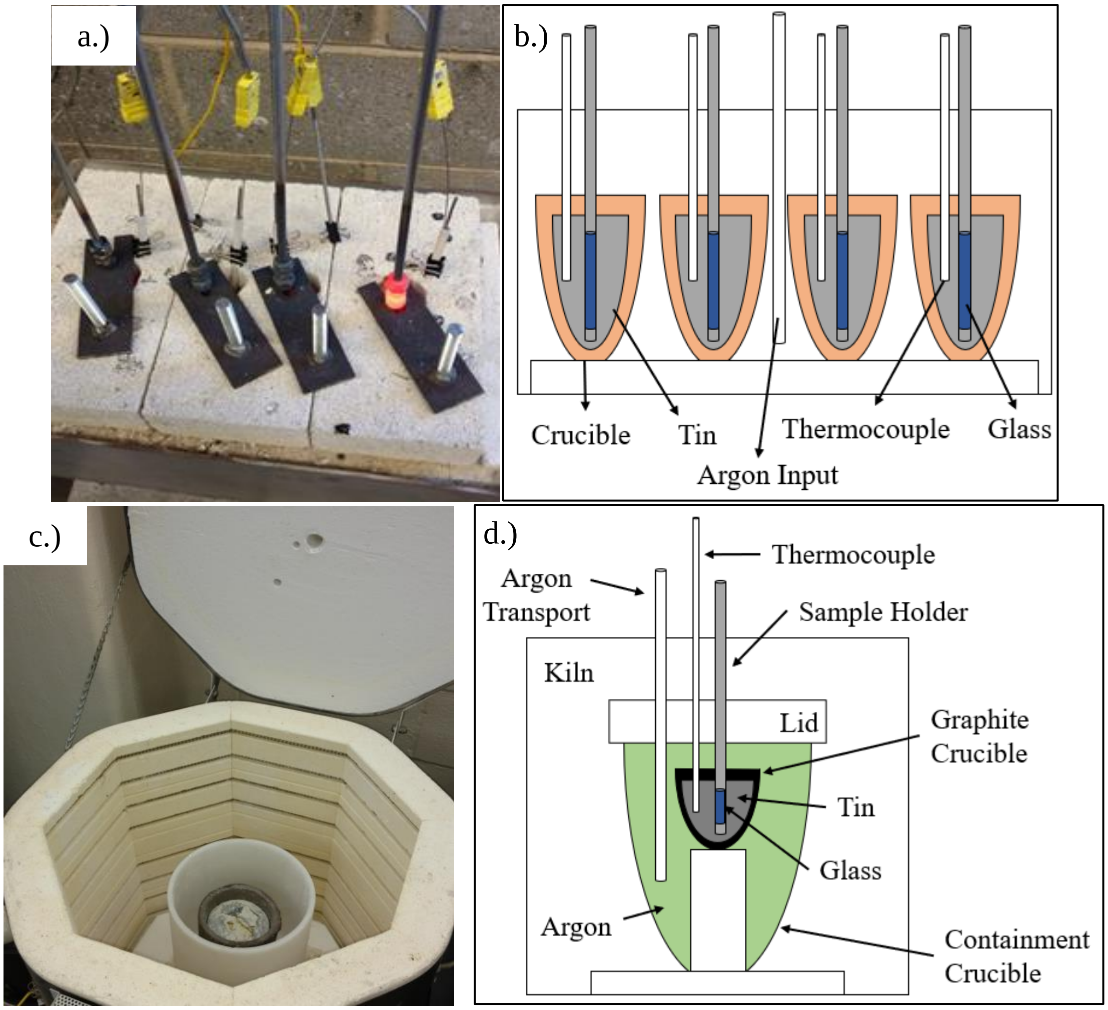

Figure 6. a) Photograph and b) schematic illustration of the set-up for the small volume isothermal tin bath. c) Photograph and d) schematic illustration of the set-up for the large volume isothermal tin bath.

Some samples were also characterized using a transmission electron microscope/scanning transmission electron microscope, TEM/STEM, (FEI Tecnai G2 F20 S-Twin). Samples were ground to a powder (<45 µm) using a mortar and pestle, then dispersed on a copper grid and loaded into the TEM. Another TEM sample was prepared by milling a section ~100 nm thick from a polished bulk glass sample using the Focused Ion Beam (FIB) with the FEI Helios NanoLab 600 dual beam system. Before the final milling the sample was transferred to a copper grid using an Omniprobe and later the specimen attached to the copper grid was loaded into the TEM. TEM examinations were performed at various magnifications, an acceleration voltage of 200 keV and an emission current of 80 μA. Micrographs were collected using annular bright field/dark field detectors. Energy dispersive X-ray spectroscopy, EDX, spectra was collected using an Oxford ultra-thin window (EDX) detector. Selected area diffraction (SAD) patterns along zone axes were collected using a Gatan ORIUS wide-angle charge-coupled device (CCD).

2.4.3. Raman Spectroscopy. Raman spectra were collected from polished samples with a Horiba Jobin YVON LabRAM Aramis μ-Raman spectrometer, using a 632.8 nm HeNe laser under a 100x magnification objective with an 1800gr/mm grating. A silicon reference sample was used to calibrate the energy scale. Ten spectra were averaged over ten seconds and at least three areas of the desired phases were examined in every case to ensure that representative spectra were reported.

2.4.4. Differential Thermal Analysis. Differential thermal analysis (DTA) data was collected on some samples (Perkin Elmer Differential Thermal Analyzer DTA 7 with Pyris software). Powders samples (~25mg) were heated in Pt crucible at 10°C/min in a Nitrogen atmosphere to 1200°C. Thermal data was compared to an Al_2O_3 reference.

3. RESULTS AND DISCUSSION

3.1. SAMPLE OBSERVATIONS

The as-received glasses are visibly heterogeneous, and all glasses produced from the various quenching and isothermal experiments, including the roller quenched glass, are also visibly heterogeneous. For example, Figure 2 shows an optical micrograph of the top side and the bottom side of the as-received glass; the latter was cooled faster with direct contact to the Inconel plate causing this surface to be darker in color.

Samples from the continuous cooling experiment were sent to Savanah River National Laboratories (SRNL) to measure the compositions after remelting in Pt at 1300°C for 60 min. Compositions were measured using ICP-AES and ICP-MS and are compared to the nominal composition, Figure A.10, A.11, and A.12 of Appendix A, showing a good fit with most components. Cs compositions were measured to be slightly lower due to Cs volatilizing.

Figure 7 shows optical images of the cross-sections of representative samples sectioned from the stainless tubes from different isothermal experiments. The sample on the left was held at 1300°C for 90 seconds and then quenched into a tin bath at 800°C, held for 0.5 minutes and finally quenched into room temperature water. The center sample and the sample on the right were also isothermally heat-treated at 800°C, but held for 4 and 60 minutes, respectively. The cracks in these samples likely resulted from thermal shock induced in the glass during the water quench.

3.2. TIME-TEMPERATURE PROFILES

For the wedge-mold experiments, the melt was too viscous to flow into the narrowest (2mm) bottom (8th) step, so samples with seven different quench rates were obtained from each of these experiments. The thermal profiles measured from the wedge mold and crucible quench experiments are compared in Figure A.1 of Appendix A. The measured thermal profile of the CCC sample was very similar to the programed furnace and appears to have converged after 20 minutes, as shown in Figure A.2 of Appendix A.

Quench rates were calculated from the respective times it took to cool each sample from their highest recorded temperature to 590°C, and these are given in Table 3 along with the maximum recorded temperature for each experiment. The cooling rates are calculated to 590°C because this is the glass transition temperature of the as-received glass that was measured using differential thermal analysis; the DTA data are shown in Figure A.3 of Appendix A.

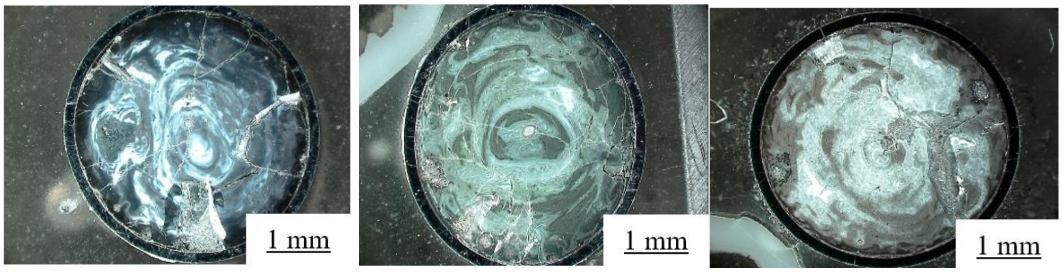

Figure 7. Optical images of as-received glass melted in a stainless-steel tube at 1300°C for 90 seconds and then left) quenched into an isothermal tin bath at 800°C and held for 0.5 minutes before quenching in water; center) quenched into an isothermal tin bath at 800°C and held for 4 minutes before quenching in water; and right) quenched into an isothermal tin bath at 800°C and held for 60 minutes before quenching in water.

Figure 8 shows the quenching profile recorded from a thermocouple that was inserted into a stainless-steel tube, packed with as-received glass, placed into the 1300°C furnace, melted for 90 seconds, and then quenched into room temperature water. This profile indicates this baseline sample was quenched at rate nearly 300°C/s. Figure 8 also shows the measured temperature profile recorded from a thermocouple inserted into a stainless-steel tube packed with glass, placed in a furnace at 1300°C for 90 seconds quenched in a tin bath at 600°C, held for 4 minutes, and quenched to room temperature. Quench rates from these experiments are listed in Table 3. The quench rate of the roller quenched samples was not measured, but based on the phases present in these samples, as discussed below, was at least as fast as the baseline quenched sample.

Table 3. Quench rates for continuously cooled and some isothermal samples, calculated from the time between the maximum recorded temperature and when the sample reached 590°C.

<table>
<tr><th colspan="5">Continuous Cooling Experiments</th></tr>
<tr><th>Quench Method</th><th colspan="2">Maximum Temperature Recorded [°C]</th><th colspan="2">Average Quench Rate [°C/s]</th></tr>
<tr><td>CCC</td><td colspan="2">1150</td><td colspan="2">0.008</td></tr>
<tr><td>Furnace Cool</td><td colspan="2">1119</td><td colspan="2">0.1</td></tr>
<tr><td>Air Cool</td><td colspan="2">1124</td><td colspan="2">3.4</td></tr>
<tr><td>Roller Quench</td><td colspan="2">-</td><td colspan="2">~300 - 1000</td></tr>
<tr><th>Wedge Molds</th><th>Copper</th><th>Steel</th><th>Copper</th><th>Steel</th></tr>
<tr><td>Step 1 (25 mm)</td><td>1241</td><td>1190</td><td>5.1</td><td>4.1</td></tr>
<tr><td>Step 2 (20 mm)</td><td>1232</td><td>1168</td><td>5.8</td><td>4.3</td></tr>
<tr><td>Step 3 (16 mm)</td><td>1204</td><td>1181</td><td>8.7</td><td>6.3</td></tr>
<tr><td>Step 4 (12 mm)</td><td>1223</td><td>1197</td><td>12.1</td><td>9.4</td></tr>
<tr><td>Step 5 (8 mm)</td><td>1208</td><td>1179</td><td>18.1</td><td>15.3</td></tr>
<tr><td>Step 6 (6 mm)</td><td>1149</td><td>1102</td><td>24.6</td><td>20.5</td></tr>
<tr><td>Step 7 (4 mm)</td><td>1011</td><td>955</td><td>42.8</td><td>33.8</td></tr>
<tr><th colspan="5">Isothermal Experiments</th></tr>
<tr><th colspan="2">Quench Description</th><th colspan="3">Quench Rate [°C/s]</th></tr>
<tr><td colspan="2">1300°C to water quench (baseline)</td><td colspan="3">294 ± 40</td></tr>
<tr><td colspan="2">1300°C to 600°C tin bath</td><td colspan="3">43 ± 10</td></tr>
<tr><td colspan="2">600°C tin bath to water quench</td><td colspan="3">50 ± 3</td></tr>
</table>

3.3. PHASE IDENTIFICATION

Phases were identified in each sample using XRD, SEM EDS, and TEM EDS. In some samples, some phases were either x-ray amorphous or in amounts too small to be detected using XRD. TEM was used to determine phases too small to be analyzed with the

SEM. TEM electron diffraction was also used on samples that were determined to be x-ray amorphous.

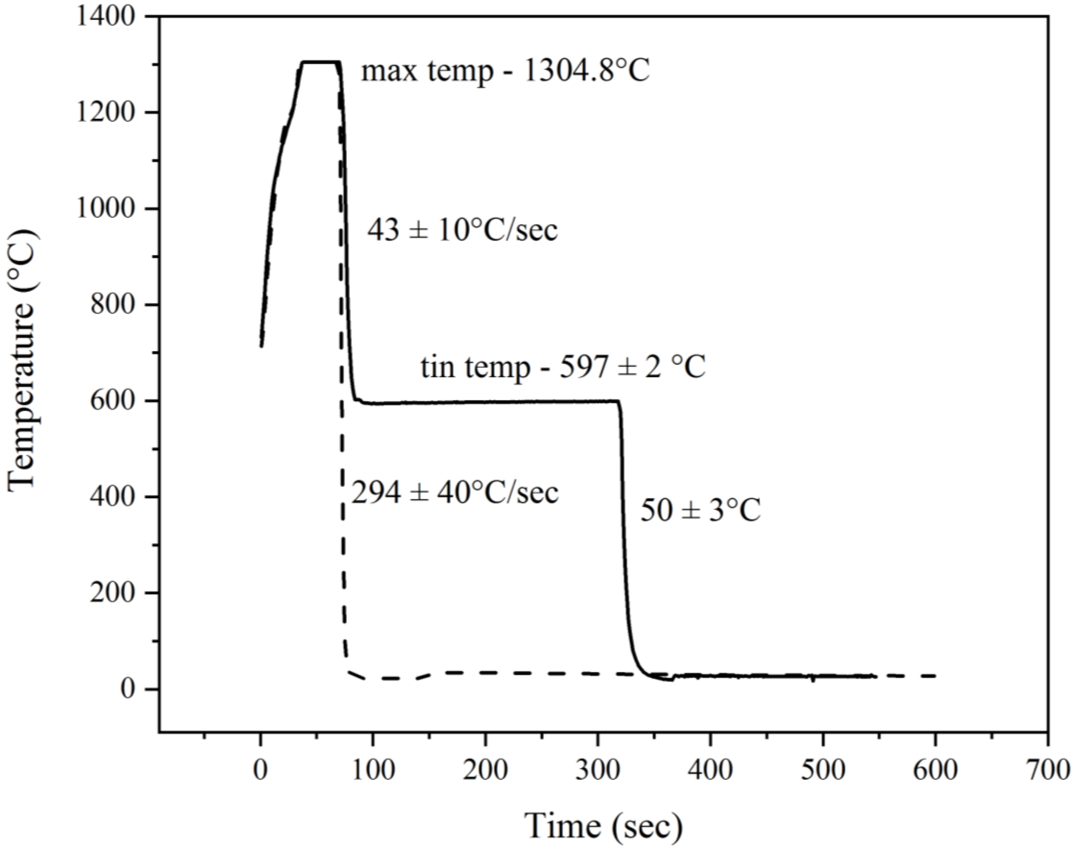

Figure 8. Cooling rate profiles for a thermocouple in a packed stainless-steel sample tube quenched in water bath (dotted line) and a thermocouple in a packed stainless-steel sample tube quenched in a tin bath set at 600°C, then quenched in water bath (solid line).

3.3.1. Phases Identified in the Continuously Cooled samples. Figure 9 shows the general trend in phase development from a mostly homogenous glass in a sample quenched at high rates, Figure 9a, to a developed glass-ceramic in the slower cooled samples. First, the glass is seen to separate into a droplet phase, dark circles, and a matrix phase with Mo-rich spherical particles, white circles, shown in Figure 9b. Next, oxyapatite, $Ca_2LN_8Si_6O_{26}$, crystallizes in which different morphologies are found at different cooling rates. Oxyapatite is the hollow hexagonal features in Figure 9c and the dendritic type features in Figure 9d.

Scanning electron microscopy (Figure 10) provided evidence for a ruthenium-rich phase in every sample, including the roller quench samples. These phases were unevenly dispersed, and often agglomerated. Heavy metal phases are known to be insoluble in borosilicate glasses, at least to temperatures of 1300°C [8].

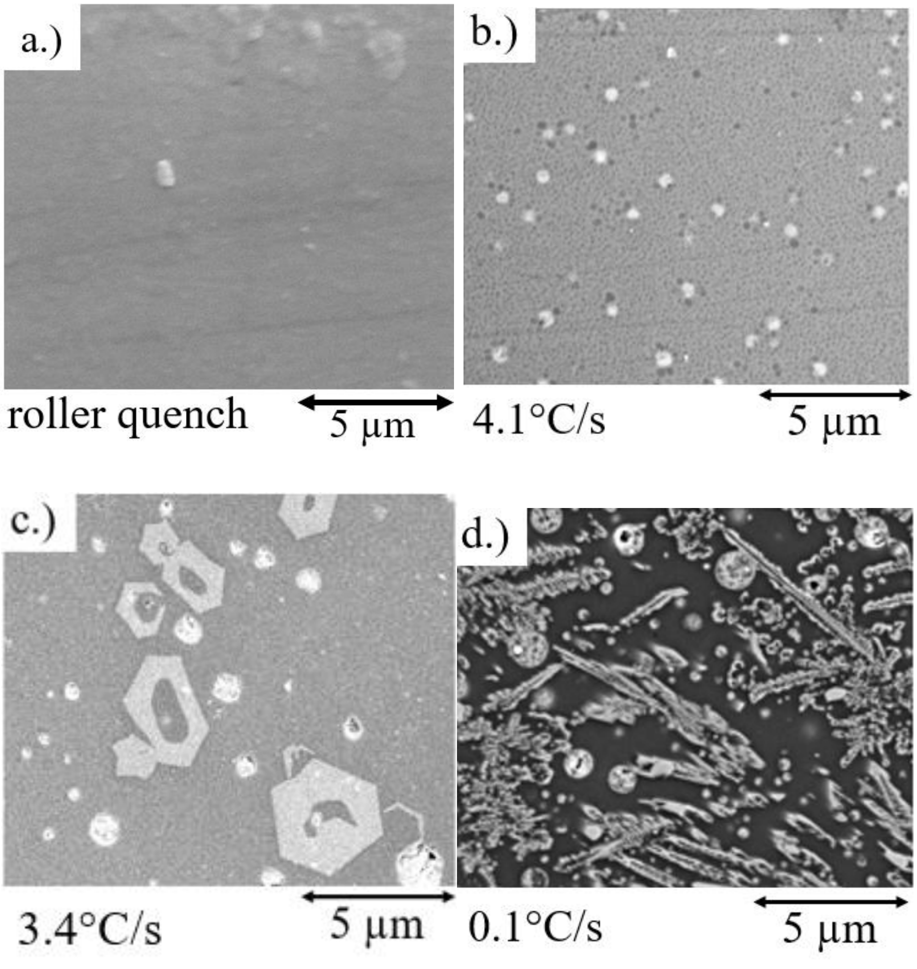

Figure 9. SEM micrographs of a) roller quench, b) 4.1°C/s, c) 3.4°C/s, and d) 0.1°C/s.

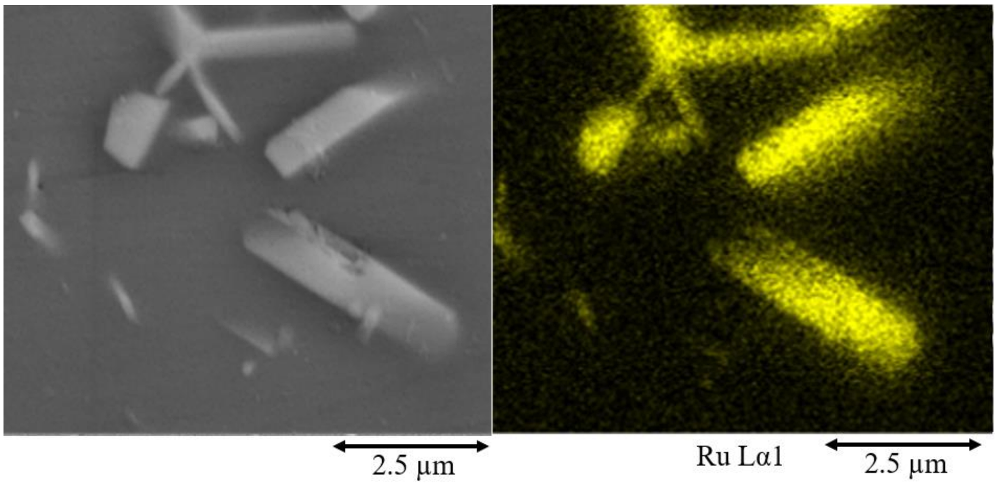

Figure 10. Scanning electron image (left) and Ru EDS map (right) of precious metal crystallites found in the roller quenched glass.

Figure 11 shows representative x-ray diffraction patterns for samples quenched at different rates. The CCC, 0.1°C/s and 3.4°C/s samples were doped with 10 wt.% SRM 674 rutile standard (PDF# 04-008-7848). Samples quenched at rates faster than about 4.1°C/s were mostly amorphous, showing only one significant peak near 28° (2θ) and three smaller peaks at 33° 45° 56° (2θ). These peaks closely match those associated with a strontium lanthanum molybdate phase ($Sr_{0.44}La_{0.39}(MoO_4)$, PDF# 04-002-4182) and this is further discussed in Appendix A. In the more slowly quenched samples, < 3.4°C/s, oxyapatite (e.g., $Ca_{1.1}Nd_{3.9}(SiO_4)_3O_{0.95}$, PDF# 04-007-5969) is clearly the major crystalline phase and crystalline powellite (e.g., $CaMoO_4$, PDF# 04-013-6764) was also identified. A peak at ~27° (2θ) is also present in the patterns collected from the samples cooled at 3.4°C/s and 0.1°C/s, and this is assigned to a barium strontium molybdate phase (e.g., $Ba_{0.75}Sr_{0.25}(MoO_4)$, PDF# 04-019-9425).

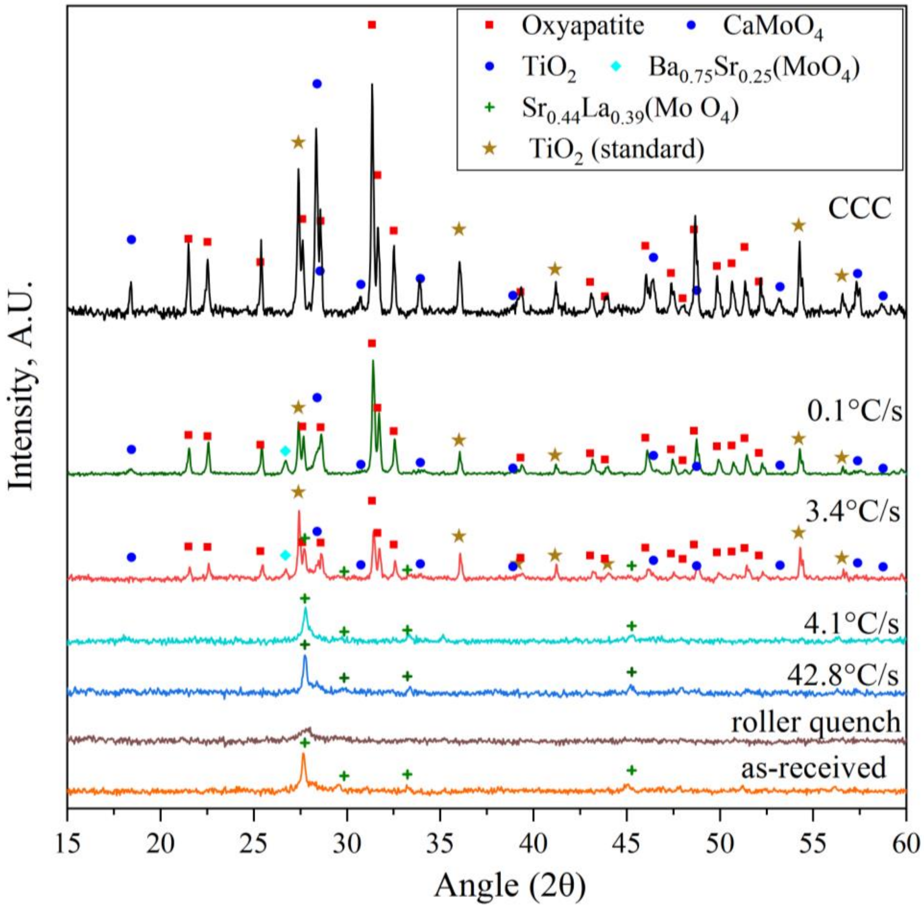

Figure 11. XRD patterns from the as-received glass cooled at various rates with the peaks assigned to the identified phases.

Figure 12 shows examples of X-ray maps from the EDS analyses used to identify the elements in the different phases that form in a quenched sample, including Ca and Nd in the oxyapatite crystals and Mo, Ba, and Ca in the powellite crystals. Sodium does not appear to be a major component in the latter phases, a preferred condition due to the poor chemical durability of $NaMoO_4$ [15]. Figure 13 shows an example where the powellite have separated into Ba-rich molybdate and Ca-rich molybdate phases. Crystalline powellite only could be detected by x-ray diffraction in samples cooled at 3.4°C/s and slower (Figure 11). Similar Mo-rich phases were found by SEM EDS in samples quenched faster than 4.1°C/s, and up to at least 42.8°C/s, and, TEM electron diffraction confirmed that the Mo-rich droplet phase in a sample quenched at 4.1°C/s was crystalline, as shown in Figure 14. Additional information on the selected area diffraction (SAD) pattern, Figure 14 can be found in Appendix A.

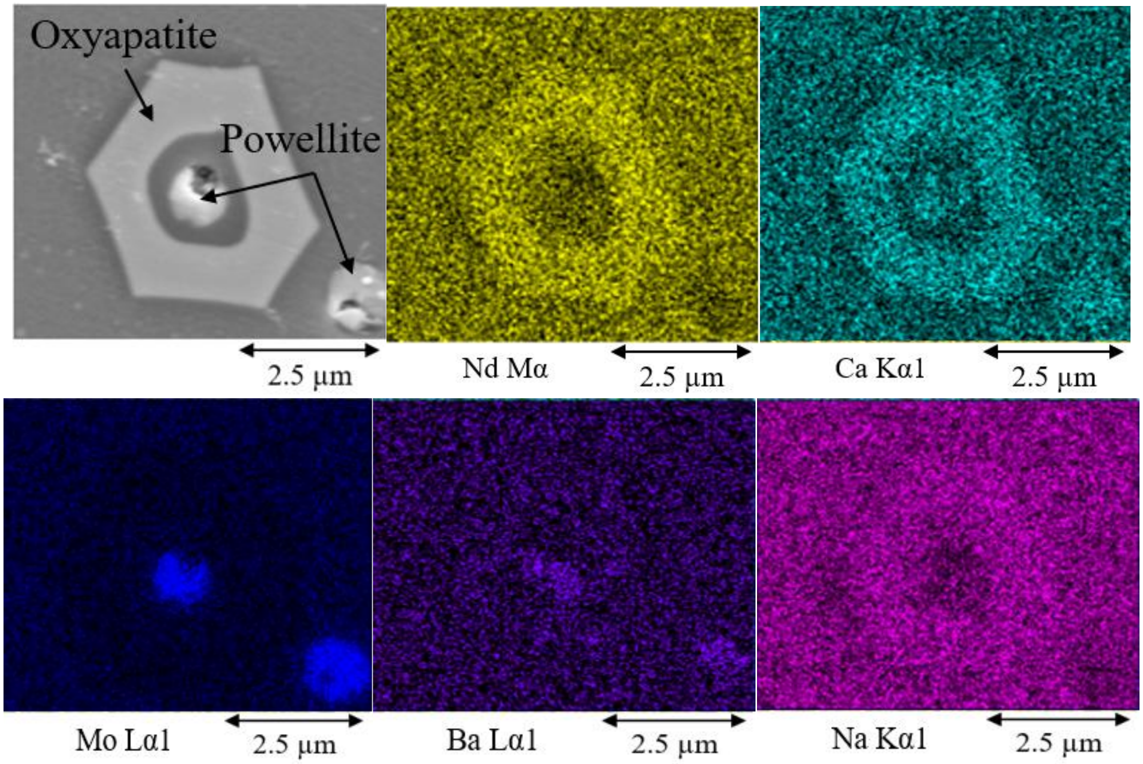

Figure 12. An SEM image and Nd, Ca, Mo, Ba, and Na X-ray maps collected from oxyapatite and powellite particles formed in a sample quenched at 3.4°C/s.

3.3.2. Phases Identified in the Isothermal Samples. Similar phases were identified in the samples from the isothermal quench experiments. For example, Figure 15 compares the XRD patterns collected from the as-received glass, the glass that was quenched at ~300°C/s directly from 1300°C to room temperature water, and the samples quenched from 1300°C to 900°C, held for various times, and then quenched in room temperature water. An XRD pattern from a sample melted at 1300°C and held isothermally at 1100°C for 60 min before water quenching is also shown for comparison. The isothermal samples were also doped with 10% SRM 674 standard rutile for the quantitative x-ray analysis. The pattern from the as-received sample has peaks assigned to the $Sr_{0.44}La_{0.39}(MoO_4)$ (PDF# 04-002-4182) phase that do not appear to be present in the pattern from the "baseline" quenched sample; the pattern from this latter sample possesses only a broad, amorphous hump. Electron microscopy revealed that sub-micron Mo-rich droplets could still be detected in the rapidly quenched baseline sample, as shown in Figure A.5 of Appendix A. The difference in XRD patterns between the "as received" and "baseline" samples, and the smaller Mo-rich droplets in the baseline sample, discussed in Section 3.4.4, suggests that melting the samples at 1300°C for 90 seconds successfully "reset" the glass microstructure before the start of each isothermal experiment. There are peaks in the XRD patterns from the isothermal samples near 41° (2θ) that do not appear in the patterns from the continuously cooled samples (Figure 11), and this may be due to some contamination from the stainless-steel tubes used in the former experiments. Some Cr, Fe, and Ni from the steel was concentrated in the glasses to a depth of about 20 µm from the tube wall, and it is possible that some transition metal oxide, like $FeCr_2O_4$, has contaminated isothermal samples after longer times at greater temperatures. Figures A.6 and A.7 in Appendix A provides additional information about this contamination.

The first unambiguous new crystalline phase that formed in the isothermal samples is oxyapatite (e.g., $Ca_{1.1}Nd_{3.9}(SiO_4)_3O_{0.95}$, PDF# 04-007-5969). Oxyapatite was found after an isothermal hold for at least 1 minute at 900°C and is clearly present in the XRD pattern of the sample heat treated for 2 minutes at 900°C, as shown in Figure 15. Crystalline powellite (e.g., $CaMoO_4$, PDF# 04-013-6764) was detected in the isothermal samples held for 4 minutes at 900°C, as indicated by the peak at 18.5° (2θ).

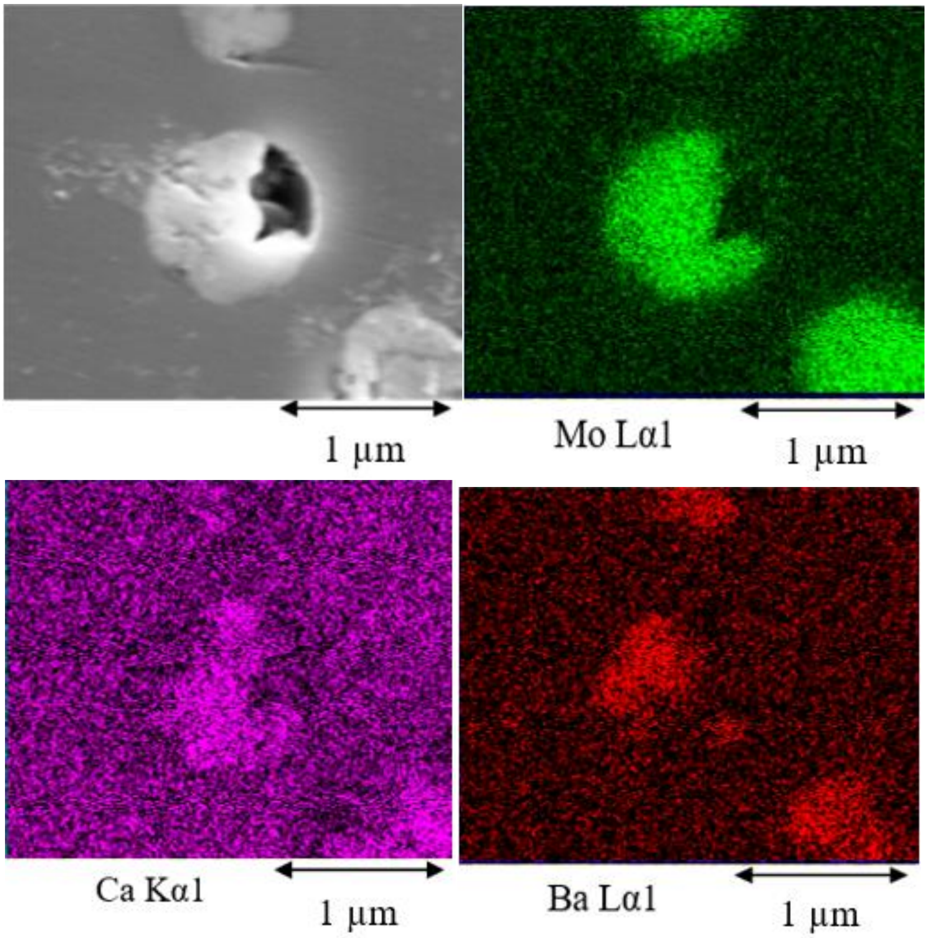

Figure 13. Electron image and Mo, Ba, and Ca X-ray maps collected of a molybdate particle formed in a sample quenched at 3.4°C/s. The particle is separated into a Ba-rich crystal and a Ca-rich crystal.

The XRD patterns from samples heat treated at 1100°C reveal several different peaks than what were found in the patterns of samples held at 900°C. Oxyapatite (e.g., $Ca_{1.1}Nd_{3.9}(SiO_4)_3O_{0.95}$, PDF# 04-007-5969) was detected but crystalline powellite (e.g., $CaMoO_4$, PDF# 04-013-6764) was not. Instead, there is evidence for the presence of other

Mo-rich phases, including $CaSr_2MoO_6$ (PDF# 00-048-0800, 30.625° 2θ) and $Sr_{0.5}Ca_{0.5}MoO_3$ phase (PDF# 04-021-8196, 32° 2θ). Needle shaped Mo-rich crystals were found in samples held at 1100°C, and these needles were also rich in lanthanides, as shown in Figure 16. The peak at 24.5° 2θ in the XRD pattern from the sample heated at 1100°C for 60 minutes could indicate the presence of $Nd_2Mo_6O_{21}$ (PDF# 00-032-0675).

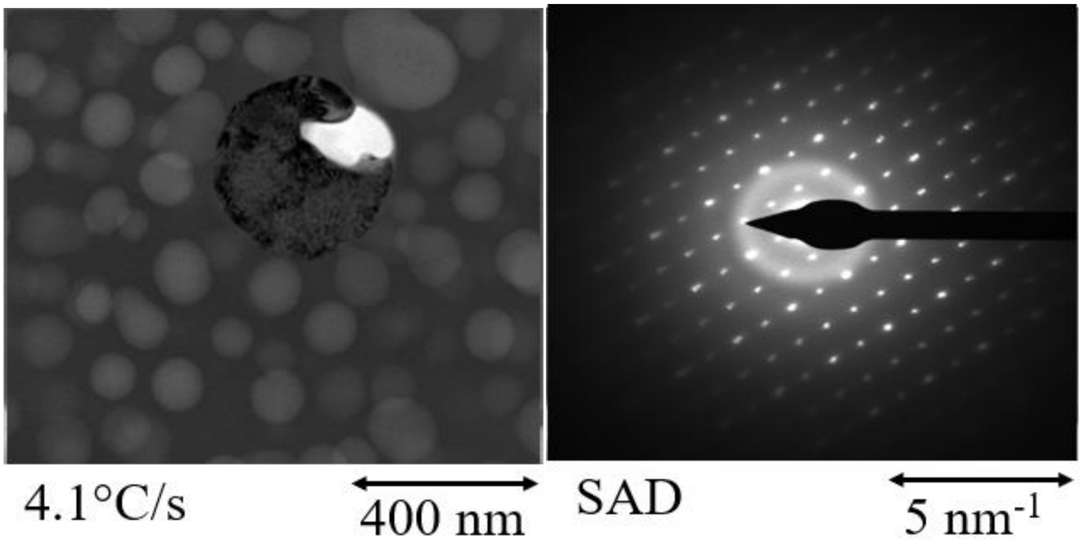

Figure 14. TEM electron image and selected area diffraction (SAD) pattern of a Mo-rich particle in the 4.1°C/s sample showing diffracted spots indicitive of crystalline materials.

3.4. PHASE MORPHOLOGY AND COMPOSITION

Analytical SEM, TEM, and Raman spectroscopy were used to characterize the morphology and composition of the various phases that form in samples with different thermal histories. In the following sections, the effects of heat treatment on the microstructures and compositions of the residual glass, oxyapatite, and molybdate phases are described.

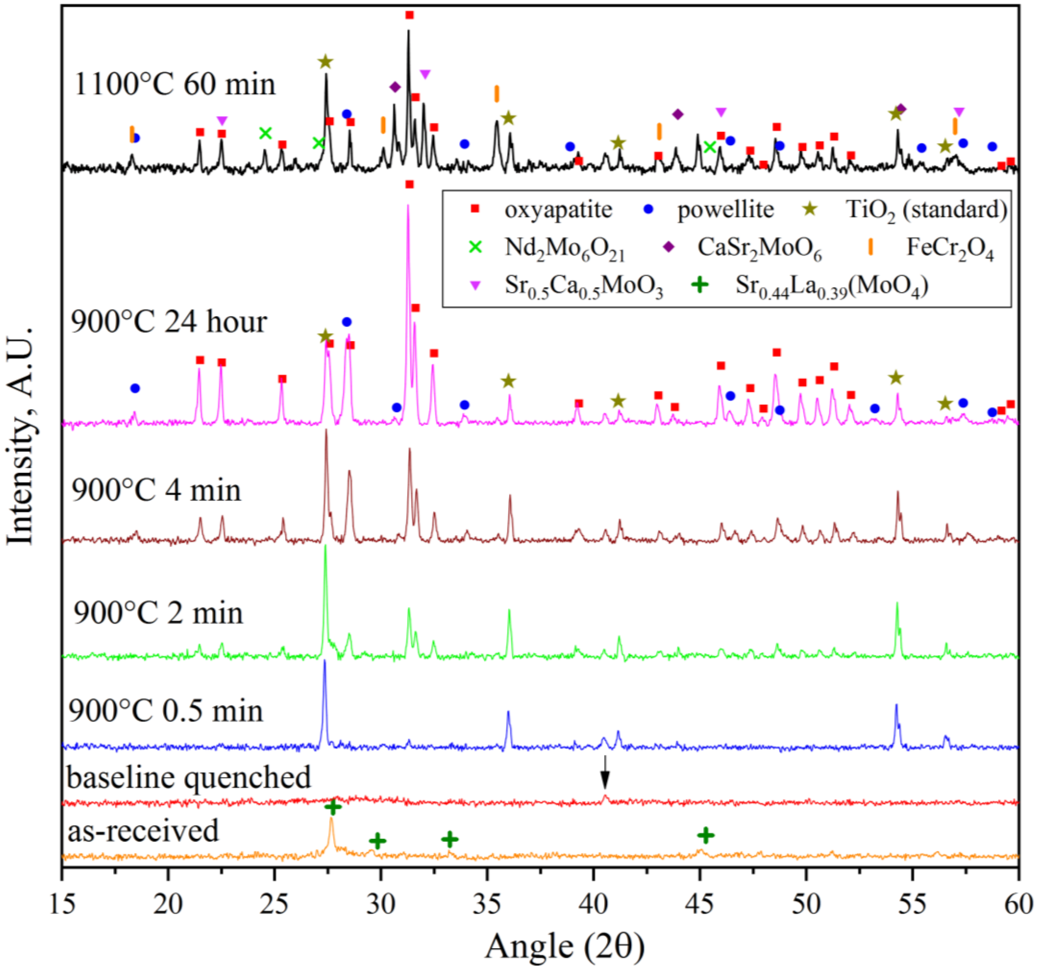

Figure 15. XRD patterns of as-received glass, baseline quenched sample (~300°C/s), samples heat-treated for various temperatures at 900°C, and heat treated at 1100°C for 60 min. The peak at 41° (2θ) marked with a black arrow is due to an unidentified phase that does not appear in the continuously cooled samples.

3.4.1. Residual Glass Morphology and Composition. The complex borosilicate glass studied here formed a droplet-in-matrix phase separated morphology. For example, Figure 17a shows a TEM image of a roller quenched sample with droplets <0.1 μm in diameter. A similar morphology exists in the wedge mold sample cooled at 4.1°C/s shown in Figure 17b, although the droplets in this sample were larger (0.13 ± 0.03 μm) than in the roller-quenched sample. Figure 17c shows an SEM image of the microstructure of a sample quenched at 3.4°C/s, where larger Mo-rich droplets (light phase) can be seen in the phase separated residual glass. The droplets in this residual glass were smaller, 0.05 ± 0.02 µm.

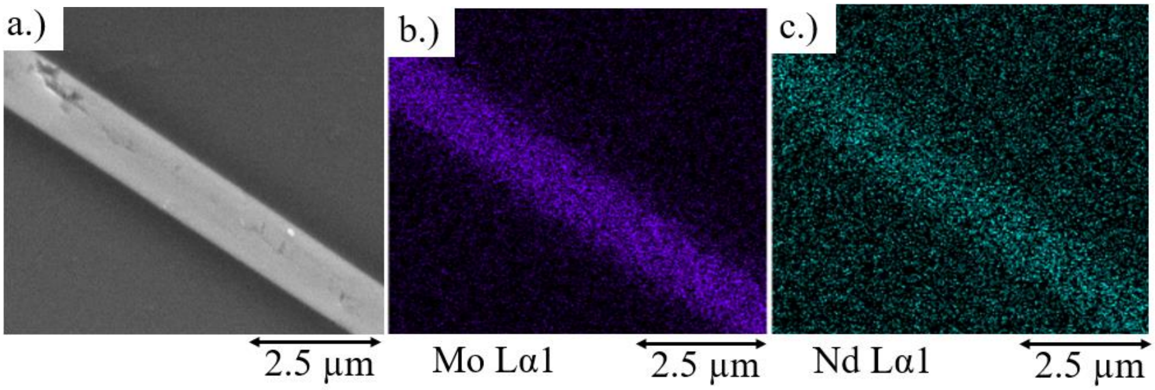

Figure 16. a) SEM electron image of the sample heat treated at 1100°C for 60 min of a Mo-rich phase also containing lanthanides, b) Mo EDS map, and c) Nd EDS map.

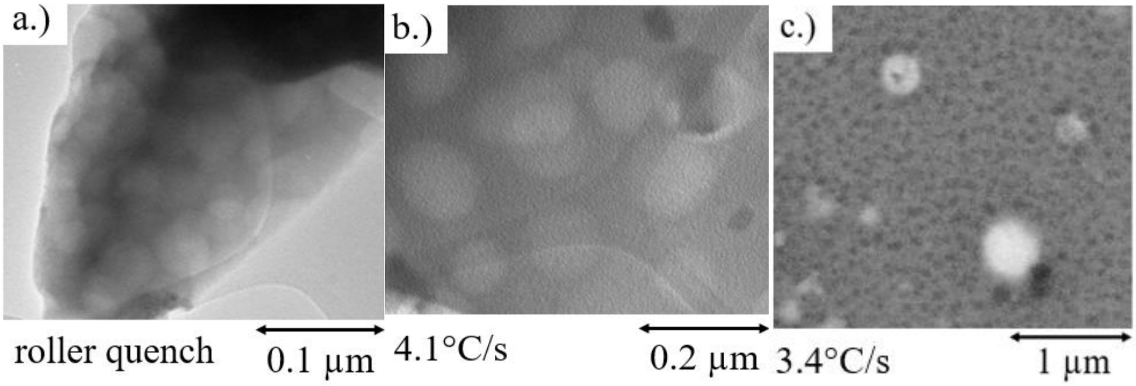

Figure 17. Electron micrographs of the PNNL glass after different continuous cooling experiments. a) TEM micrograph of the roller quench. b) TEM micrograph of sample cooled at 4.1°C/s. c) SEM micrograph of sample cooled at 3.4°C/s.

Figure 18 shows scanning electron micrographs from samples held isothermally at 900°C for 0.5 minutes (a) and 2 minutes (b). The former image shows Mo-rich droplets (arrows) embedded in the phase-separated residual glass matrix, similar to what was found for samples from the continuous-cooling experiments. After two minutes at 900°C, crystalline oxyapatite is evident and confirmed by XRD (Figure 14). It is noteworthy that in regions where the oxyapatite crystals have formed, the residual glassy phase appears to be much more homogeneous than the phase-separated morphology that is evident in regions where the oxyapatite crystals have not yet formed. Figure 18c and d are SEM images from samples held for 0.5 min at 1000°C and 800°C, respectively, clearly showing that the size of the phase seperated droplets is much smaller, if existant at all, in these samples.

EDS analysis of the TEM sample in Figure 17b indicates that the droplets are relatively rich in Al and Si, whereas the matrix phase is enriched with Ca, Zr, Mo, Cs, Ba, and the rare earth elements (Table 4). B and Li could not be detected by this EDS system and Sr and Rb had overlapping peaks but, Crum et al. [12] have shown that these elements are also concentrated in the matrix region of the phase separated glass. Crum et al. also found Cs to be more concentrated in the droplet phase. The growth of the oxyapatite crystals alters the composition of the surrounding glass by sequestering ions like Ca and the rare earths, and this appears to allow the remaining borosilicate liquid to form a more homogeneous glass upon quenching.

Figure 19 shows that the average droplet size in the phase-separated residual glass increased from ~30 nm to about ~150 nm with decreasing quench rate (~300°C/s to 4.1°C/s), but then decreased for quench rates slower than ~4°C/s. No droplets could be detected in samples cooled 0.1°C/s and slower using SEM. Also shown is the droplet size (0.14 ± 0.05 µm) found in the as-received glass near the surface (~1 mm) that was in contact with air upon being plate quenched. The residual glass in samples cooled at the slowest rates appears to be homogeneous. This change in glass morphology is believed to be associated with the growth of the oxyapatite crystals. Crum et al. [12] reports similar morphological changes in the residual glass and suggested that when oxyapatite crystallize from the lanthanide, alkaline-earth-silicate matrix, the Cs-alumino-borosilicate droplet phase dissolves into the matrix to form a homogeneous liquid that quenches into a homogeneous glass.

3.4.2. Oxyapatite Morphology and Composition. The morphology of the oxyapatite crystals depends on thermal history. No oxyapatite crystals formed in wedge-mold samples cooled faster than 4.1°C/s (step one, steel wedge), nor in isothermal samples held at 600°C, or for short times (<1-2 minutes) at higher temperatures.

There does not appear to be differences in the peak positions from the XRD patterns, Figure 11, and 15, that are assigned to oxyapatite. These peaks are assigned to oxyapatite with an expected stoichiometry of $Ca_{1.1}Nd_{3.9}Si_3O_{12.95}$ that belongs to the hexagonal crystal system and P63/m space group (#176).

The SEM images and optical micrographs in Figure 20 show representative oxyapatite morphologies for a select number of the heat treatment conditions. For example, at 700°C, oxyapatite forms very small, <1 µm, crystals that cluster in dendritic formations (Figure 20a). At 900°C, oxyapatite forms the hollow hexagonal particles shown in Figure 20b, that over time form larger, seemingly solid hexagonal crystals, Figure 20c. The crystals are also more dispersed, more defined, and less dendritic at higher temperatures, as shown Figure 20d, e, and f. Crum et al. described this hollow hexagonal form as a Hopper morphology and found that over time, the crystals grow inward [14]. At 1100°C, the hollow hexagonal oxyapatite crystals appear to be, in some cases, an order of magnitude larger than the crystals that form at 1000°C, Figure 20d.

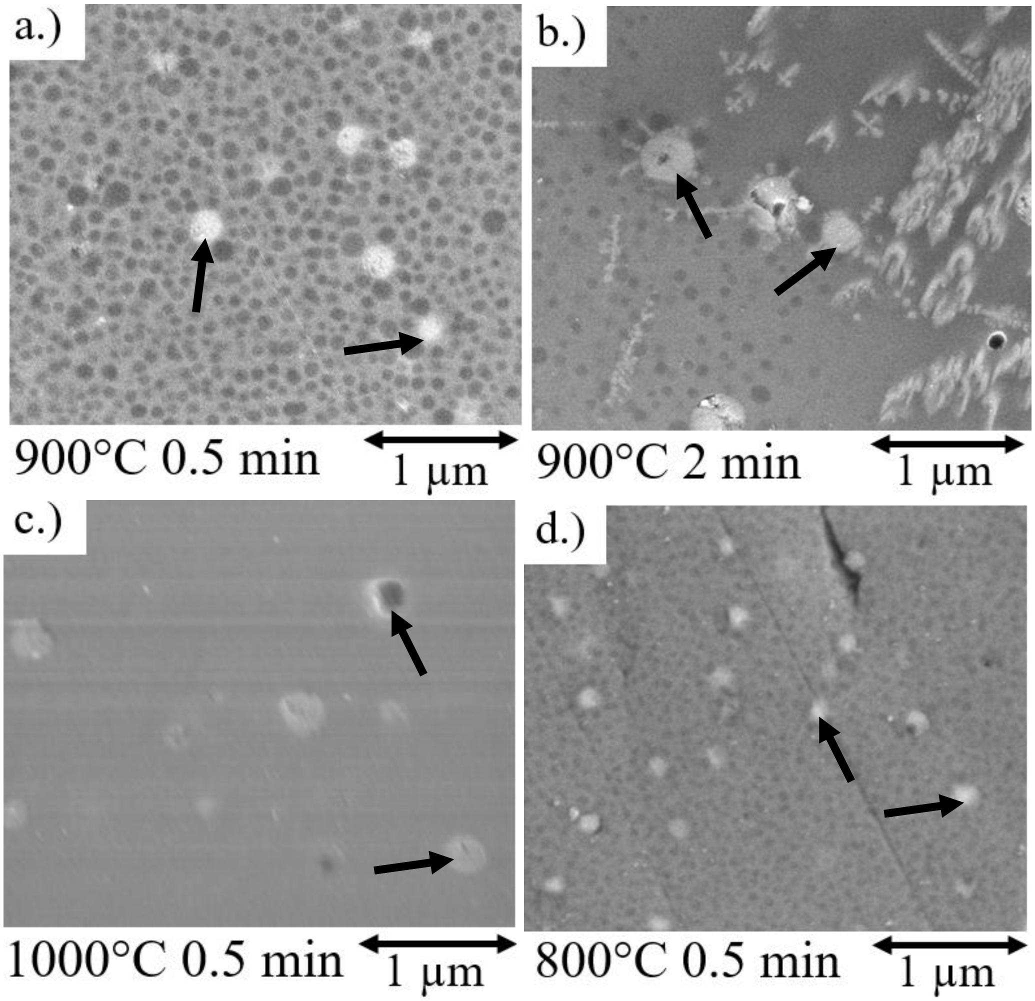

Figure 18. SEM micrographs of the a) 900°C isothermal sample after 0.5 min, b) 900°C isothermal sample after 2 min, c) 1000°C isothermal sample after 0.5 min, and d) 900°C isothermal sample after 0.5 min. Arrows show some of the Mo-rich droplets that have formed in these samples.

Table 4. Compositions of the different phases in the phase-seperated residual glass of the 4.1°C/s sample, determined by TEM EDS with oxygen normalized to 0.

Element	**Droplet [at. %]**	**Matrix [at. %]**
Na	1	2 ± 1
Al	15 ± 3	3 ± 2
Si	70 ± 9	42 ± 18
Ca	1	8 ± 4
Y	1 ± 1	2 ± 1
Zr	4 ± 2	5 ± 2
Mo	1 ± 1	5 ± 2
Ru	-	-
Rh	-	-
Te	1 ± 1	2 ± 2
Cs	1 ± 1	1 ± 1
Ba	-	3 ± 2
La	1 ± 1	3 ± 2
Ce	2 ± 1	6 ± 3
Pr	-	4 ± 2
Nd	2 ± 2	10 ± 5
Sm	1 ± 1	3 ± 2

The morphology of the oxyapatite crystals that formed in the continuous cooling samples were consistent with the morphologies of the crystals in the isothermal samples. The samples cooled at 3.4°C/s had dispersed oxyapatite crystals (Figure 20g) that were similar in size and morphology to samples held isothermally at 900°C or 1000°C for short (≤ 2 min) times (Figure 20b, d). The samples cooled at 0.1°C/s developed uniformly dispersed collections of crystals (Figure 20h), which grew to larger sizes in the sample cooled under the CCC-conditions (Figure 20i).

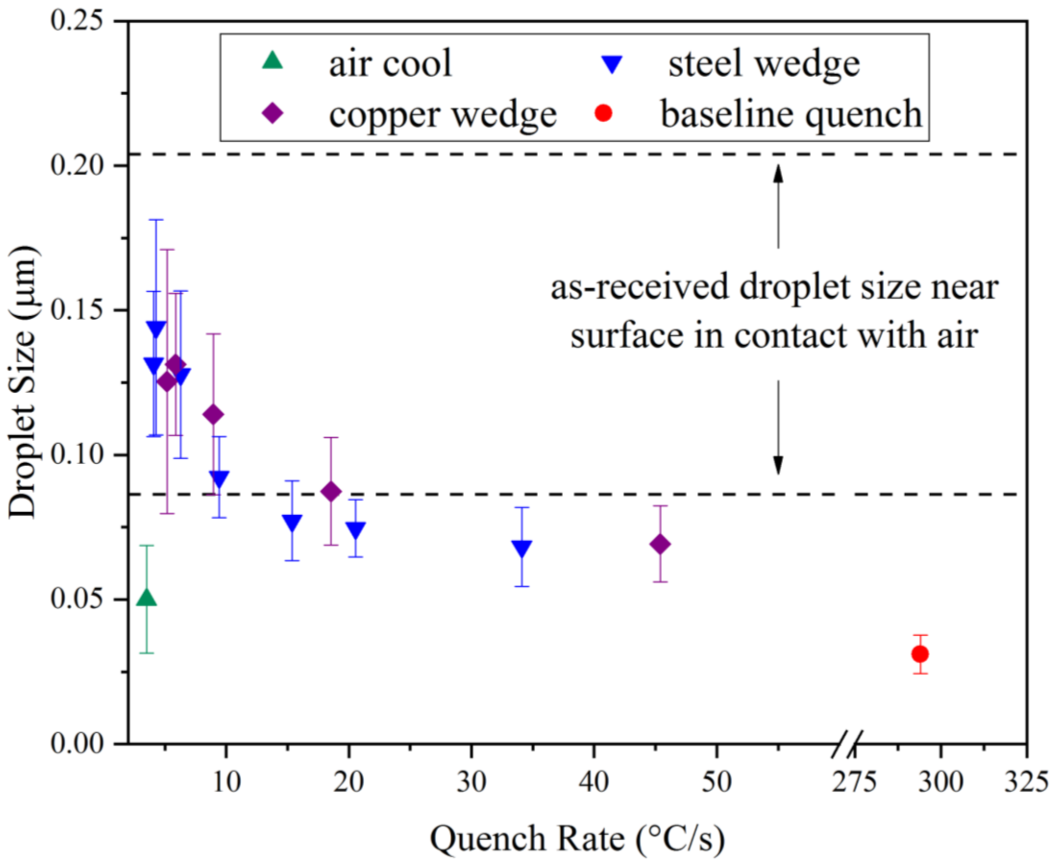

Figure 19. Size of phase-separated droplets in the PNNL glass quenched at different rates.

The fractions of oxyapatite crystals in the isothermal samples were determined from the quantitative XRD measurements and this information is summarized in the time-temperature-transformation diagram in Figure 21. Heat treatment conditions where oxyapatite was not detected are represented by the unfilled squares, and the black lines represent the conditions where the indicated fractions of oxyapatite were detected. The maximum fraction of oxyapatite (28.5 wt.%) was found in the sample held at 900°C for 24 hours. The solid blue lines represent the continuous cooling curves for several samples. It is interesting that the amount of oxyapatite was lower in the 0.008°C/s (15.2 wt.%) than the 0.1°C/s (21.4 wt.%). Asmussen et al. reported samples with similar compositions cooled along the CCC profile to contain 18.6 wt.% oxyapatite [16]. The 3.4°C/s sample does not appear to cross the region where oxyapatite formed in the isothermal experiments, however the CCT curves are shifted to longer times and lower temperatures when compared to TTT curves.

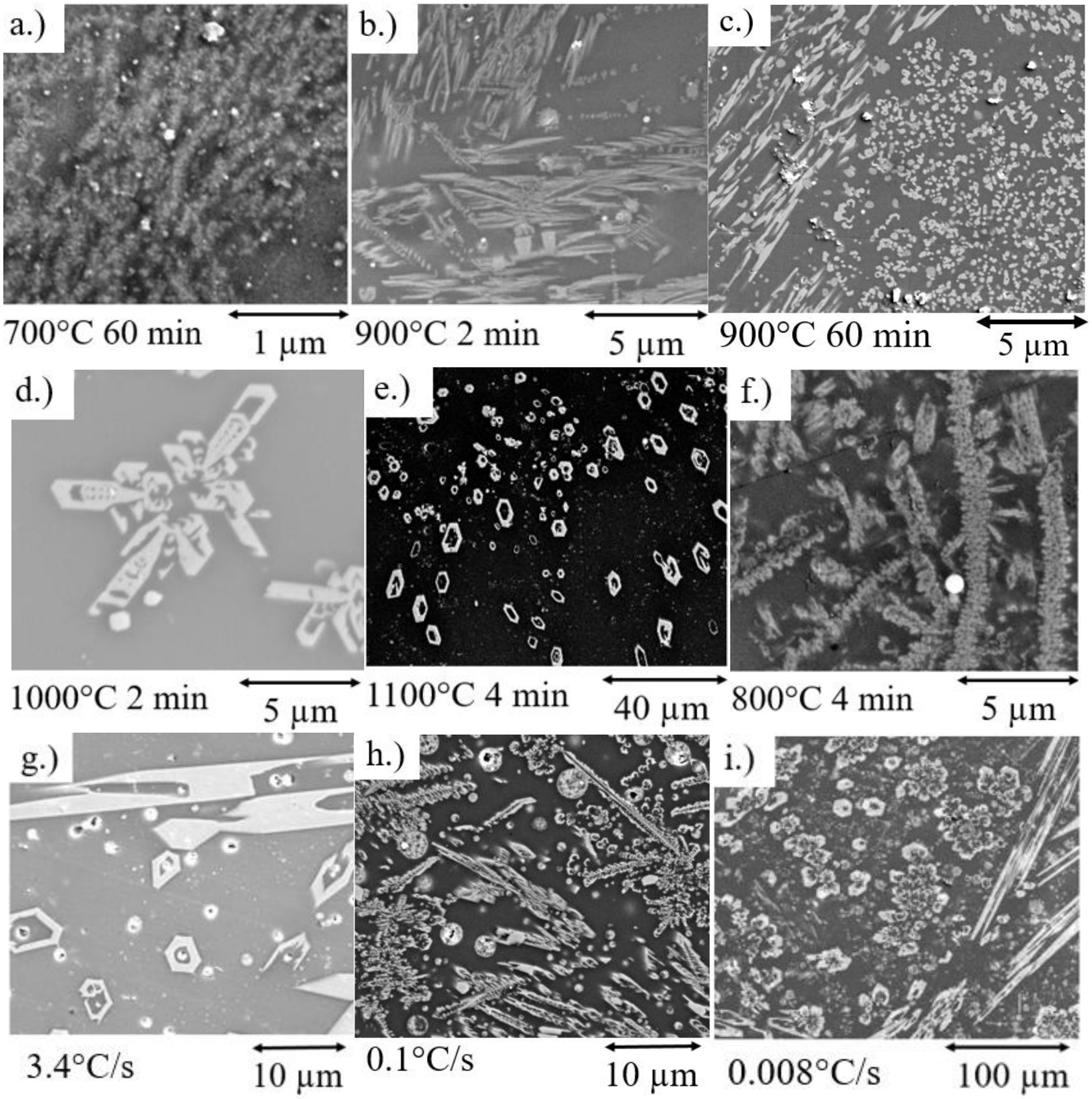

Figure 20. SEM micrograph of oxyapatite in samples heat treated at a) 1100°C for 4 min, b) 1000°C for 2 min, c) 900°C for 2 min, d) 800°C for 4 min, e) 700°C for 60 min, f) 900°C for 60 min, g) 3.4°C/s, h) 0.1°C/s and i) 0.008°C/s.

In some instances, the oxyapatite crystals were found to grow outward from a single point. For example, Figure 22 shows crystals that have grown from an area with a group of RuO_2 crystals. This might explain the differences in morphologies of oxyapatite across a sample. Shown in Figure 20c, the oxyapatite in the left side of the image are found elongated in similar directions verse the oxyapatite on the right which are mostly equal in all directions. Chouard et. al found that RuO_2 crystals act as nucleating agents for the oxyapatite crystals [21].

The compositions of oxyapatite crystals formed in a variety of samples were determined using SEM EDS and are summarized in Table 5. The major components of these crystals include Si, Ca, and the lanthanide elements, mainly Nd and Ce. The compositions do not appear to differ significantly in samples with different thermal histories and morphologies. The composition of oxyapatite crystals described by Crum et al. is also listed in Table 5 [13]. The lanthanide (LN) to silicon and Ca/Si ratio for each heat treatment are similar. The measured LN/Si ratio of oxyapatite is slightly greater and the Ca/Si ratio is slightly lower than the expected ratio ($Ca_{1.1}Nd_{3.9}Si_3O_{19.95}$) determined from XRD pattern assignments.

3.4.3. Oxyapatite Crystallization Kinetics. Kinetic information for formation of oxyapatite was obtained from the quantitative XRD data on samples collected from the tin bath isothermal experiments. Crystal fractions were normalized by dividing the weight fraction of oxyapatite for an isothermal sample by the weight fraction of oxyapatite in a sample crystallized by holding it at 900°C for 24 hours, conditions believed to produce the maximum fraction of oxyapatite (ω_{max}). Normalized weight fractions ($\alpha = \omega(t) / \omega_{max}$) are plotted vs time for each temperature in Figure 23. Some samples were run multiple times to determine experimental variability, as represented by the relevant error bars. The fastest oxyapatite crystallization rate was determined to be ~1000°C, and rates decreased at 1100°C.

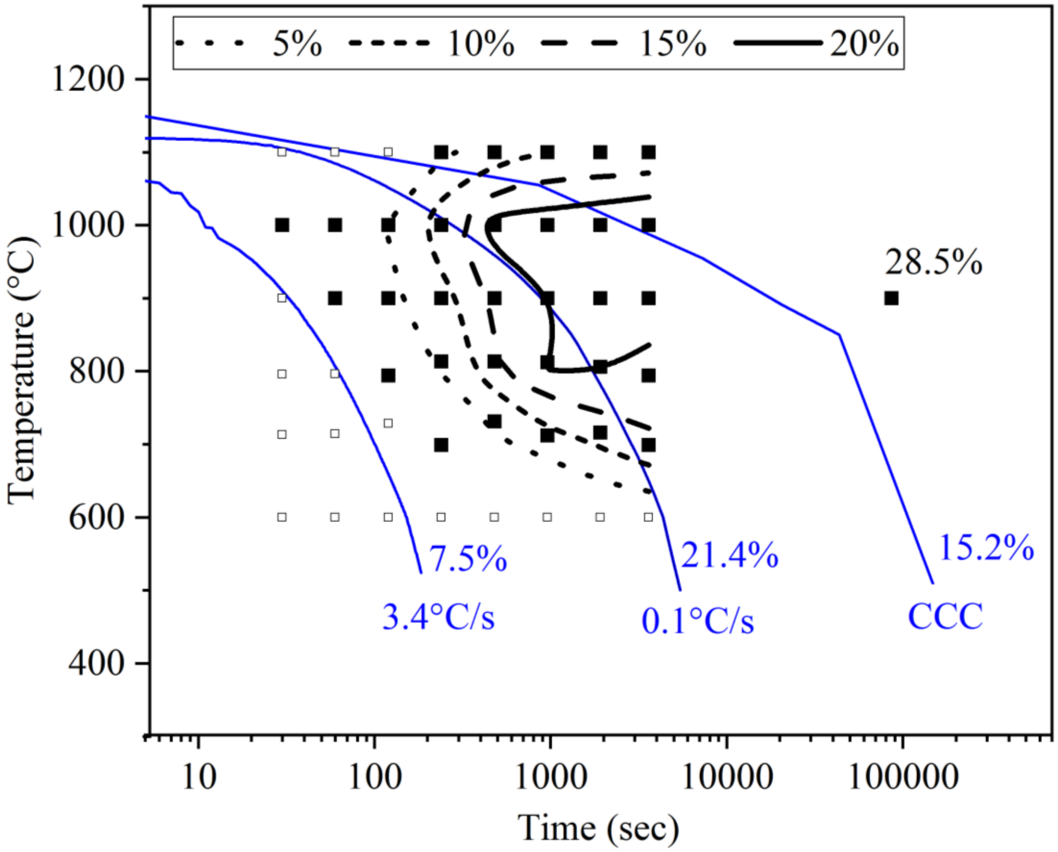

Figure 21. TTT and CCT diagrams for oxyapatite formation.

The Johnson–Mehl–Avrami–Kolmogorov (JMAK) model was used to analyze the crystal growth kinetics [22, 23]. The classic JMAK equation is

$$\alpha_n(t) = 1 - e^{[-(k_n t)^n]} \quad (1)$$

where t is time, n relates to the different nucleation and growth mechanisms, and k_n is the dissolution constant [22]. k_n is related to temperature through the Arrhenius equation,

$$k_n = k_o e^{\frac{-E}{RT}} \tag{2}$$

where k_o is a frequency factor, E is the activation energy, R is the gas constant, and T is the absolute temperature. Equation (1) can be rewritten as

$$\ln[-\ln(\alpha_n(t))] = n\ln(k_n) + n\ln(t) \tag{3}$$

where the term $n\ln(k_n)$ is the intercept and n (Avrami exponent) is the slope of a double logarithmic $-\ln(1-\alpha_n(t))$ versus t plot. Figure 24 shows the Avrami plots for oxyapatite formation between 700°C and 1000°C

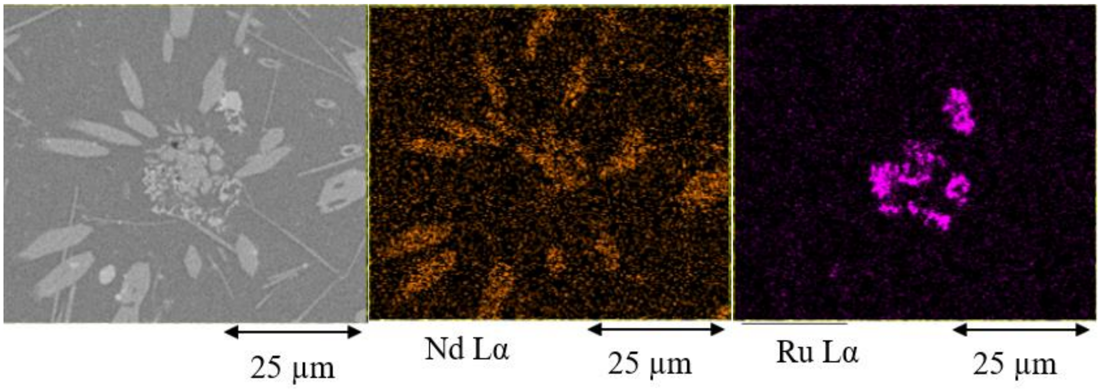

Figure 22. SEM micrograph and EDS maps showing the outward growth of oxyapatite from a RuO_2 crystal cluster in the sample heat treated at 1100°C for 32 minutes.

Equation (2) can be rewritten as

$$\ln(k_n) = \ln(k_o) - \frac{E}{RT} \tag{4}$$

where – E/R is the slope of the $\ln(k_n)$ vs 1/T plot. The $\ln(k_n)$ values extracted from the slopes and intercepts from Figure 24 are plotted vs. 1000/T in Figure 25. A slope of -7.1 ± 1.0 was determined and this corresponds to an activation energy of 58.8 ± 8.16 kJ/mol.

The Avrami exponent (n), the slopes of the Avrami plot (Figure 24), was calculated to be 0.9 ± 0.2 and this relates to the growth mechanism.

Table 5. Cation fractions in oxyapatite crystals in samples with different heat treatments with oxygen normalized to 0, compared with those reported by Crum et al. [13].

	3.5°C/s [At.%]	**CCC** [At.%]	**1100°C 60 min** [At.%]	**Crum et al. [13]** [At.%]
Na	-	-	-	2 ± 3
Al	3 ± 1	-	1 ± 1	
Si	36 ± 5	37 ± 1	37 ± 1	39 ± 4
Ca	18 ± 2	15 ± 2	14 ± 2	18 ± 2
Rb	3 ± 3	1 ± 1	-	-
Sr	1 ± 1	1 ± 1	2 ± 2	1 ± 1
Y	1 ± 1	2	2 ± 3	2
Zr	1 ± 1	-	-	NR*
Mo	-	-	-	0
Ru	-	-	-	NR*
Rh	-	-	-	NR*
Te	-	-	-	NR*
Cs	1	1	1 ± 1	0
Ba	2 ± 1	-	2 ± 1	NR*
La	4 ± 2	4	5 ± 1	4 ± 2
Ce	9 ± 2	11 ± 1	9	11 ± 4
Pr	3 ± 2	6 ± 1	3	4
Nd	15 ± 2	19 ± 1	19	17 ± 7
Sm	3 ± 2	4 ± 1	3 ± 1	2
LN/Si	1.0 ± 0.2	1.2 ± 0.1	1.1	1.0 ± 0.4
Ca/Si	0.5 ± 0.1	0.4	0.4	0.5 ± 0.1

* NR = values not reported

Fournier et al., described JMAK studies of the growth of rare earth oxyapatite crystals ($Ca_2RE_8Si_6O_{26}$) in borosilicate glasses and reported similar n values, 0.65 [24] and 0.84 [25] which they related to diffusion-controlled crystallization mechanisms. However, they also reported much greater activation energies 475 ± 90 kJ/mol [24] and 496 ± 46 kJ/mol [25] for crystal growth. A greater activation energy means there is a much greater increase in crystal growth rates with increasing temperature. Fournier et al. used less complex glass compositions in their studies while our studies have found a change in the residual glass with temperature prior to the crystallization of oxyapatite, Figure 17a, c, and d. This change in the residual glass could influence diffusion properties effecting the crystallization of oxyapatite causing a reduction in the activation energy. Crum found that residual glass phase separation affected the melt rheology increasing viscosity [14].

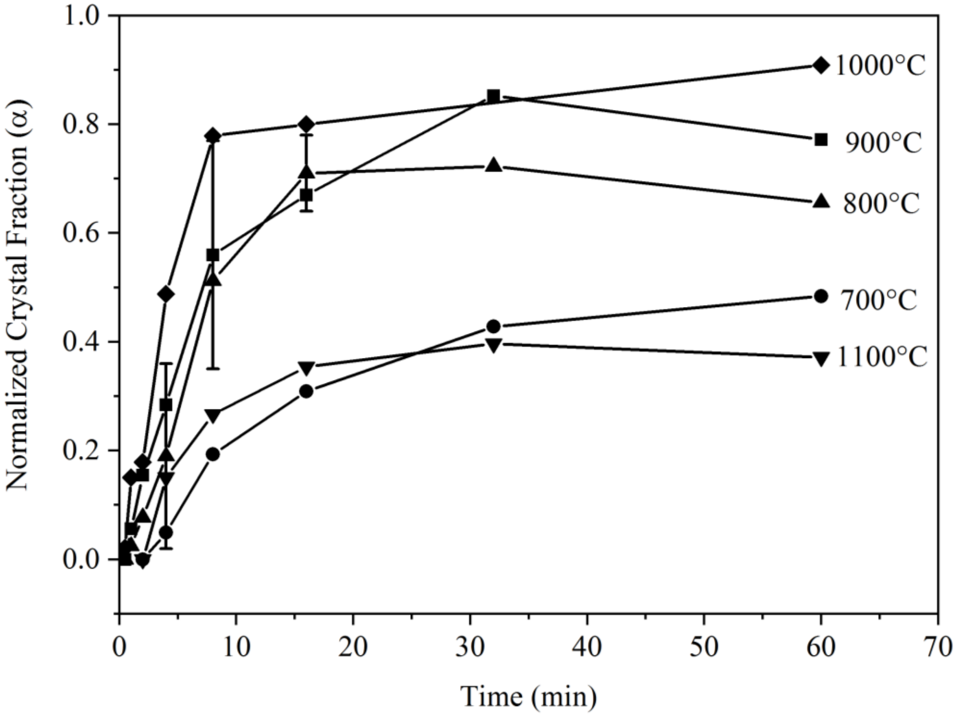

Figure 23. Crystal fraction of oxyapatite vs time for samples from the isothermal experiments.

3.4.4. Mo-rich Phase Morphology and Composition. The formation of Mo-rich crystalline phases appears to be much more complex than the formation of crystalline oxyapatite. From x-ray diffraction, Section 3.3.1 and 3.3.2, there are many molybdate phases assigned to the various patterns. From the continuous cooling patterns peaks are assigned with $Sr_{0.44}La_{0.39}(MoO_4)$, $CaMoO_4$, and $Ba_{0.75}Sr_{0.25}(MoO_4)$, in which all belong to the tetragonal crystal system I 4_1/a space group (#88). They also all have a 1:1 alkaline earth (AE) and lanthanide (LN) to molybdenum ratio. In the isothermal experiments preformed at 1100°C, there are assignments of a $CaSr_2MoO_6$, $Sr_{0.5}Ca_{0.5}MoO_3$, and $Nd_2Mo_6O_{21}$ belonging to different crystal systems and space groups.

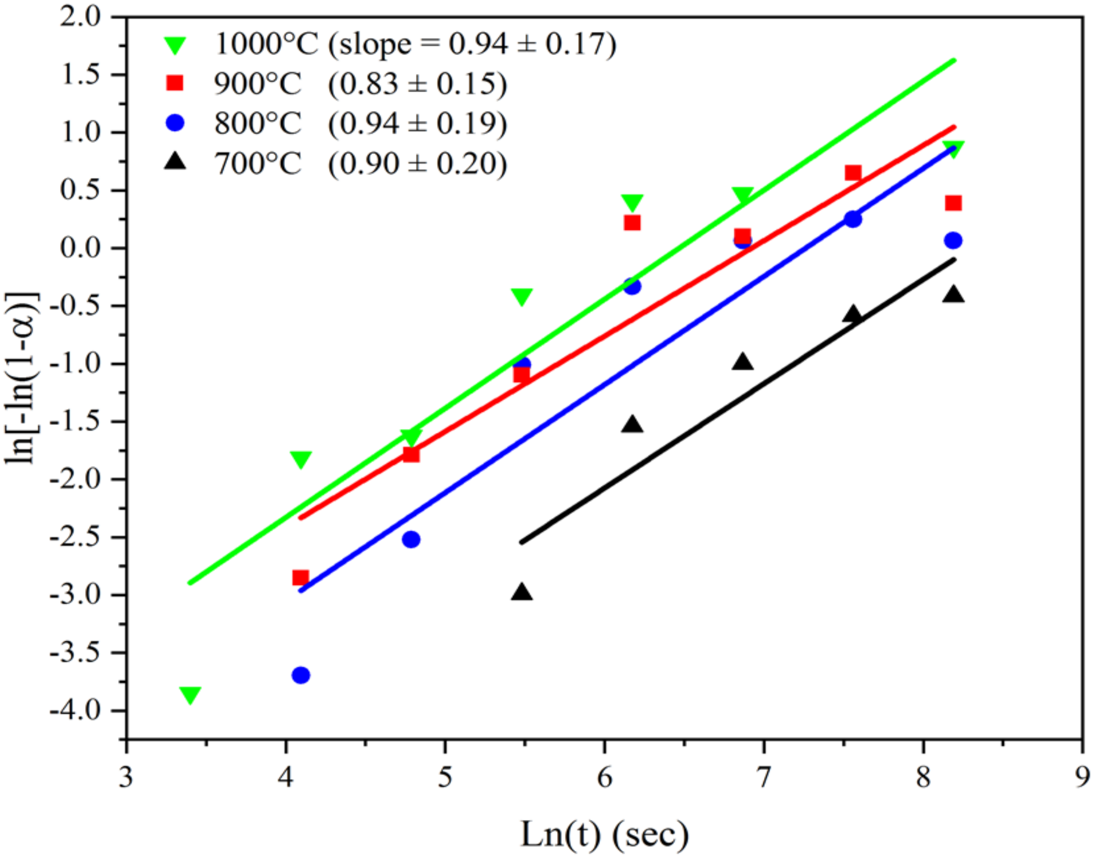

Figure 24. Avrami plot for oxyapatite isothermally held at various temperatures.

In the continuous cooling experiments, spherical morphologies were found in all samples cooled at least 0.1°C/s; viz., Figures 26a and b. In the CCC sample, the Mo-rich droplets appear to be less spherical and many have formed cross-type morphologies, as shown in Figure 26c. Mo-rich droplets were not detected by SEM in the roller quenched glass but were found in the baseline quenched glass (~300°C/s, from the isothermal study) and the droplets grow with decreasing quench rate (Figure 27). The droplet size distributions were similar for samples from both the copper wedge mold and the steel wedge mold experiments. A large increase in the size of the Mo-rich droplets occurred for the air-cooled sample (3.4°C/s), which also had oxyapatite crystals. The isothermal experiments showed that oxyapatite would crystallize before crystalline powellite could be detected using XRD; e.g., Figure 15. The rapid growth of the Mo-rich phase after the precipitation of the lanthanum silicate oxyapatite phase indicates that the lanthanide ions influence the solubility of Mo in the glass melt. This is discussed in more detail in Section 3.6.

The Mo-rich droplets in the as-received glass sample were found to be 0.24 ± 0.05 µm represented with the dashed horizontal lines shown in Figure 27. If these droplet sizes are an indication for the quench rate of a sample, then the estimated quench rate of the as received glasses likely falls in the range 10-25°C/s.

The isothermal experiments reveal that the morphology of the Mo-rich phases changes significantly with time and temperature. Figure 28 shows examples of Mo-rich phases with spherical, dendritic, cross-like, and needle-like morphologies, with the latter being more abundant at higher temperatures and longer times. The dendritic structures appear to grow between the aluminosilicate-rich droplets in the phase separated residual glass and, in many cases, the dendrites grow from the spherical droplets, as shown in Figure 28a. The Mo-rich crosses appear to form in the more homogenous residual glass and are not associated with other microstructural features; viz., Figure 28a. These cross-like structures are described by Delattre et al. [26] and Li et al. [27] as possessing perpendicular arms of equal length. At 1100°C, where slow nucleation rates and fast crystal growth rates are expected, needles with lengths many orders of magnitude larger than the crosses and dendrites are the dominant Mo-rich phase (Figure 28b and c). Many powellite needles are oriented in similar directions or from similar points.

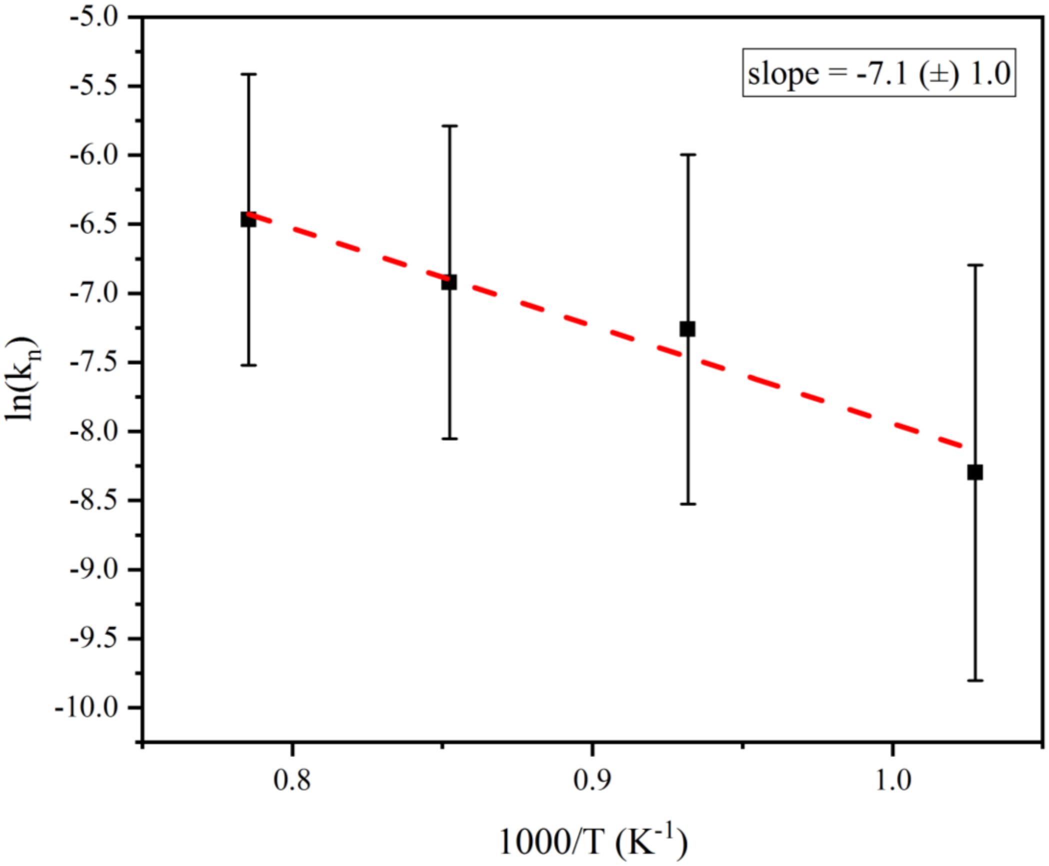

Figure 25. $\ln(k_n)$ vs 1000/T for oxyapatite growth from isothermal hold experiments between 700 and 1000°C.

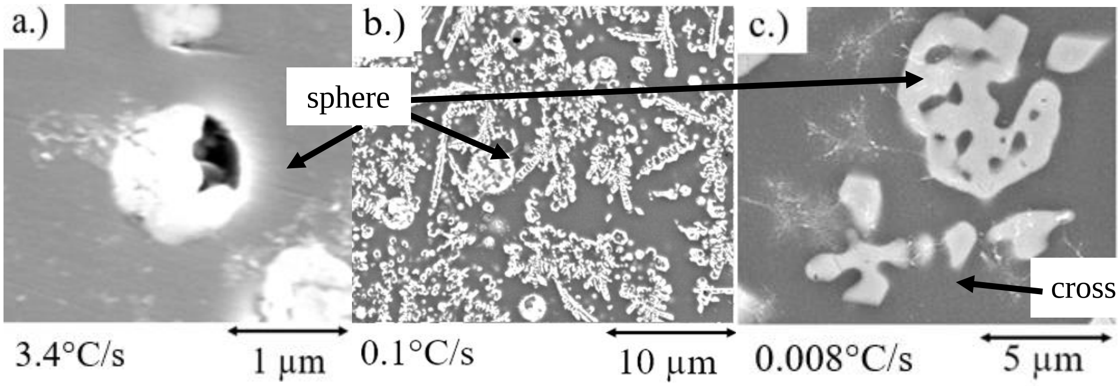

Figure 26. SEM images of powellite in samples continuously cooled a) 3.4°C/s, b) 0.1°C/s, and c) 0.008°C/s.

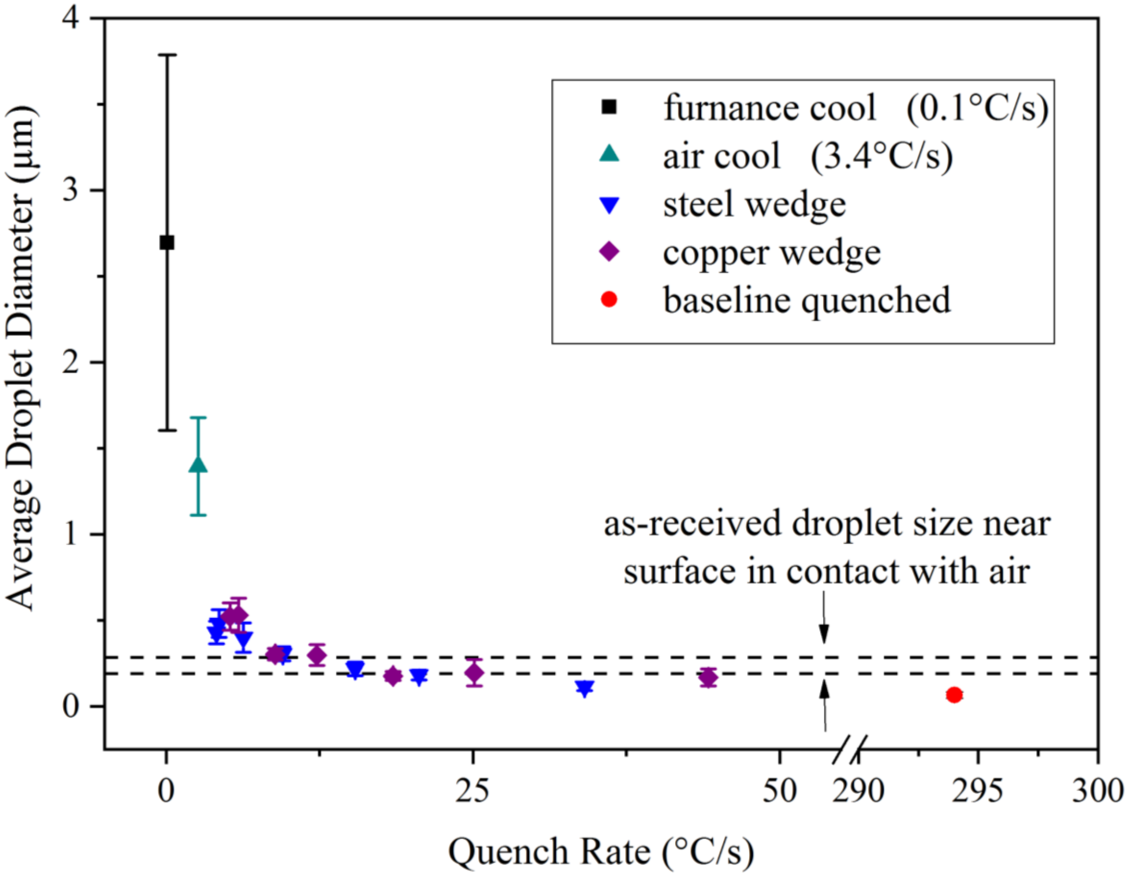

Figure 27. Molybdenum droplet diameter vs quench rate for samples from the continuous cooling experiments. The horizontal dashed lines represent the average diameter with one standard deviation of droplets from the as-received glass 1 mm from the surface that was in contact with air.

The average compositions of different Mo-rich phases were determined using SEM EDS and TEM EDS and are summarized in Table 6. The spherical morphologies in samples prepared using quench rates faster than the CCC treatment separated into Ba-rich and Ca-rich molybdate crystals, as shown in Figure 13. Crum et al. found that the spherical molybdate particles separated into spherical clusters of small $BaMoO_4$ and $CaMoO_4$ crystals [12]. Later studies found these crystals to be based on two types of solid solutions, $Ca_xSr_{1-x}MoO_4$ and $Ca_xBa_{1-x}MoO_4$ [13, 16]. Crum et al. found similar compositions for these phases in samples with the same composition [13]. In the CCC sample, Ca/Sr-molybdate particles were found but no Ba/Sr-molybdate particles. The cross-like molybdates have similar compositions to the spheres, but the needles have significantly greater lanthanide concentrations, as discussed earlier with Figure 16. The alkaline earth (AE) and lanthanide (LN) to molybdenum concentrations are also listed in Table 6 and have a 1:1 ratio comparable to the expected ratios from the XRD pattern assignments.

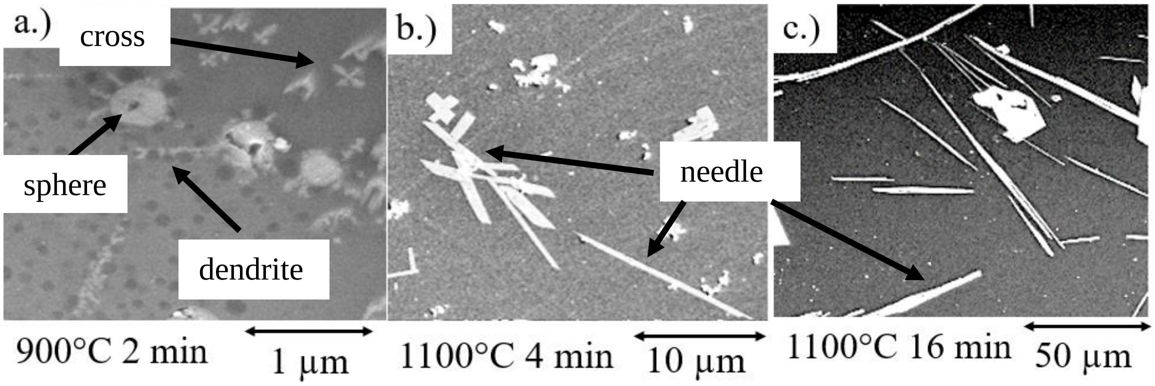

Figure 28. SEM images of Mo-rich phases in samples heat treated isothermally a) 900°C for 2 min, b) 1100°C for 4 min, c) 1100°C for 16 min.

A TTT/CCT diagram for the formation of the molybdate phases is shown in Figure 29. At low temperatures, <900°C, molybdates are only found as spheres. These spheres form before the crystallization of oxyapatite and this is discussed later in Section 3.6. At temperatures in the range from 900°C to 1000°C, Mo-rich phases with spherical, dendritic, cross-like, and needle-like morphologies have been found, whereas at 1100°C, the molybdate phases were found to have spherical and needle morphologies.

The results of the continuous cooling experiments align with those from the isothermal experiments. In the samples cooled at 3.4°C/s and 0.1°C/s, spherical powellite particles were found with sizes and compositions similar to those found in isothermal samples held at ≤ 900°C. No needles, dendrites, or crosses were found in the 3.4°C/s and 0.1°C/s samples because they were cooled quickly through the temperature ranges where those morphologies developed in the isothermal samples (Figure 29). In the sample cooled according to the CCC profile (0.008°C/s), cross-type powellite was the dominant phase, with some droplets. This is consistent with the longer times spent at temperatures where cross-type powellite was found to form in the isothermal experiments. The variations in the compositions and morphologies of the Mo-rich phases with temperature invalidated the use of the JMAK kinetic analysis, as discussed in Appendix A.

Raman spectroscopy was useful to differentiate the various Mo-rich phases and confirmed that the needles have different structures and compositions than the spheres and crosses. Figure 30 shows representative Raman spectra of the various morphological features found in these samples. Figure 31 shows optical micrographs the features from where the Raman spectra were collected. The peaks in the residual glass spectrum correlate to a symmetric internal $[MoO_4]^{-2}$ tetrahedral Mo-O stretching mode (910 cm^{-1}) [28, 29]

and another internal $[MoO_4]^{-2}$ tetrahedral O-Mo-O bending mode (320 cm^{-1}) [29, 30]. The peaks from spectra of the oxyapatite crystals correlate to $[SiO_4]^{-4}$ tetrahedral stretching (860 cm^{-1}) and bending modes (529 cm^{-1} and 400 cm^{-1}), as well as a La-O stretching mode (298 cm^{-1}) [31]. The spectra from the cross and droplet features contain peaks assigned to internal $[MoO_4]^{-2}$ tetrahedral vibrational modes (324, 385, 795, 843, and 880 cm^{-1}) and external (vibrations between the lattices) $[MoO_4]^{-2}$ tetrahedral rotational modes (197 cm^{-1}) [32]. The spectra collected from the Mo-rich needles are very different and have not yet been identified.

3.5. TIME-TEMPERATURE-TRANSFORMATION DIAGRAM

A Time-Temperature-Transformation, TTT, diagram that summarizes the overall crystallization of the borosilicate waste glass was developed using the information from the isothermal tin bath experiments and is shown in Figure 32. Scanning electron microscopy identified the morphologies of the phases present in each sample, which are indicated by the different symbols. Quantitative XRD only detected and identified two phases, oxyapatite, represented by the large symbols, and powellite, represented by large closed symbols. The quantitative XRD information was used to develop the lines that represent the overall crystallization fractions (5, 10, 20, and 25 wt. %), determined by linear interpolation of two neighboring measured data points and these are also plotted in Figure 32.

Mo-rich spheres were detected by SEM in all samples. The phases that form after short times are x-ray amorphous, but TEM determined that these spheres were indeed crystalline and possessed similar compositions to the crystalline powellite detected by

XRD in samples heated for longer times. Raman spectroscopy also found very similar vibrational modes for all Mo-rich spheres. The dendritic and cross molybdate phases were also found to be very similar to the spheres and all are believed to be the powellite phase detected by XRD.

Table 6. Cation fractions of Mo-rich crystals in samples with different heat treatments with oxygen normalized to 0, compared with those reported by Crum et al. [13].

Element	**4.1°C/s (Ba,Sr,Mo)**	**4.1°C/s (Ca,Sr,Mo)**	**CCC (cross)**	**CCC (droplet)**	**1100°C 60 min (needle)**	**Crum et al. [13]**
	TEM [At.%]	TEM [At.%]	SEM [At.%]	SEM [At.%]	SEM [At.%]	SEM [At.%]
Na	10 ± 2	6 ± 1	4 ± 1	3 ± 1	1 ± 1	3 ± 4
Al	4 ± 1	-	1 ± 1	2 ± 1	1 ± 1	-
Si	-	13 ± 2	5 ± 4	8 ± 5	31 ± 7	-
Ca	20 ± 2	27 ± 3	26 ± 5	27 ± 2	8 ± 2	33 ± 11
Rb	-	-	-	-	-	3 ± 4
Sr	7 ± 3	5 ± 3	7	7	1	8 ± 4
Y	-	-	-	-	-	-
Zr	-	-	1 ± 1	-	3 ± 1	NR*
Mo	41 ± 8	41 ± 10	46 ± 3	46 ± 5	36 ± 11	55 ± 7
Ru	-	-	1 ± 1	-	-	NR*
Rh	-	-	-	-	-	NR*
Te	-	-	1 ± 1	1 ± 1	-	NR*
Cs	-	-	-	1 ± 1	-	-
Ba	14 ± 5	2 ± 3	1 ± 1	1	1	NR*
La	-	-	1	1 ± 1	3 ± 1	-
Ce	-	2 ± 4	1	1 ± 1	5 ± 1	-
Pr	-	-	1 ± 1	0	2 ± 1	-
Nd	3 ± 3	3 ± 4	2	2 ±1	6 ± 1	-
Sm	-	1 ± 4	1 ± 1	0	-	-
(AE+LN)/Mo	1.0	1.1	0.9 ± 0.1	0.9 ± 0.2	0.8 ± 0.4	0.7 ± 0.2

* NR = values not reported

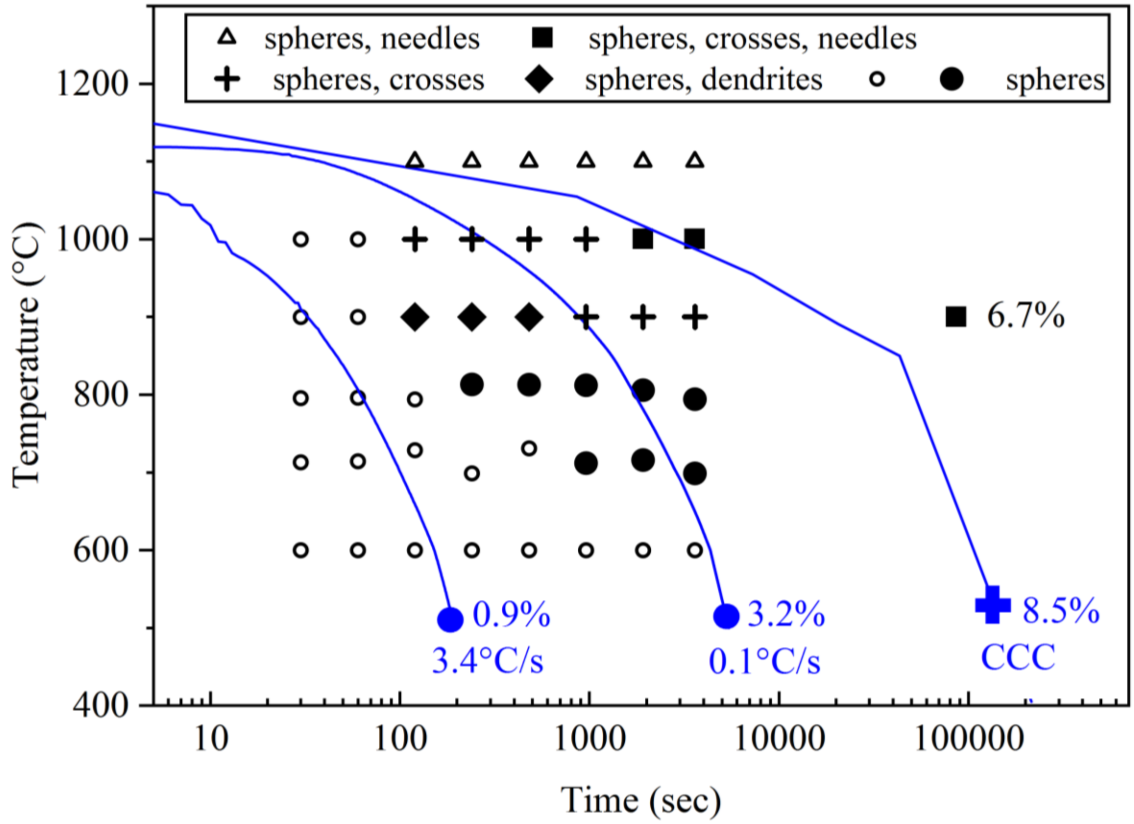

Figure 29. TTT (black symbols) and CCT (blue lines) for the formation of different Mo-rich crystals. The open symbols indicate x-ray amorphous Mo-rich phases. The morphologies were determined using SEM and the crystal fractions were determined by quantitative XRD.

Powellite was not detected in the XRD patterns of samples heated at 1100°C; these samples instead possess Mo-rich needles with large concentrations of lanthanide ions. This phase is labeled as “needles” in Figure 32 and these needles were also found using SEM and Raman spectroscopy in samples after long times at 1000°C and 900°C. SEM images of the 1100°C/2 minute sample indicated the presence of some oxyapatite crystals, even though they could not be detected by XRD; these samples are labeled “trace oxyapatite” in Figure 32. Samples held at 1100°C for short times, 0.5 and 1 min, were not recorded in this diagram because it is uncertain to whether the Mo-rich spheres that were found in the samples formed at this temperature or if they formed while the samples were quenched in water.

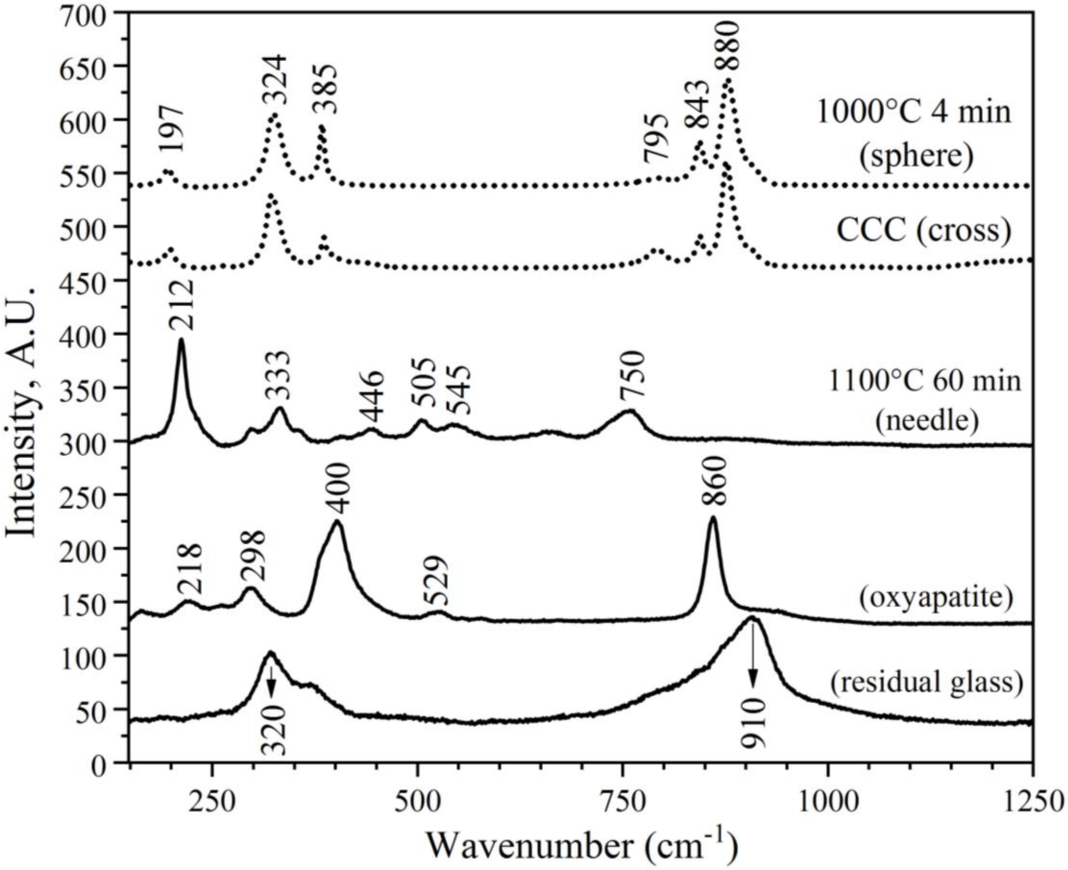

Figure 30. µ-Raman spectra of (dashed lines) a powellite sphere and cross in the sample heat treated at 1000°C for 4 min and (solid lines) spectra of a powellite needle, oxyapatite, and the residual glass in the 1100°C 60 min sample.

The first crystalline phase to be detected by XRD at every temperature was oxyapatite, with crystalline powellite detected at longer times. The weight fraction of oxyapatite was always greater than that of powellite, with the former approaching 30 wt.% of the sample, and powellite not exceeding 10 wt.%. The fastest crystallization occurs around 1000°C. The sample held at 900°C for 24 hours reached an overall crystal percentage of 35.2%, the largest fraction of any sample studied. The data from the Rietveld analyses for the crystalline percentages can be found in Table A.3 of Appendix A. Not shown in the diagram is the RuO_2 crystals that were found in every sample using SEM and are known to be insoluble in this borosilicate glass.

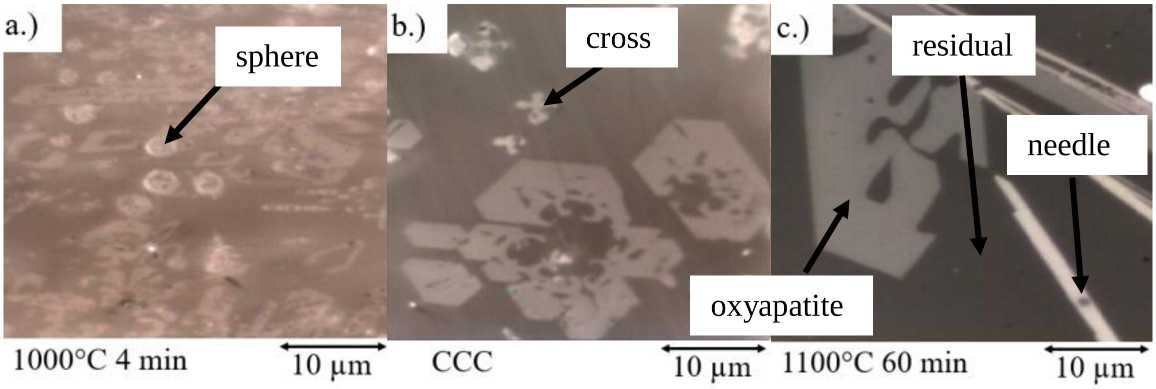

Figure 31. Micrographs showing locations of where the Raman spectra in Figure 30 was collected.

3.6. GLASS-CERAMIC FORMATION PATHWAYS

The isothermal and constant cooling rate experiments provided important information on the crystallization pathways, and the types and sizes of the phases that form are summarized in Figure 33. A transformation diagram was developed to show how these phases evolve, shown in Figure 34. It should be noted that the heavy metal (e.g., RuO_2) phase that is present in all samples and is known to be insoluble in these melts even at 1300°C [8] is not included in this analysis. The following section will describe the phase transformations as a function of the relative nucleation and crystallization rates expected at different temperatures.

At high temperatures (~1000 to 1300°C, the melting temperature (T_{melt}) used here), where there are expected to be fewer nuclei and fast crystal growth rates, a small number of oxyapatite and needle-like molybdate crystals rapidly grow in size. As indicated in Figure 34, the oxyapatite and Mo-rich needles crystallize directly from the melt around the same time. The phase assemblage of the glass heat-treated for short times is uncertain due to the fast growth of the phase separated glass and the Mo-rich spheres at ~900°C, Figure 17a. It is believed that any phase separation in the samples held for short times occurred upon quenching the glass in water instead of forming at the high temperatures. At high temperatures, >1000°C, the oxyapatite crystals are large, hexagonal-shaped crystals (colored white in Figure 33 and Figure 34) sometime with a hollow center and the molybdate phase is found as mostly long needles (colored light grey in Figure 33 and Figure 34). Often these crystals are found to grow from a central point, also displayed in Figure 33.

In the temperature range from ~800°C to ~1000°C, the nucleation and crystallization rates are likely similar and so crystallization is fastest at these temperatures. On cooling, the melt first separates into an aluminosilicate-rich droplet phase and an alkali and alkaline earth (AE)-lanthanide (LN)-Mo-rich borosilicate matrix phase, as shown in Figure 34. Mo-rich droplets that also concentrate Ca and Ba ions then grow from the AE-LN-Mo-borosilicate phase, and these crystallize to form the two phases with the powellite crystal structure, (Ca-rich)MoO_4 and (Ba-rich)MoO_4. At longer times, oxyapatite ($Ca_2LN_8Si_6O_{26}$) crystallizes from the matrix portion of the phase-separated residual glass, and this causes the droplet phase to dissolve into the modified matrix to form what appears in SEM to be a homogeneous glass. In this temperature range, oxyapatite crystallizes fast enough so that there is sufficient Mo still left in the newly homogenized residual glass that will then crystallize out as (Ca-rich)MoO_4 crosses. It appears that when Mo crystallizes out directly from a homogeneous residual glass phase, it forms crosses and needles, but if the glass has a phase separated morphology, Mo-rich spheres separate and subsequently crystallize. The needles were found to be a much different material, one containing greater concentrations of lanthanides and lower concentrations of alkaline earth, most likely due to the composition of the glass from which they crystallize. The crosses were found to be only (Ca-rich)MoO_4. The spheres were found to contain amounts of Ba unlike the crosses which crystalizes into both (Ca-rich)MoO_4 and (Ba-rich)MoO_4 with the former to be more abundant.

In the temperature range from ~600°C to ~800°C, one expects that the relative nucleation rates are much greater than the crystal growth rates, and this leads to the formation of dendritic clusters of smaller oxyapatite crystals, as represented in Figure 33. Since the glass transition temperature of this material was ~590°C, no significant phase transformations are expected below this final temperature range.

Mo is incorporated in borosilicate glasses as MoO_4^{2-} units, and Chouard et al. found that samples with increased Nd had a higher Mo solubility. He believed that lanthanide ions, like Nd^{3+}, increased molybdenum solubility through blocking the transport of the MoO_4^{2-} units through also bonding with the silica network [21]. At high temperatures this effect will be minimal due to the lower viscosity allowing the MoO_4^{2-} and Nd^{3+} units to combine with alkaline earths and precipitate molybdate and oxyapatite crystals, respectively.

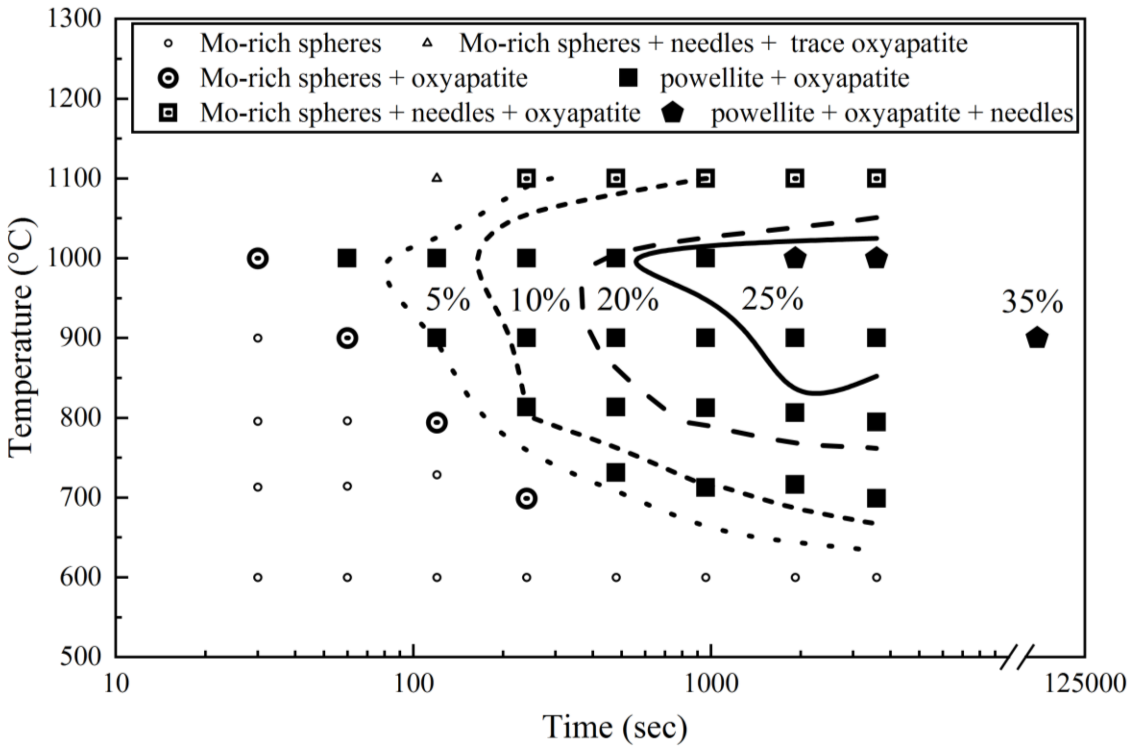

Figure 32. TTT diagram describing the fraction of crystallized material that forms in the PNNL borosilicate waste glass.

At lower temperatures, instead of the Nd^{3+} blocking the transport of the MoO_4^{2-} through the bondings with the silica network [21], the MoO_4^{2-} and Nd^{3+} ions are located in the AE-LN-Mo-rich borosilicate matrix phase. Brehault et al. [9] found this combination also increased the solubility of MoO_3. The increased local concentration of MoO_4^{2-} units is still great enough to cause some of the MoO_4^{2-} ions to precipitate out into powellite. With longer times Nd^{3+} ions precipitate into oxyapatite. The close association of powellite and oxyapatite crystal formation, both temporal and spatial, is consistent with the concentration of lanthanide ions and molybdate tetrahedra in the matrix portion of the phase separated liquid that first forms on cooling. Powellite crystals are generally found near oxyapatite crystals, and there are many examples of powellite spheres that have formed within the hollow oxyapatite hexagons; i.e., Figure 12. Also, because there's increased solubility of Mo in the AE-LN-Mo-rich borosilicate matrix phase, the precipitation of powellite crosses may be influenced by the decrease in Mo solubility with the sequestration of Nd in the oxyapatite crystals and reduction of the phase separation.

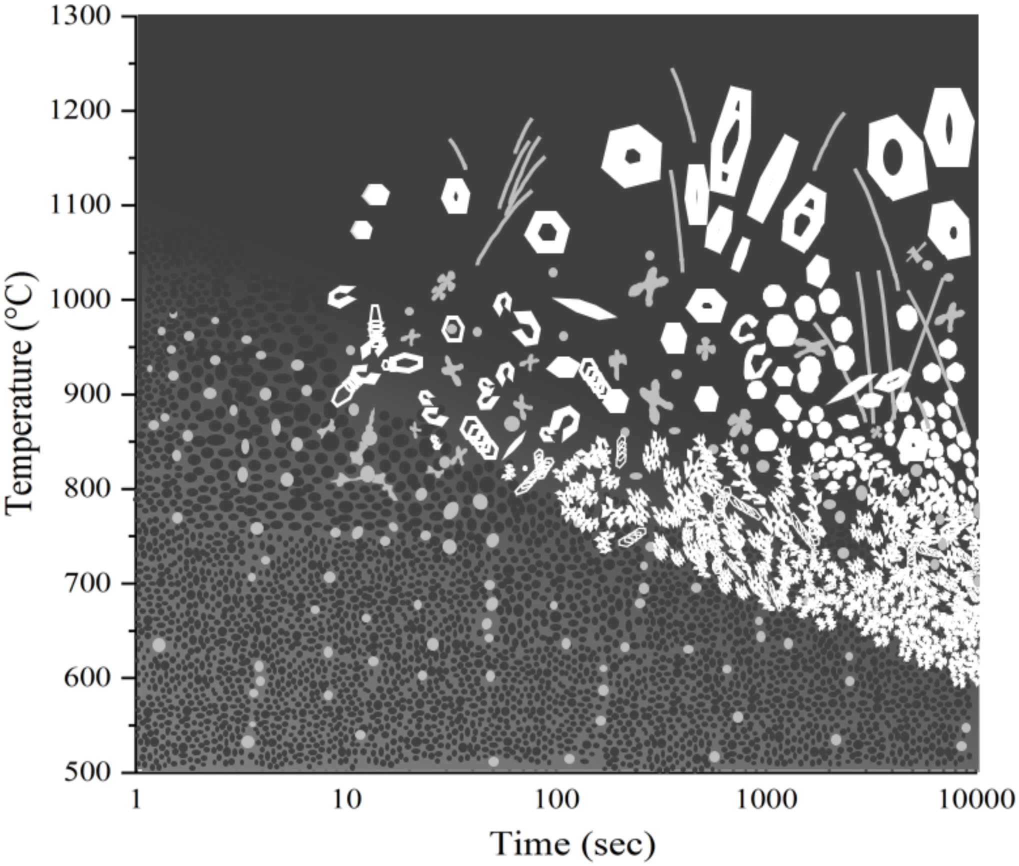

Figure 33. Schematic figure of the effects of time and temperature on the development of microstructural features in the borosilicate waste glass-ceramic. Sizes are not to scale but show general trends.

The composition of the residual glass for some continuously cooled samples was estimated by subtracting out the crystal phases from the as-received composition and are summarized in Table 7. The composition of the phases determined by EDS were normalized to their respective crystal fractions determined by quantitative XRD and subtracted from the nominal glass composition. The lanthanides and Mo decrease with decreasing cooling rate due to oxyapatite and powellite crystallizing out of the glass. B was found to only be contained in the residual glass and increased with slower cooing rates. Changes in the composition of the residual glass would have an effect on thermal and chemical durability properties to be described in future work.

The phase development pathways identified in this study are useful for explaining the microstructural development of oxyapatite reported in other studies. For example, Delattre et al. [25] found that the oxyapatite crystals that formed in a borosilicate glass after treatment times >1 hour at temperatures from 700°C -775°C were hollow hexagonal dendrites and needles, whereas solid hexagonal dendrites/needles formed at temperatures from 700°C -840°C. In the present study, hollow oxyapatite crystals formed at isothermal temperatures as high as 1100°C, and these hollow oxyapatite forms are favored at shorter times for all temperature, whereas the filled oxyapatite crystals were more common at longer times. Delattre et al. nucleated their samples for 6 hours at 630°C prior to their isothermal heat treatments, whereas in the present study, samples were isothermally heat treated immediately after melting, avoiding any prior nucleation or crystallization events. Delattre et al. did not find any hollow crystals at the higher temperatures, since at those temperatures the crystallization rate is faster, and the residual melt is less viscous, so the pre-nucleated samples would quickly transform to the filled hexagonal crystals.

The phase development pathways identified in this study also expand on results reported by Asmussen et al. [16] by providing a range of cooling rates ~4 magnitudes wider and Crum et al. [12] providing more precise times and temperatures for the phase transitions. Asmussen et al. found clusters of much smaller oxyapatite crystals formed in samples cooled four times faster than the cooling rate of the CCC sample, ~0.03°C/s, a morphology similar to what was created in the sample cooled at 0.1°C/s in this study. Crystals produced in their samples cooled ¼X the CCC sample were also much larger aligning with the large crystals found in the samples heat treated at high temperatures (>1000°C) in which this sample would spend sufficient time at those temperatures. Crum et al. [12] described similar phase transformations in which the glass would phase separate into an aluminosilicate droplet and matrix phase and from this matrix phase powellite and oxyapatite would crystallize out. The TTT and CCT diagrams developed in this study provides useful data describing times, temperatures, and cooling rates for these transformations.

4. CONCLUSIONS

Experimental protocols to quantitatively characterize the microstructural transformations that occur as functions of time and temperature for a complex borosilicate glass-ceramic designed for nuclear waste remediation have been developed. Oxyapatite, $Ca_2LN_8Si_6O_{26}$, and powellite, (Ca-rich)MoO_4, are the two major crystalline phases that form when these melts are cooled. Molybdenum and rare earth ions are concentrated in the matrix liquid which surrounds aluminosilicate rich droplets, when the melts initially phase separate on cooling. Molybdenum-rich droplets separate from the matrix to form powellite-like crystalline phases, followed by the formation of the oxyapatite crystals. The changes in the liquid composition with the precipitation of these crystals causes the residual glass microstructure to become more homogeneous upon quenching.

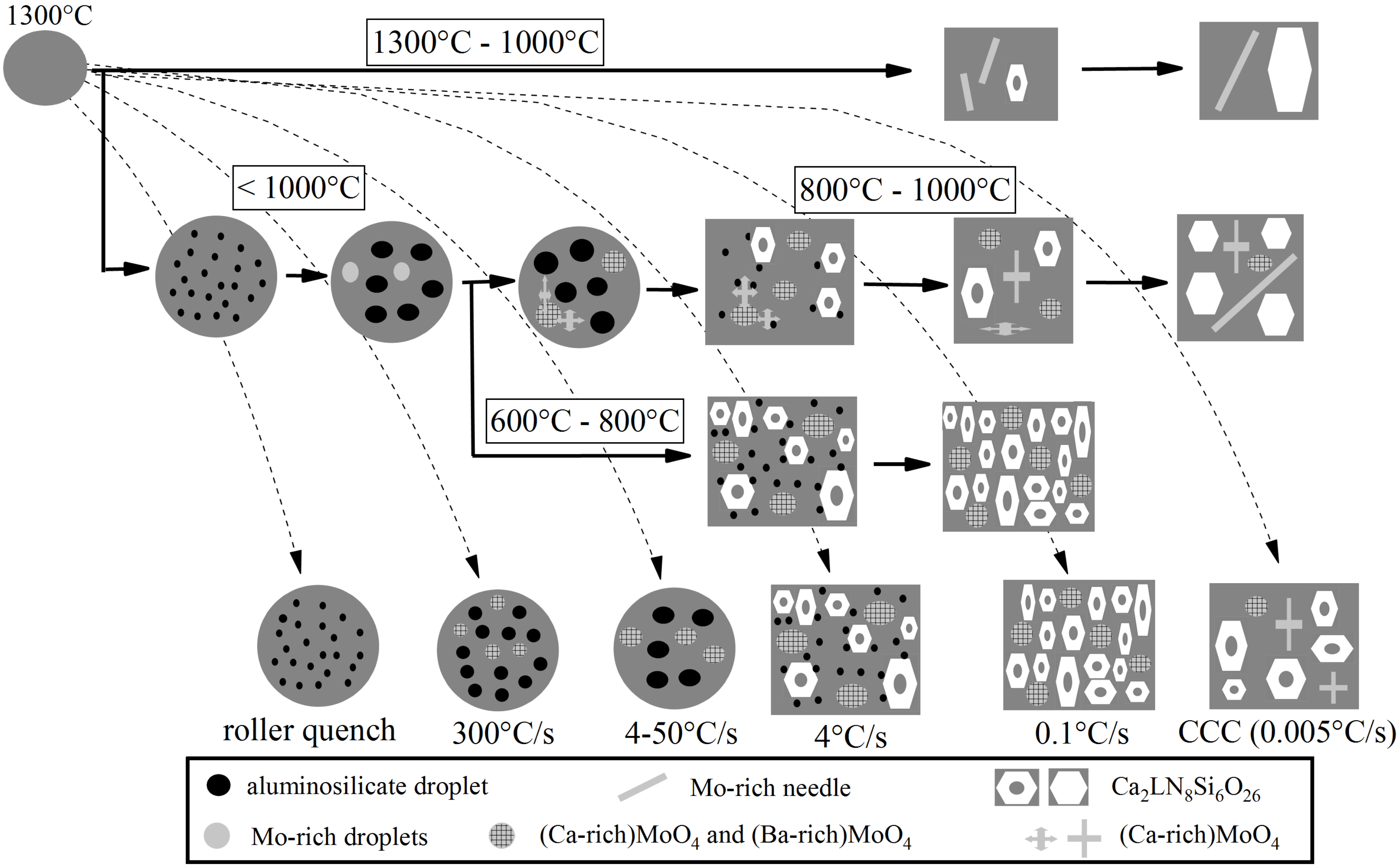

Figure 34. Phase transformation pathways of isothermal and continuous cooling experiments. Crystalline features are below the detection limit of the XRD in the circular maps.

Table 7. Estimated composition of the residual glass at various cooling rates.

Oxide	**as-received [At.%]**	**3.4°C/s [At.%]**	**0.1°C/s [At.%]**	**CCC [At.%]**
Al_2O_3	3.8	3.9 ± 0.1	3.8 ± 0.5	4.5 ± 0.2
B_2O_3	11.3	12.1 ± 0.2	14.5 ± 1.2	13.4 ± 0.5
BaO	2.2	2.2 ± 0.1	2.2 ± 0.5	2.5 ± 0.1
CaO	8.4	7.6 ± 0.3	5.7 ± 1.5	5.6 ± 0.9
Ce_2O_3	1.5	1.2 ± 0.1	1.2 ± 1.1	0.9 ± 0.2
Cs_2O	1.6	1.6	1.8 ± 0.2	1.9 ± 0.01
La_2O_3	0.8	0.64 ± 0.1	0.6 ± 0.5	0.6 ± 0.1
Li_2O	3.2	3.5	4.2 ± 0.4	3.9 ± 0.1
MoO_3	4.2	4.2 ± 0.1	3.6 ± 0.6	1.2± 0.9
Na_2O	4.1	4.3 ± 0.1	4.1 ± 1.6	4.7 ± 0.2
Nd_2O_3	2.4	2.0 ± 0.1	1.7 ± 0.5	1.3 ± 0.3
Pr_2O_3	0.7	0.6 ± 0.1	0.5 ± 0.5	0.3 ± 0.1
SiO_2	47.7	48.0 ± 1.0	47.7 ± 5.9	51.1 ± 2.1
SrO	1.5	1.5 ± 0.1	1.4 ± 0.5	1.0 ± 0.2
ZrO_2	3.8	3.9 ± 0.1	4.2 ± 0.4	4.4 ± 0.2
OTHER	4	2.7 ± 0.1	3.0 ± 0.3	2.5 ± 0.2
TOTAL	100	100	100	100

Molybdenum-rich droplets were found by electron microscopy in samples cooled slower than about 45°C/s. From phase separated residual glass, Mo-rich spheres would separate and subsequently crystallize while from a more homogenous residual glass Mo-rich phases would form cross-shaped and needle-like morphologies, the latter two morphologies occurring at temperatures 1000°C and above or after the formation of oxyapatite at temperatures 900°C and above. The composition of the needles was determined to be much different than the cross and droplet shaped Mo-rich phases. Due to the changing mechanisms and low crystal percentages of the Mo-rich phases (up to ~10 wt.%), the JMAK kinetic model was unable to accurately describe the crystallization of powellite.

Oxyapatite formed hollow hexagonal-shaped crystals that over time fill in to form more solid features. The fastest growth of oxyapatite in the isothermal experiments occurred at 1000°C, and crystalline oxyapatite formed in samples continuously cooled from the melt at rates slower than about 4°C/s. A sample with about 30 wt.% oxyapatite was created after an isothermal hold at 900°C for 24 hours. A JMAK analysis of the crystallization kinetics for oxyapatite indicate a diffusion-controlled growth mechanism, but the resulting activation energy, 58.8 ± 8.16 kJ/mol, was an order of magnitude lower than what was reported elsewhere for growth over a much narrower temperature range, indicating some significant changes in the growth conditions over the 700-1000°C experimental range in the present study.

This report provides data on the microstructural development of a borosilicate glass-ceramics as a function of time and temperature through isothermal and constant cooling experiments. Understanding the crystallization pathways is essential in developing acceptable waste forms to vitrify hazardous nuclear waste. Information from this study will be considered when further developing the glass-ceramic composition and processing techniques.

ACKNOWLEDGEMENTS

The authors thank the Department of Energy and the Nuclear Energy University Program (Project 15-8112) for supporting this work and Jarrod Crum (PNNL) for providing the glasses and discussing these results. They would also like to thank the many

Missouri S&T colleagues contributing to this work, including Elizabeth Peterson, Todd Sander, and Evan Musterman for help with the wedge mold and isothermal experiments, Derek Seymour for help with sample preparation and analysis, Eric Bohannon for help with XRD, Jenhsien Hsu, and Jingjing Qing for help with SEM and TEM.

REFERENCES

[1] "The Global Nuclear Energy Partnership: Greater Energy Security in a Cleaner, Safer World," (2018).

[2] "Review of DOE's Nuclear Energy Research and Development Program," The National Academies Press, Washington, DC, (2008).

[3] "Fuel Cycle Technologies Annual Review Meeting," Argonne Natioanl Laboratory, Argonne, IL (2011).

[4] D. Gombert, S. Piet, T. Trickel, J. Carter, J. Vienna, and B. Ebert, "Combined Waste Form Cost Trade Study," Idaho National Laboratory, Idaho Falls, Idaho (2008).

[5] M. J. Plodinec, "Borosilicate Glasses for Nuclear Waste Immobilization," *Glass Tech*, **41** 186-92 (2000).

[6] M. I. Ojovan and W. E. Lee, "An Introduction to Nuclear Waste Immobilization, 2 ed.," *Elsevier Science*, (2013).

[7] M. Magnin, S. Schuller, D. Caurant, O. Maje´rus, D. de Ligny, and C. Mercier, "Effect of compositional changes on the structure and crystallization tendency of a borosilicate glass containing MoO_3," *Ceram Trans*, **207** 59–68 (2009).

[8] J. V. Crum, A. L. Billings, B. J. Lang, J. C. Marra, C. P. Rodriguez, J. V. Ryan, *et al.*, "Baseline Glass Development for Combined Fission Products Waste Streams," Pacific Northwest National Laboratory, Richland, WA, (2009).

[9] A. Brehault, D. Patil, H. Kamat, R. E. Youngman, L. M. Thirion, J. C. Mauro, C. L. Corkhill, J. S. McCloy, and A. Goel. "Compositional Dependence of Solubility/Retention of Molybdenum Oxides in Aluminoborosilicate-Based Model Nuclear Waste Glasses," *The Journal of Physical Chemistry B* **122** [5] 1714-1729 (2018).

[10] J. V. Crum, B. J. Riley, and T. L. R., "Summary Report: Glass-Ceramic Waste Forms for Combined Fission Products," Pacific Northwest National Laboratory, Richland, WA (2011).

[11] J. V. Crum, L. Turo, B. Riley, M. Tang, A. Kossoy, and C. Jantzen, "Multi-Phase Glass-Ceramics as a Waste Form for Combined Fission Products: Alkalis, Alkaline Earths, Lanthanides, and Transition Metals," *Journal of the American Ceramic Society,* **95** 1297-1303 (2012).

[12] J. V. Crum, V. Maio, J. McCloy, C. Scott, B. Riley, B. Benefiel, *et al.*, "Cold crucible induction melter studies for making glass ceramic waste forms: A feasibility assessment," *Journal of Nuclear Materials,* **444** 481-492 (2014).

[13] J. V. Crum, J. J. Neeway, B. J. Riley, Z. Zhu, M. J. Olszta, and M. Tang, "Dilute condition corrosion behavior of glass-ceramic waste form," *Journal of Nuclear Materials,* **482** 1-11 (2016).

[14] J. V. Crum, B, McCarthy, J, Mayer, and C, Bonham, "Rheology of Borosilicate Glass Ceramic Melts," Pacific Northwest National Laboratory, Richland, WA, (2016).

[15] J.V. Crum, G.F. Piepel, C.C. Bonham, J.L. Mayer, J.J. Neeway, R.M. Asmussen, B.P. McCarthy, C.P. Rodriguez, C.L. Crawford and J.C. Marra. "Glass-Ceramic Matrix Study" U.S. Department of Energy Office of Nuclear Energy, (2017).

[16] M. R. Asmussen, J. J. Neeway, T. C. Kaspar, and J. V. Crum "Corrosion Behavior and Microstructure Influence of Glass-Ceramic Nuclear Waste Forms" *Corrosion Science Section*, **73** [11] 1306-1319 (2017).

[17] J. D. Vienna, J. V. Crum, G. J. Sevigny, and G. L. Smith, "Preliminary Technology Maturation Plan for Immobilization of High-Level Waste in Glass-Ceramics," Pacific Northwest National Laboratory, Richland, Washington, (2012).

[18] "Waste Acceptance Product Specifications (WAPS) For Vitrified High-Level Waste Forms," *DOE/EM-0093 Revision 3,* (2012).

[19] Y.G. Maldonado, F.A. Acosta, A.H. Castillejos, and B.G. Thomas, "Kinetic Study of the Devitrification of Mold Powder Slags," *AISTech,* **11** (2012).

[20] E. I. Peterson, T. P. Sanders, J. Smith, R. J. O'Malley, "Investigation of Mold Flux Crystallization by Rapid Quenching and Isothermal Aging in Molten Tin," *AISTech,* Nashville, TN, (2017).

[21] N. Chouard, D. Caurant, O. Majerus, J. L. Dussossoy, S. Klimin, D. Pytalev, R. Baddour-Hadjean, J. P. Pereira-Ramos, "Effect of MoO_3, Nd_2O_3, and RuO_2 on the crystallization of soda–lime aluminoborosilicate glasses," *J. Mater. Sci.,* **50** 219–241 (2015).

[22] I. S. Gutzow and J. W. P. Schmelzer, "The Vitreous State, second ed." *Berin Heidelberg: Springer-Verlag*, 219 -365 (2013).

[23] J. Malek, "Kinetic analysis of crystallization processes in amorphous materials," *Thermochinica Acta* **355** 239-253 (2000).

[24] J. Fourniera, E. Régniera, F. Faureb, X. Le Goff, H.-P. Brauc, E. Brackxd, O. Pineta, "Application of the JMAK model for crystal dissolution kinetics in a borosilicate melt," *Journal of Non-Crystalline Solids* **489** 77-83 (2018).

[25] J. Fourniera, E. Régniera, F. Faureb, X. Le Goff, H.-P. Brauc, E. Brackxd, O. Pineta, "Modeling of dissolution kinetics of rare earth crystals in a borosilicate glass melt," *Journal of Non-Crystalline Solids* **481** 248-253 (2018).

[26] O. Delattre, E. Régnier, S. Schuller, S. Poissonnet, N. Massoni, M. Allix, *et al.*, "Crystallization Kinetics of Apatite and Powellite in a Borosilicate Glass Under Thermal Gradient Conditions," *Physics Procedia,* **48** 3-9 (2013).

[27] D. Li, E. G. F. Sengers, F. J. J. G. Janssen, H. DE Waal, "Morphologies of CaMoO4 crystals in simulated nuclear waste disposal glass," *Journal of Materials Science Letters,* **11** 928-929 (1992).

[28] K. B. Patel, B. Boizot, S. P. Facq, S. Peuget, S. Schuller, I. Farnan, "Impacts of composition and beta irradiation on phase separation in multiphase amorphous calcium borosilicates," *Journal of Non-Crystalline Solids* **473** 1-16 (2107).

[29] D. A. McKeown, H. Gan, I. L. Pegg, "X-ray absorption and Raman spectroscopy studies of molybdenum environments in borosilicate waste glasses," *Journal of Nuclear Materials* **488** 143-149 (2017)

[30] E. Sarantopoulou, C. Raptis, S. Ves, D. Christofilos, G. A. Kourouklis, "Temperature and pressure dependence of Raman-active phonons of CaMoO4: an anharmonicity study," *J. Phys.: Condens. Matter* **14** 8925–8938 (2002).

[31] S. Guillot, S. Beaudet-Savignat, S. Lambert, P. Roussel, G. Tricot, R. Vannier, A. Rubbens, "Local relaxation in lanthanum silicate oxyapatites by Raman scattering and MAS-NMR," *J. Raman Spectrosc.* **42** 1455–1461 (2011).

[32] K. Brinkman, K. Fox, J. Marra, J. Reppert, J. Crum, and M. Tang, "Single phase melt processed powellite (Ba,Ca)MoO_4 for the immobilization of Mo-rich nuclear waste," *Journal of Alloys and Compounds,* **551** 136-142 (2013).

II. THE EFFECTS OF MICROSTRUCTURE ON THE DISSOLUTION BEHAVIOR OF A COMPLEX GLASS-CERAMIC WASTE FORM

Nicholas Roberts, Paul Porter, and Richard K Brow

Department of Materials Science & Engineering, Missouri University of Science & Technology, Straumanis-James Hall, 1400N. Bishop Ave, Rolla, MO 65409-0330

ABSTRACT

Borosilicate glass-ceramics developed by Pacific Northwest National Laboratories (PNNL) are intended to vitrify reprocessed spent nuclear fuel into environmentally safe waste forms. The multi-phase glass-ceramics exhibit complicated corrosion behavior. Borosilicate glass ceramics provided by PNNL were re-melted and quenched with different thermal histories to produce samples with a range of microstructures, described by analytical electron microscopy and x-ray diffraction. In particular, slower quench rates produced samples with greater fractions of crystalline powellite ($CaMoO_4$, up to ~10 wt. %) and oxyapatite ($Ca_2LN_8Si_6O_{26}$, up to ~30 wt. %). Product consistency tests (PCT) were performed to characterize the effects of microstructural development on elemental release rates. Atomic force microscopy (AFM), profilometry, and electron microscopy studies of polished, monolithic samples provide information about the relative recession rates of the residual glass and major phases, and reveal powellite to be the least durable phase, followed by the residual glass, and the oxyapatite. However, the thermal history dependent composition of the residual glass phase appears to have the greatest effect on the overall dissolution kinetics of this glass-ceramic.

1. INTRODUCTION

Efforts around the world are being made to reduce the volume of spent nuclear fuel and to develop viable waste storage options [1-3]. In the United States, the waste form must meet the requirements described in the Waste Acceptance Product Specifications (WAPS) [4]. Chemically durable borosilicate glasses are used worldwide and are understood to be a viable option to immobilize nuclear waste [3,5].

In order to understand the chemical durability of waste glasses, it is important to first understand the potential driving forces associated with dissolution. There are several stages for the dissolution of waste glasses in contact with groundwater in a geological depository, and these are summarized in Figure 1 [6]. In Stage I, the initial dissolution rate is dominated first by the exchange of ions in solution with weakly bonded alkalis in the glass and then by the hydrolysis of the glass network until a protective layer is formed. In Stage II, the dissolution rate decreases to the "residual rate" due to the saturation of silica in the surrounding aqueous environment, in equilibrium with the protective layer that formed in Stage I. If these equilibrium conditions change and crystals precipitate from the saturated solutions, then glass dissolution can accelerate in Stage III.

Section 1.3 of the WAPS states that the waste form needs to be more chemically durable than the environmental assessment (EA) reference glass, as determined using the Product Consistency Test (PCT) [4,7,8]. The product consistency test is a standard test procedure for determining the dissolution rates of waste glasses. For test method "A", a seven-day test, the stage I and possibly stage II dissolution reactions would dominate the overall release rates. For the present study, only stage I and possibly stage II dissolution behavior will be evaluated.

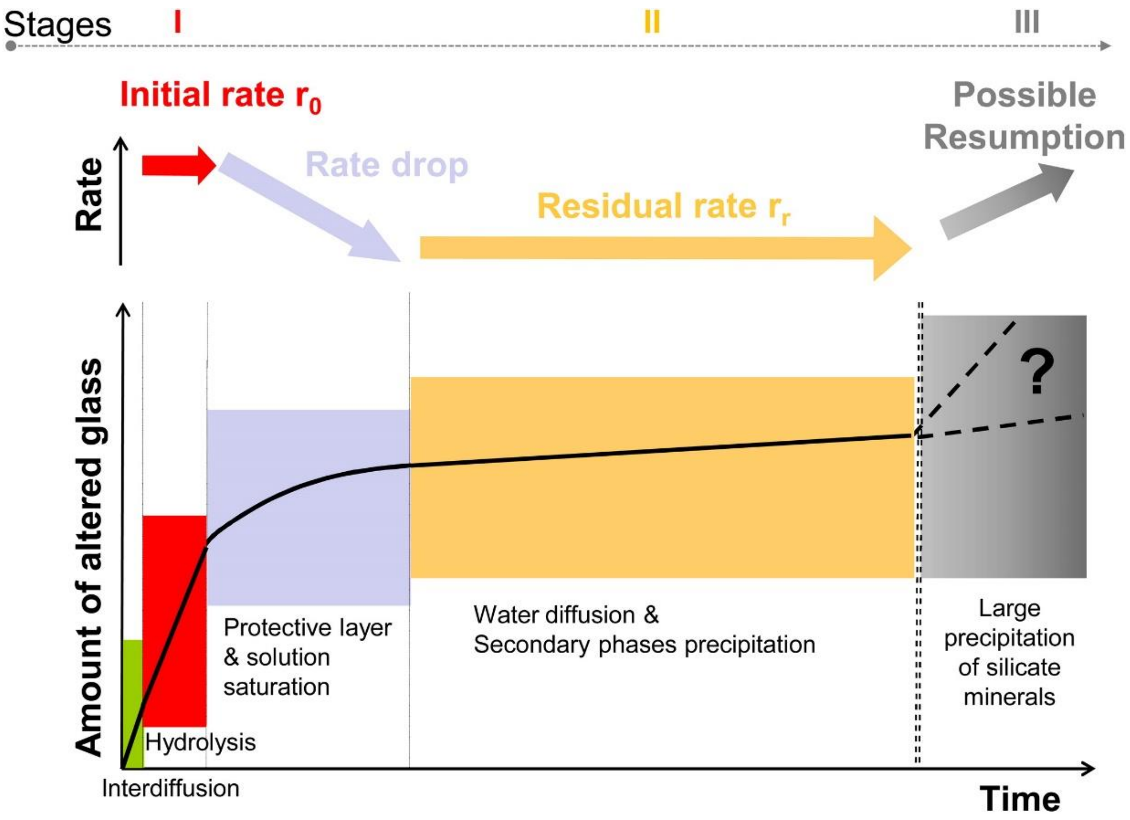

Figure 1. Long-term dissolution behavior of a waste glass [6].

Over the past decade, researchers at Pacific Northwest National Laboratory (PNNL) have done extensive work for the D.O.E Fuel Cycle Research and Development (FCRD) program developing borosilicate glass-ceramic compositions to immobilize wastes generated from aqueous spent nuclear fuel (SNF) reprocessing techniques [9-16]. The Collins CLT waste (Table 1) describes the non-radioactive components expected from reprocessed SNF and has large concentrations of transition metals, lanthanides and Cs-oxides that have relatively low solubilities in borosilicate glasses. To increase the loadings of waste like Collins CLT, PNNL researchers have developed glass-ceramic formulations that retain acceptable durabilities with greater waste loadings [9,16].

Table 1. Composition of Collins CLT waste [9].

Oxide	Content [mol%]	Oxide	Content [mol %]
MoO_3	19.719	CdO	0.621
ZrO_2	17.590	SeO_2	0.534
Nd_2O_3	11.279	Eu_2O_3	0.354
BaO	10.443	Ag_2O	0.353
Cs_2O	7.416	SnO_2	0.339
SrO	6.887	Gd_2O_3	0.322
Ce_2O_3	6.859	Rh_2O_3	0.226
La_2O_3	3.527	Br	0.205
Pr_2O_3	3.187	PdO	0.100
TeO_2	2.985	Pm_2O_3	0.036
Sm_2O_3	2.240	Sb_2O_3	0.028
Y_2O_3	2.019	In_2O_3	0.007
Rb_2O	1.641	Tb_2O_3	0.006
RuO_2	1.076	**Total**	**100.000**

A variety of different crystal phases have been detected in the glass-ceramics developed at PNNL for vitrifying the Collins CLT waste, including oxyapatite ($Ca_2Nd_8Si_6O_{26}$), Ln-borosilicate ($Gd_3BSi_2O_{10}$), powellite ($(Ca,Sr)MoO_4$ or $(Ca,Ba)MoO_4$), $CsLiMoO_4$, $La_2Mo_3O_{12}$, pollucite ($CsAlSiO_4$), $Zr_{0.9}Ce_{0.1}O_2$, Y_2O_3, and RuO_2 [16]. The effects of thermal history on the growth and morphology of the oxyapatite and powellite phases in a glass developed by PNNL are described in an earlier study [17]. In this paper, the relationship between microstructure and aqueous corrosion processes are described

In preliminary PCT studies at PNNL, glass-ceramics based on low (< 25 mass%) waste-loadings, the release rates of Si, B, Na, and Li were all found to be an order of magnitude below the respective benchmarks established with the EA reference glass [9]. The release rate of Mo from this composition (3.5 mass% Mo, nominal) was substantially lower (0.3 g/L) for samples rapidly quenched from the melt, compared to slowly cooled

(1.06 g/L), following the center-line canister cooling (CCC) protocol shown in Table 2. No crystalline features were found in the plate-quenched sample, whereas oxyapatite and powellite were identified in the CCC-sample. It was believed that the greater release of Mo from the slowly cooled sample was due to the preferential dissolution of the molybdenum-rich phase.

Table 2. Treatment schedule comparable to the CCC of a waste storage canister [9].

Step	Start Temperature (°C)	Rate (°C/min)	Step Duration (hours)
1.	1200 - 1150	0	Preheat 0.5 hours then fast cool
2.	1150 - 1050	~ -7	0.2
3.	1050 - 950	-0.935	1.8
4.	950 - 886	-0.288	3.7
5.	886 - 845	-0.108	6.3
6.	845 - 626	-0.205	17.8
7.	626 - 400	-0.126	29.9
8.	400	0	Dwell 1 hour

In studies of glasses with waste loadings up to 50 wt.%, samples cooled using the CCC profile were tested under static dissolution conditions for various times [10]. Mo release rates significantly increased (0.05 to 0.4 g/L) when the MoO_3 composition increased from 6.25 wt.% to 6.95 wt.%. It was believed that Mo was mostly contained in the powellite phase in the samples with lower Mo concentrations (6.25 wt.% and less) and the increase in Mo leach rate was due to the release of Mo in the residual glass phase. Nd release rates were very low, indicating that oxyapatite crystals were more durable than the residual glass. The release rates of boron and sodium from the glass-ceramic with 50 mass% CLT waste were relatively higher (+0.1g/L), leading to the conclusion that the residual glass is less durable than the crystalline phases.

To aid the development of borosilicate glass-ceramics at PNNL, a statistical compositional matrix was designed to determine the effects of composition on the important properties of these materials [16]. The centroid composition from the test matrix is the glass-ceramic composition used in this report. Three different dissolution tests were used in that study to characterize the chemical durability of these glass-ceramics. One test, a modified PCT method “B”, static dissolution test, was used to analyze samples cooled according to the CCC after 7, 28, 119, 448 days. The second test was a single-pass flow-through, SPFT, test used on samples cooled at 4, 1, and 0.25 times the CCC cooling rate [15,16]. The third test was a modified single-pass flow-through, MSPFT, test used to further analyze the CCC-cooled samples by weight loss measurements and dimensional changes using scanning electron microscopy [13,16]. From the PCT tests, the effects of composition on the release of various components from the glass were determined and are summarized in Table 3 [16]. B, Na, and Mo were found to have the fastest release rates; Mo was released primarily from powellite crystals and Na and B were released from the residual glass. The SPFT dissolution tests showed that regardless of cooling rate, pH or flow rate, the powellite crystals corroded fastest, followed by the residual glass phase, with the oxyapatite phase the most stable. The MSPFT dissolution determined that the residual glass dissolved fastest.

These earlier studies indicate that changes in microstructure and composition of the different phases have a significant effect on the overall dissolution rates of these complex borosilicate glass-ceramics. This work describes the effects of cooling rate of the centroid composition from the PNNL test matrix [16] on chemical durability, to better understand the relationships between microstructural and dissolution rates. Slower cooling rates changed the types and percentages of the crystalline phases and altered the composition of the residual glass to affect the overall dissolution rates of the waste material.

Table 3. Compositional effects on elemental release rates [16].

Glass Component	**Trend increasing/decreasing release rates**
Al_2O_3, ZrO_2	decrease in B, Li, Na, Cs, Si
SiO_2	decrease in B, Cs
B_2O_3, Na_2O, MoO_3	increase in B, Li, Na, Cs, Si
Ln_2O_3	increase in B, Li, Na, Cs
Li_2O	increase in B, Si / decrease in Li
CaO	no effect

2. EXPERIMENTAL METHODS

2.1. GLASS-CERAMIC COMPOSITION

The nominal molar composition of the as-received centroid composition glass, with a waste loading of 47 wt.%, is shown in Table 4 [16]. Sample preparation information can be found in reference [16]. 500 g batches from reagent-grade oxides were melted twice in a lidded Pt/10% Rh crucible between 1250°C and 1450°C for 1 hour and quenched on an Inconel plate in air.

2.2. THERMAL TREATMENTS

Samples were prepared with different microstructures by melting the centroid composition at 1300°C for one hour, then quenching at different rates, using several techniques described in [17]. Table 5 summarizes the conditions used to prepare samples in this study.

Table 4. Glass composition [16].

Oxide	**Content [mol%]**	**Oxide**	**Content [mol%]**
SiO_2	47.674	TeO_2	0.641
B_2O_3	11.329	Sm_2O_3	0.481
CaO	8.445	Y_2O_3	0.433
MoO_3	4.229	Rb_2O	0.353
Al_2O_3	3.789	RuO_2	0.232
Na_2O	4.069	CdO	0.135
ZrO_2	3.774	SeO_2	0.116
Li_2O	3.247	RhO_2	0.089
Nd_2O_3	2.427	Eu_2O_3	0.076
BaO	2.241	Ag_2O	0.075
Cs_2O	1.591	SnO_2	0.072
SrO	1.476	Gd_2O_3	0.070
Ce_2O_3	1.472	PdO	0.023
La_2O_3	0.757	Total	100.000
Pr_2O_3	0.684		

Table 5. Quench rates and phases for each sample [17].

Quenching Technique	**Cooling Rate [°C/s]**	**Phases (Quantitative XRD) [wt. %]**	
roller quench	>100	x-ray amorphous	
copper wedge step 2	5.8	x-ray amorphous	
copper wedge step 1	5.1	x-ray amorphous	
steel wedge step 1	4.1	x-ray amorphous	
air-cool	3.4	$Ca_2Nd_8Si_6O_{26}$	8.4 ± 1.3
		$CaMoO_4$	1.2 ± 0.4
furnace-cool	0.1	$Ca_2Nd_8Si_6O_{26}$	21.4
		$CaMoO_4$	3.2
CCC	0.008	$Ca_2Nd_8Si_6O_{26}$	15.2
		$CaMoO_4$	8.5

2.3. PRODUCT CONSISTENCY TEST

The product consistency test (PCT) was used to measure elemental release rates from glasses with various cooling profiles. Sample preparation was done according to the procedures described for method “A” [7]. Powders were produced with an agate mortar and pestle and sieved between 75 and 150 µm, then reacted with DI water in Teflon vessels at 90 ± 2°C for 7 days. All experiments were performed in triplicate. Samples were then filtered (4 µm syringe filter) and leachate concentrations were evaluated using an inductively coupled plasma optical emission spectrometer, ICP-OES, (PerkinElmer Optima 2000 DV, Norwalk, USA) to measure the release rates of Si, B, Ca, Na, Ba, Nd, and Mo. The release rates were normalized to the concentrations of each element in the target composition and reported as g/m^2, as outlined in the ASTM procedure [7].

2.4. DIFFERENTIAL DISSOLUTION TEST

The relative dissolution rates of different microstructural features were determined using techniques to measure changes in local topology. Samples with different thermal histories were cut and ground to sizes ~1 x 1 x 0.1 cm, then polished using a 0.25 µm diamond suspension. A titanium layer (~150 nm thick, Figure 2) was deposited on part of the surface of the polished samples using electron beam evaporation to provide a reference for sample height, Figure 2. Samples were then placed, Ti-layer facing up, in Teflon containers filled with ~500 mL of deionized water (90°C) for various times, and weight changes were recorded after drying the samples in room temperature air.

Atomic force microscopy, AFM, and profilometry were used to measure changes in the heights of different phases in the glass microstructure relative to the titanium layer, after dissolution of monolith samples at 90°C for various times. A Digital Instrument Nanoscope IIIA scanning probe microscope was used for the AFM experiments. The samples were scanned in tapping mode at 2 Hz with an AppNano ACTA-10 probe. The scans produced 3D maps of the surface and at least 10 measurements were used to determine the relative recession rates of the different phases. A KLA Tencor P-17 stylus profiler with Profile 8.1 software was also used to measure changes in surface topology of corroded glasses. Scan lengths 200 – 1000 µm were analyzed at a rate of at 10 µm/sec sampling at 50 Hz.

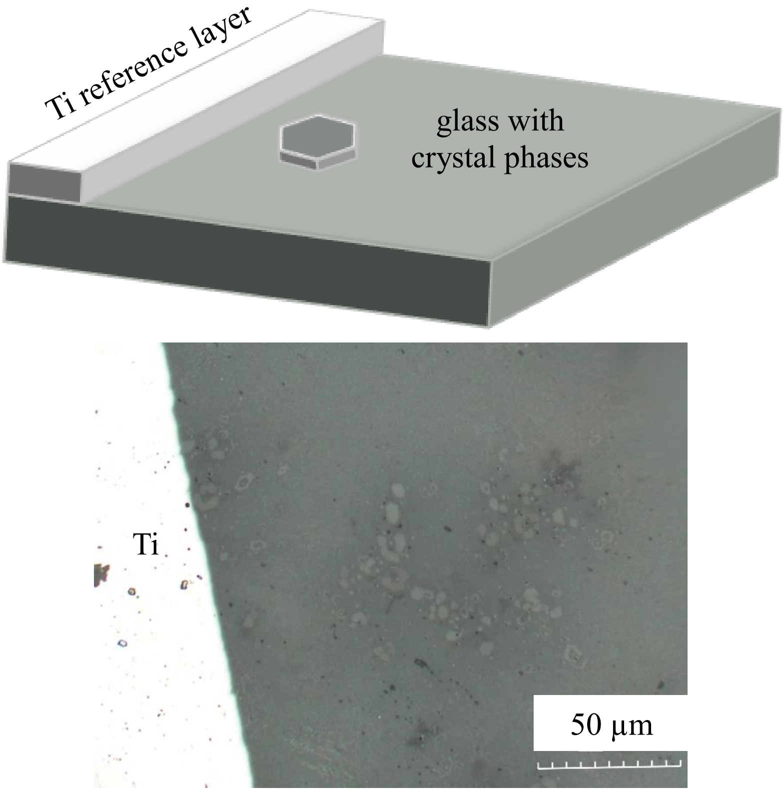

Figure 2. Top) schematic diagram of a sample from a differential dissolution test, with the titanium reference layer and a crystal exposed after dissolving away the surrounding glass. Bottom) an optical image of the air-cooled sample coated with ~150 nm of titanium before a dissolution test.

2.5. MICROSTRUCTURAL CHARACTERIZATION

A dual beam scanning electron microscope (SEM, FEI Helios NanoLab 600) with energy-dispersive x-ray spectroscopy (EDS) was used to characterize samples before and after the corrosion tests. The samples were sputter-coated with AuPd before they were loaded into the SEM. Micrographs were collected at different magnifications, electron voltages, and currents. EDS maps were obtained using Oxford Instruments AZTEC software at various magnifications using 15 keV and 1.4 nA.

3. RESULTS

3.1. EFFECTS OF THERMAL HISTORY ON MICROSTRUCTURE

In the first part of this study, the effects of thermal history on the development of the microstructure of the centroid composition are described [17]. Figure 3 shows representative microstructures from that study of the samples examined here. When melts were cooled by roller quenching, an aluminosilicate droplet phase separates from a borosilicate matrix that has large concentrations of alkalis (Na, Li, Cs), alkaline earths (Ca, Ba), lanthanides, and transition metals, including Mo, Figure 3a. The aluminosilicate droplets increase in size in samples cooled at slower rates to 4.1°C/s (~150 nm), shrink and seem to disappear from samples cooled at 0.1°C/s and slower. Table 6 shows the compositions of the droplet and matrix phases from the sample cooled at 4.1°C/s. Samples cooled in the wedge mold experiments (5.8, 5.1, 4.1°C/s) have Mo-rich droplets (Figure. 3b) that are x-ray amorphous but were found by electron diffraction to be related to crystalline powellite ($CaMoO_4$). The composition of the powellite droplets from the sample cooled at 4.1°C/s is given in Table 6. The sample cooled at 3.4°C/s has larger powellite droplets that do diffract x-rays, as well as hexagonal oxyapatite ($Ca_2LN_8Si_6O_{26}$) crystals (Figure 3c), and the fraction of the latter has increased in the sample quenched at 0.1°C/s (Figure 3d). The sample cooled using the CCC profile (on average, 0.008°C/s), had the largest oxyapatite crystals, and the principal morphology of the powellite crystals changed from spheres to crosses. However, the composition of these cross-like crystals is similar to what was determine for the spherical particles in the slower quenched samples (Table 6). Table 6 also gives the composition of the oxyapatite crystals in the CCC-cooled sample.

3.2. ION RELEASE VALUES FROM PCT

Ion release rates from the PCT tests on samples cooled at different rates are shown in Figure 4. The data from these analyses are given in Table B.1 of Appendix B. In general, the release rate for Ba, Ca, Mo, Na, and B all increase with decreasing quench rates, with maxima for each element at 0.1°C/s. The rates decrease again from the CCC-treated sample. Si and Nd release rates do not differ significantly from samples with different thermal histories, although the former has its lowest value from the CCC-treated sample. The roller quench, 0.1°C/s, and CCC samples were sent to Savanah River National Laboratories and the PCT test preformed on them. Values were generally lower, however the same trend with cooling rate was seen. Additional data from the SRNL tests can be found in Appendix B.

3.3. RECESSION RATE VALUES FROM THE DIFFERENTIAL DISSOLUTION TESTS

Figure 5 shows SEM/EDS images from the surface of a sample cooled at 3.4°C/s exposed after exposing the surface to 90°C deionized water for 12.5 days. Cross-sections of oxyapatite crystals, rich in Nd and Ca, can clearly be seen, along with smaller Mo-rich spheres. The SEM image of the sample cracks believed to be created when the corroded sample was dried.

Table 6. Compositions of the major phases in the glass.

	residual glass		**powellite**		**oxyapatite**
	(TEM)		**(TEM)**	**(SEM)**	**(SEM)**
	4.1°C/s droplet	**4.1°C/s matrix**	**4.1°C/s - sphere**	**CCC - cross**	**CCC**
	[At%]	[At%]	[At%]	[At%]	[At%]
Al_2O_3	8	2	0	1	0
BaO	0	4	2	2	0
CaO	1	10	29	27	19
Ce_2O_3	1	3	1	1	7
Cs_2O	0	1	0	0	0
La_2O_3	1	2	0	1	2
MoO_3	1	6	44	48	0
Na_2O	0	1	3	2	0
Nd_2O_3	1	6	2	1	13
Pr_2O_3	0	2	0	0	4
Rb_2O	0	0	0	0	0
RhO_2	0	0	0	0	0
RuO_2	0	0	0	1	0
SiO_2	79	50	14	5	48
Sm_2O_3	1	2	1	0	3
SrO	0	0	5	8	1
TeO_2	1	3	0	1	0
Y_2O_3	1	1	0	0	1
ZrO_2	5	7	0	1	0
TOTAL	100	100	100	100	100

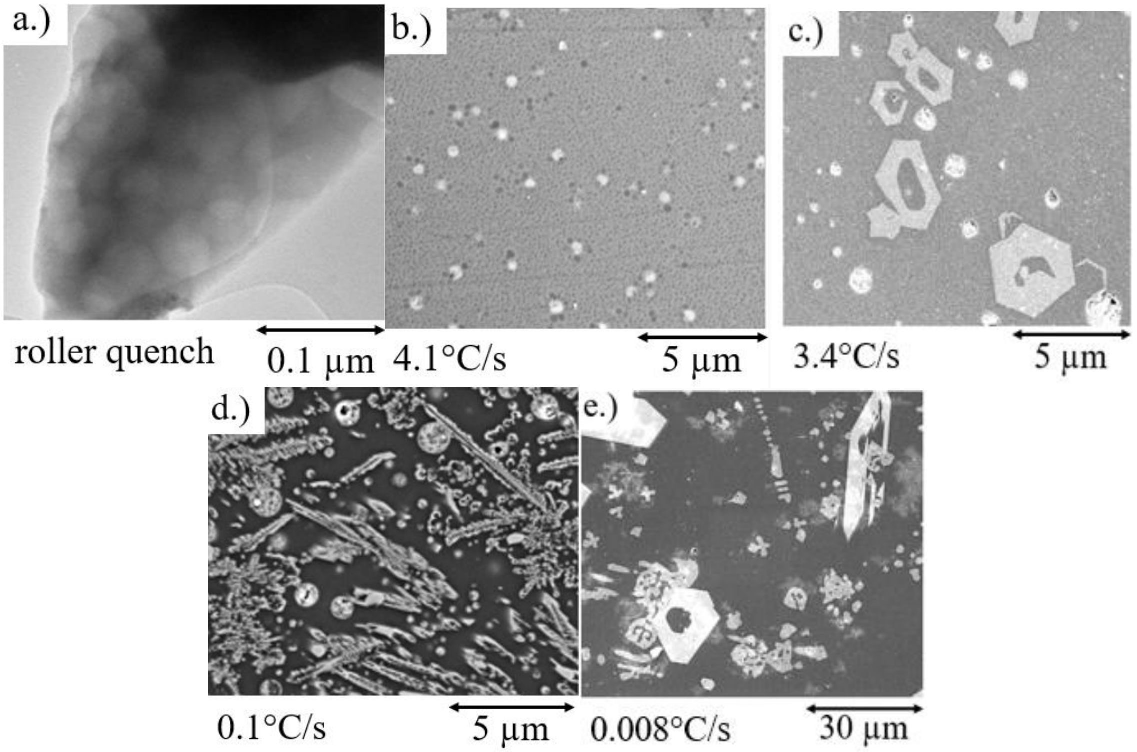

Figure 3. Electron images from samples quenched at different rates; a) roller quench (TEM), b) 4.1°C/s, c) 3.4°C/s, d) 0.1°C/s, and e) 0.008°C/s.

Figures 6 and 7 show AFM scans around the same oxyapatite crystals shown in Figure 5. Clearly, the glass around the crystals has been etched away at a faster rate than the crystals themselves, leaving the latter at greater relative heights. Also shown in Figure 7 is an example of the height scan across the corroded surface which shows that the average change in height (Δh) from the top of the crystal to the glass is 240 ± 90 nm. For the measurements from the Ti-layer to the glass surface (Figure 7, right), the Δh determined by subtracting the deposited Ti layer step-height (150 nm) from the step-height of the reacted sample had an average value of 260 ± 70 nm. The same sample was further reacted in 90°C DI water for a total of 18.75 days and the relative heights of the same areas and crystals were analyzed again. These results are summarized in Figure 9.

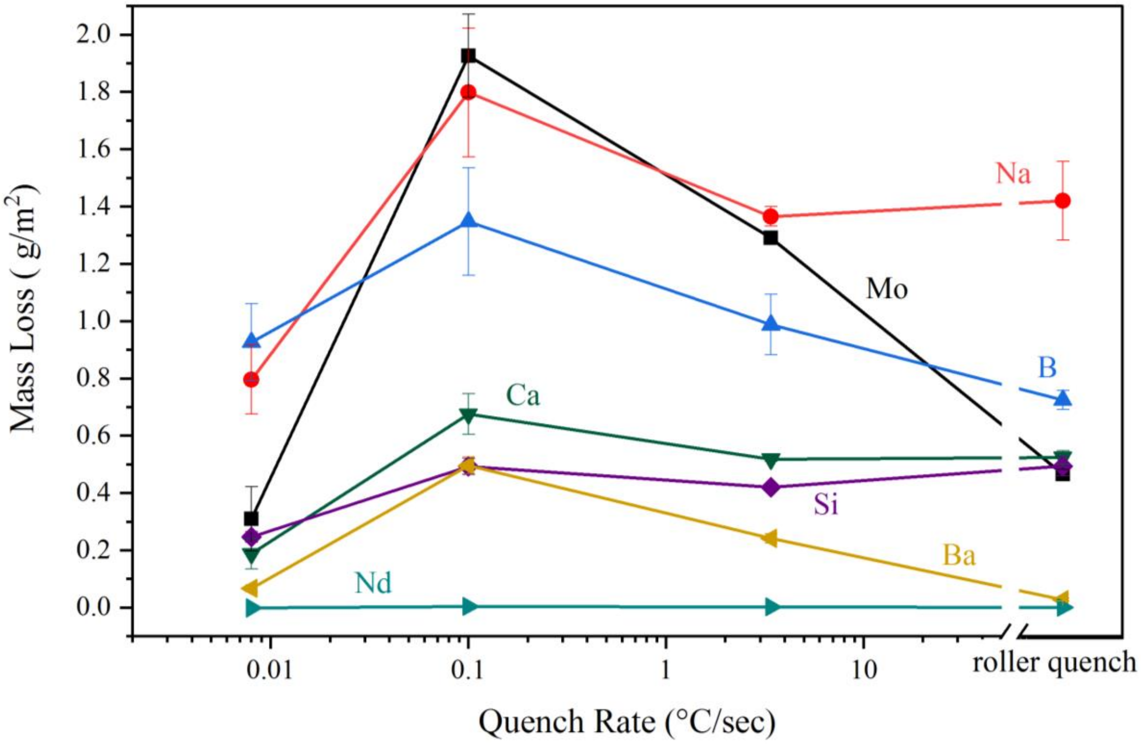

Figure 4. Seven-day PCT method “A” results for the centroid composition as a function of cooling rate. The lines are guides for the eye.

Profilometry was used to measure the relative recession rates of different phases that formed in samples quenched at different rates, using the titanium layer deposited on the original sample as a height reference. This layer thickness was determined to be 160 ± 10 nm and was assumed to be constant for all corrosion samples. Figure 8 shows example profilometer scans of a sample cooled at 3.4°C/s, before and after reaction in 90°C water for eight days. This sample showed a change of height (Δh) of 250 ± 30 nm.

The results from the profilometry and AFM experiments are shown in Figure 9 and reported in Appendix B, Table B.2. The AFM measurements of the 3.4°C/s follow the same trend as the profilometry test. The durability of the glasses decreases with decreasing quench rate. There appears to be a much larger relative recession rate of the sample cooled using the CCC profile (0.008°C/s).

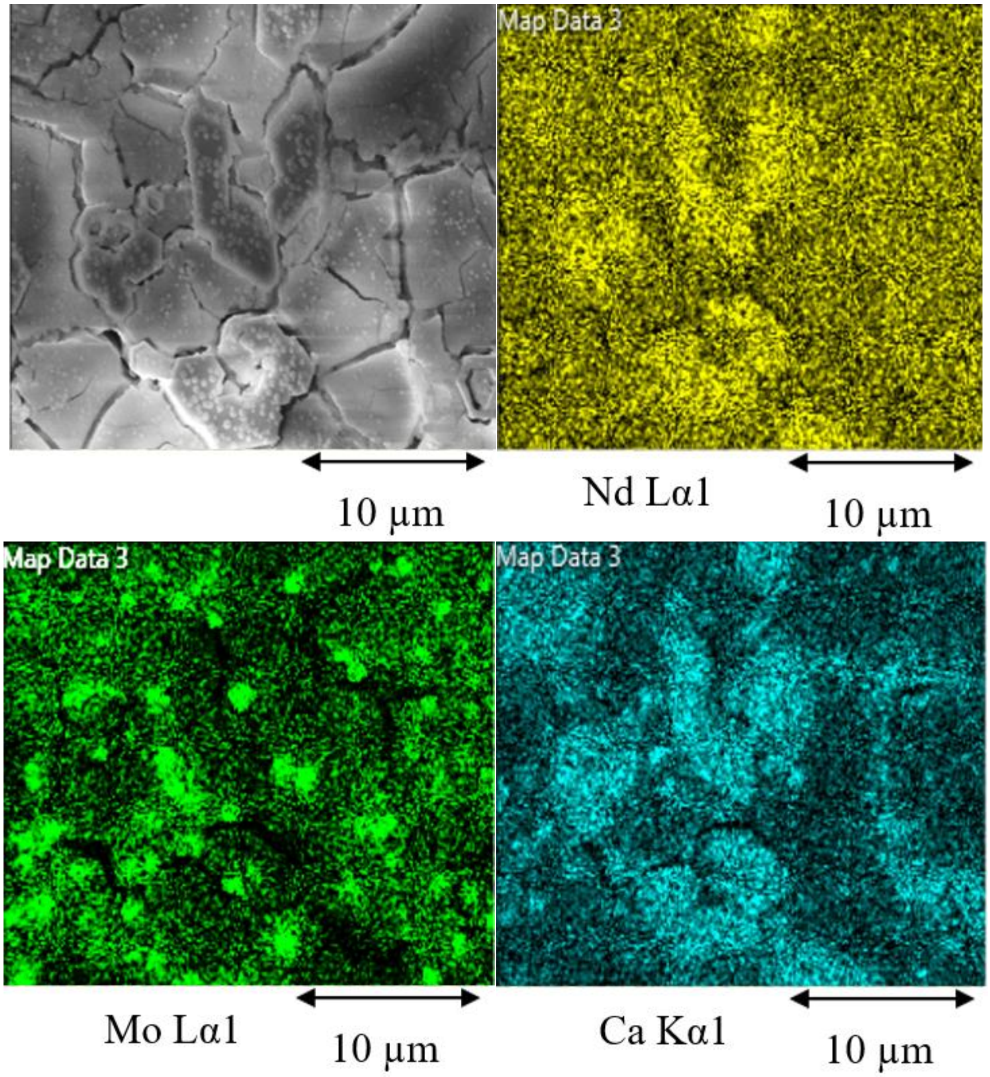

Figure 5. SEM micrograph and EDS maps from a sample cooled at 3.4°C/s, then reacted for how long in deionized water at 90°C.

Simple weight measurements, normalized to surface area, made before and after the reaction shows a similar trend with increasing dissolution rates from samples quenched at slower rates, as shown in Figure 10. However, this is only up to the sample at 0.1°C/s and at 0.008°C/s the weight loss rate decreases, similar to the PCT test. The data for the 0.1°C/s and 3.4°C/s were fit to a parabolic function with the equation also listed in Figure 10. The weight loss measurements can be found in Table B.3 Appendix B.

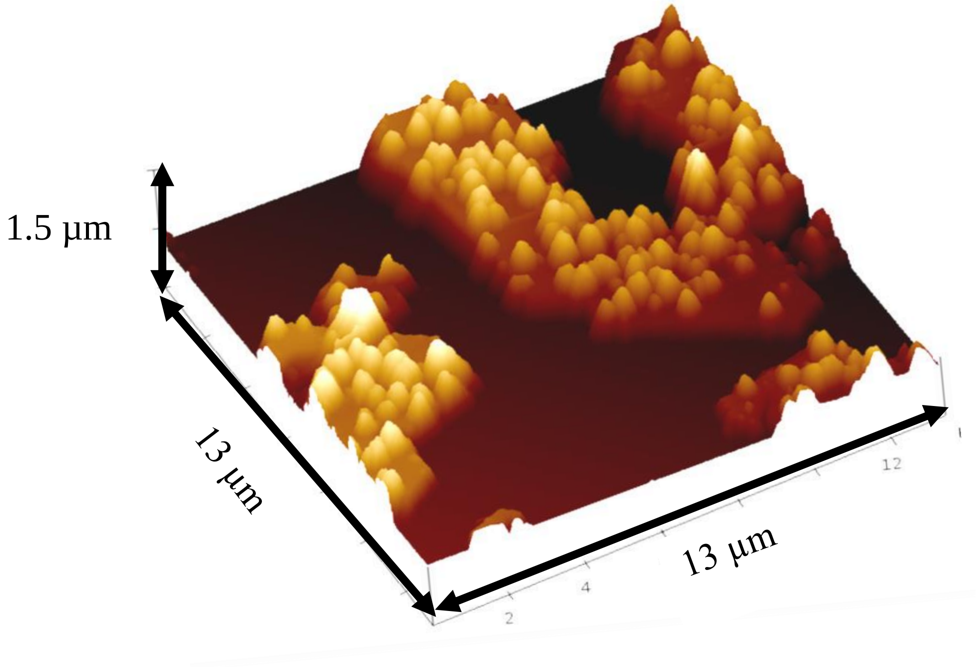

Figure 6. AFM scan of an oxyapatite crystal in the sample cooled at 3.4°C/s after 12.5 days in deionized water at 90°C.

Figure 11 shows micrographs of the surface of a CCC-quenched sample after one week in 90°C deionized water that clearly show pits left after the removal of a cross-like powellite crystals. The oxyapatite crystals remain. EDS analyses (not shown) reveal that the sub-micron crystals on the surface of this sample are rich in Zr.

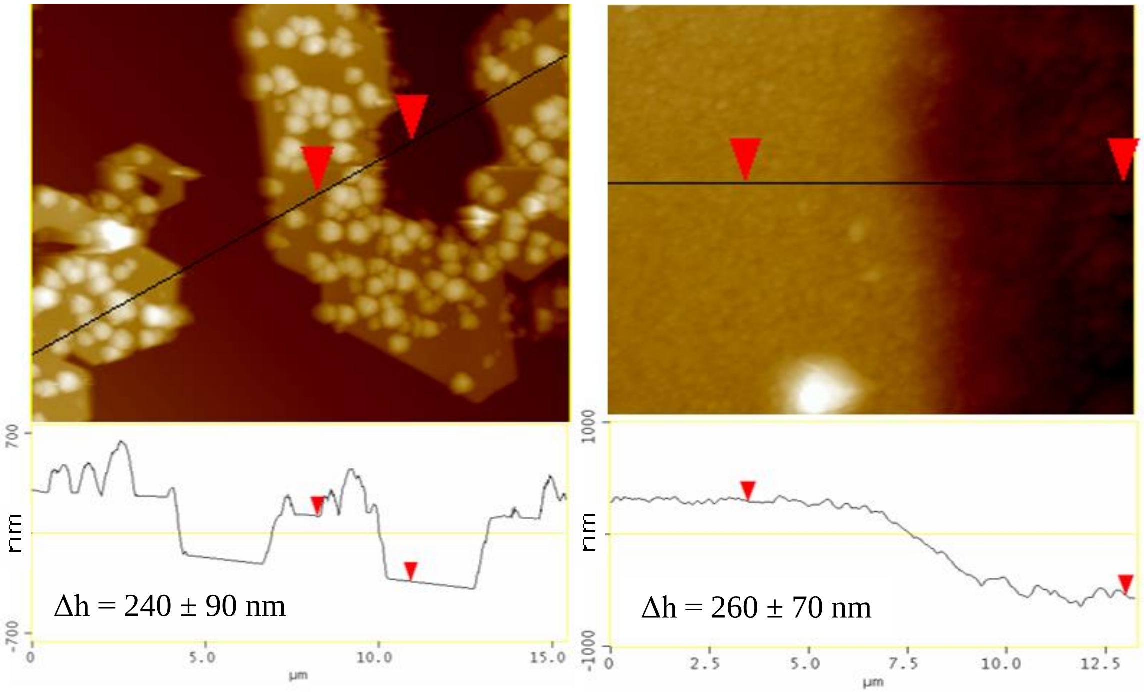

Figure 7. Left, example measurement of sample cooled at 3.4°C/s showing crystal to the glass measurements and, right, Ti coating to the glass measurements for the sample after 12.5 days in deionized water at 90°C.

The difference in height between the Ti layer, oxyapatite, residual glass, and molybdate phase was believed to be found using profilometry in the CCC sample due to the relatively large crystals, Figure 12. The step heights from the Ti layer (initially 150 nm) to the respective crystals post dissolution in DI water at 90°C for 7 days for the CCC sample were also calculated and are shown in Figure 12. The Ti layer is represented by the grey area shown being 150 nm thick. The step height from the Ti-layer to the oxyapatite crystals is shown with the red area, to the residual glass with the green area, and to powellite with the blue area. These measurements again show that oxyapatite dissolved out slowest followed by the residual glass followed by powellite. The change in height from the residual glass to the powellite crystals was found to be ~1 µm which in range with the size of a powellite crystal. The widths of the peaks match well with the size of oxyapatite and the width of the low valleys match well with the size of the powellite crystals as well shown in Figure 13 and Figure 11 right.

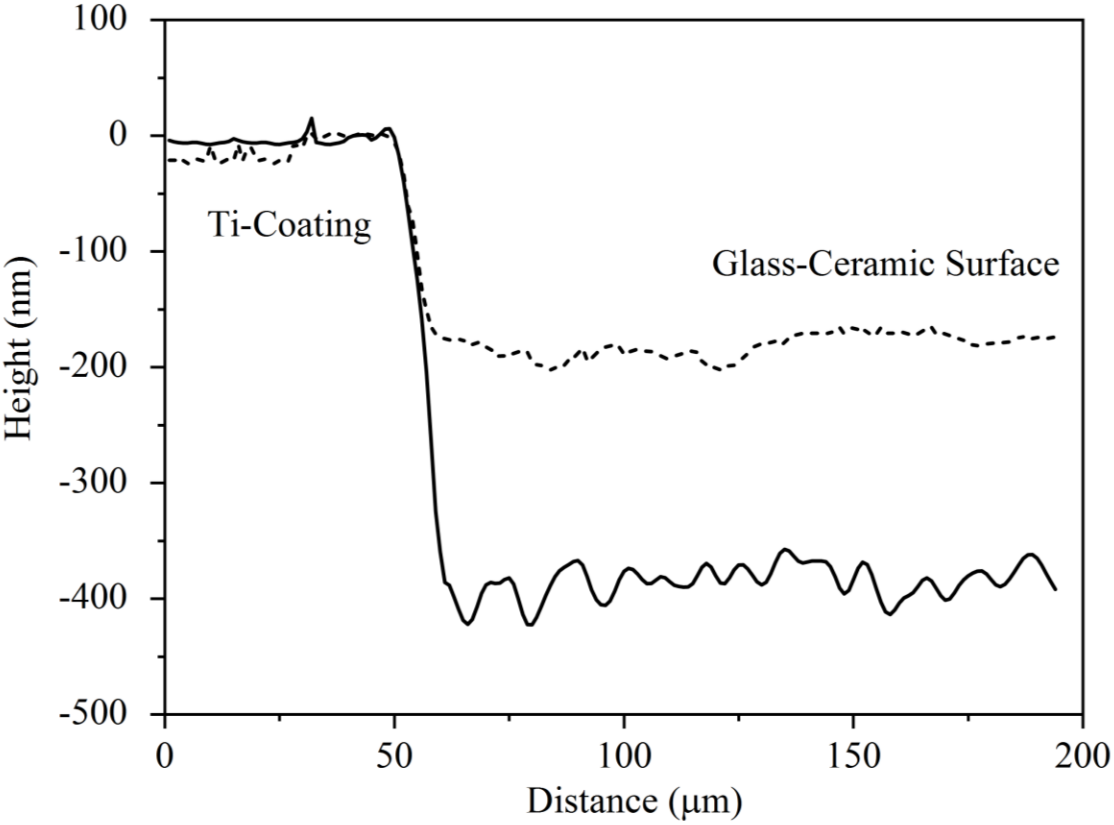

Figure 8. Example profilometry line scans of the sample quenched at 3.4°C/s before (dashed) and after (solid) reacting in 90°C deionized water for eight days.

4. DISCUSSION

The absolute ion-release rates from the PCT experiments (Figure 4) were significantly greater (~5X) than those reported by Crum et al. [16], listed in Table B.1 of Appendix B. However, the relative ion-release rates were found to follow a similar trend with ion release rates of Ba ≈ Si ≈ Ca < Mo ≈ Na < B.

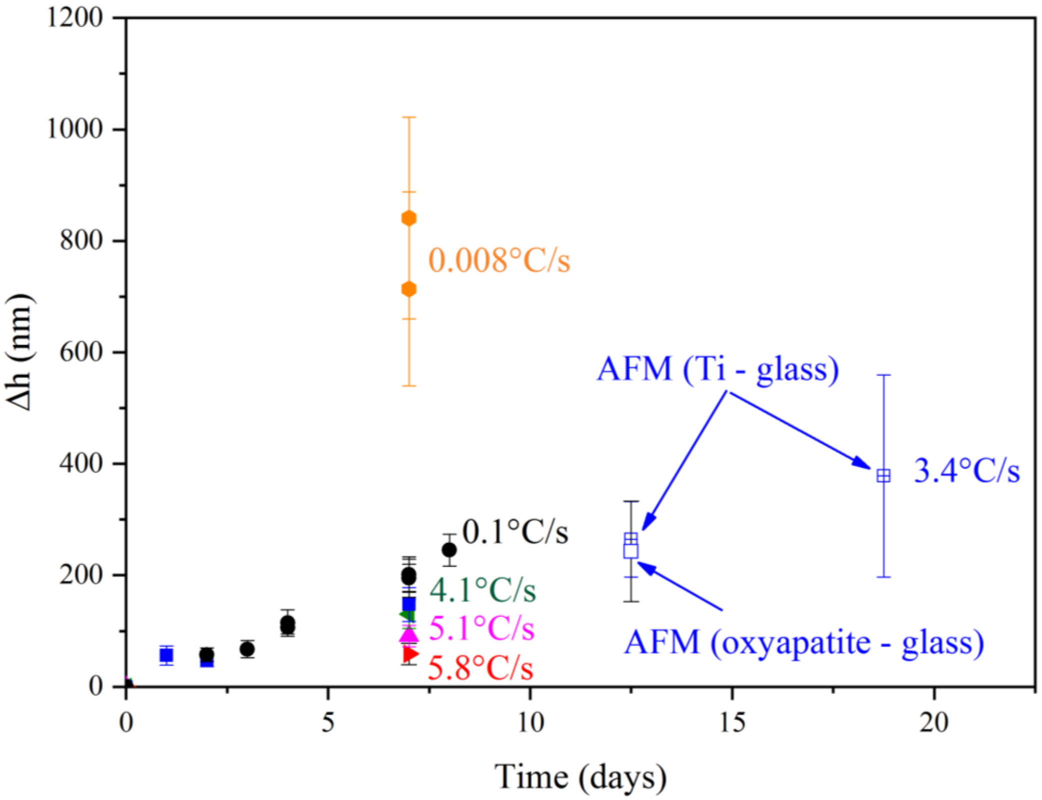

Figure 9. Profilometry (solid symbols) and AFM (open symbols) results in Δh as a function of time.

The change in the relative recession rate with quench rate can be associated with changes in the microstructure and associated changes in the composition of the residual glass. The residual glass compositions were calculated by subtracting from the nominal composition (Table 4) the oxide components associated with the powellite and oxyapatite crystalline phases determined by quantitative XRD [17]; these estimated residual glass compositions are given in Table 7. The composition of the roller quench glass is estimated to have the same composition as the as-received glass. Asmussen et al. [15] reported a similar residual glass composition of the CCC sample, as shown in Table 7. B (glass former) and Na (glass modifier) are predominantly retained in the residual glass and increase in relative concentrations in samples that are cooled more slowly and so have greater crystal fractions. The growth of oxyapatite crystals removes lanthanides (Nd) and some Ca and Si from the residual glass; little to no Nd is expected to remain in the residual glass of the 0.1°C/s and CCC samples, the latter in agreement with Asmussen et al. [15]. Increasing fractions of powellite, (Ca-rich)MoO_4, crystallize from the melts with decreasing cooling rate, pulling mostly Mo and some of the alkaline earth ions from the residual glass. Based on the quantitative XRD results, some Mo remains in the residual glass of the sample cooled at 0.1°C/s but is mostly sequestered from the glass phase in the CCC sample (Table 7).

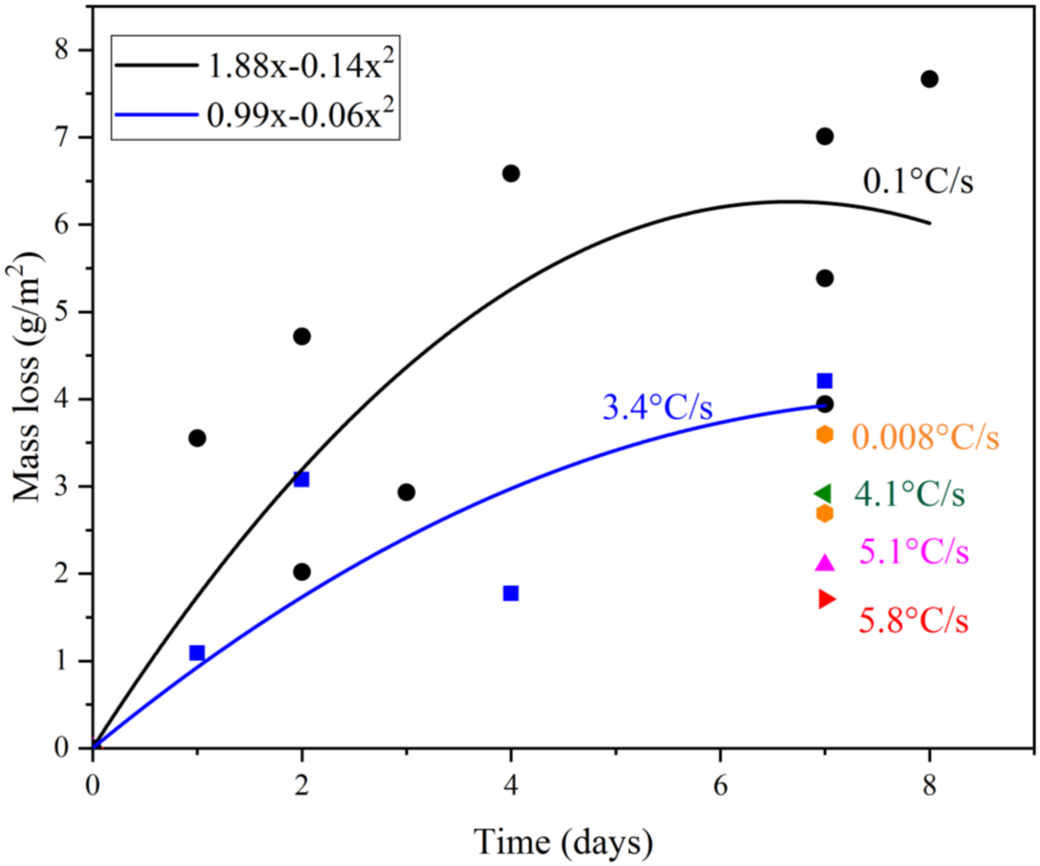

Figure 10. Mass loss from sample weight measurements in grams. The data for the 0.1°C/s and 3.4°C/s samples were fitted to a parabolic.

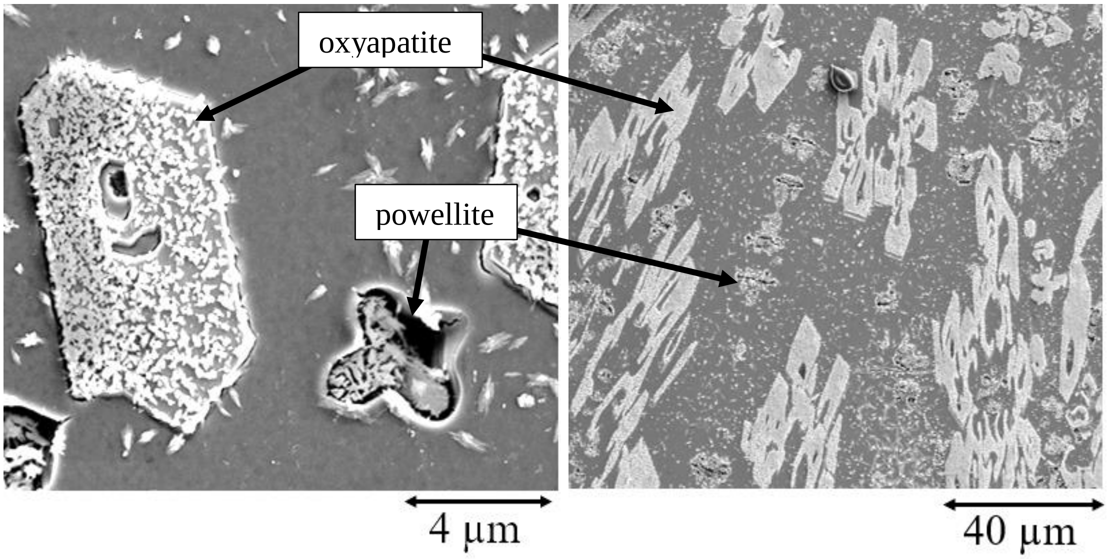

Figure 11. SEM images of a CCC sample after seven days in 90°C deionized water, showing left) a powellite and a oxyapatite crystal and right) a lower magnification image showing more representative sizes of the powellite and oxyapatite crystals.

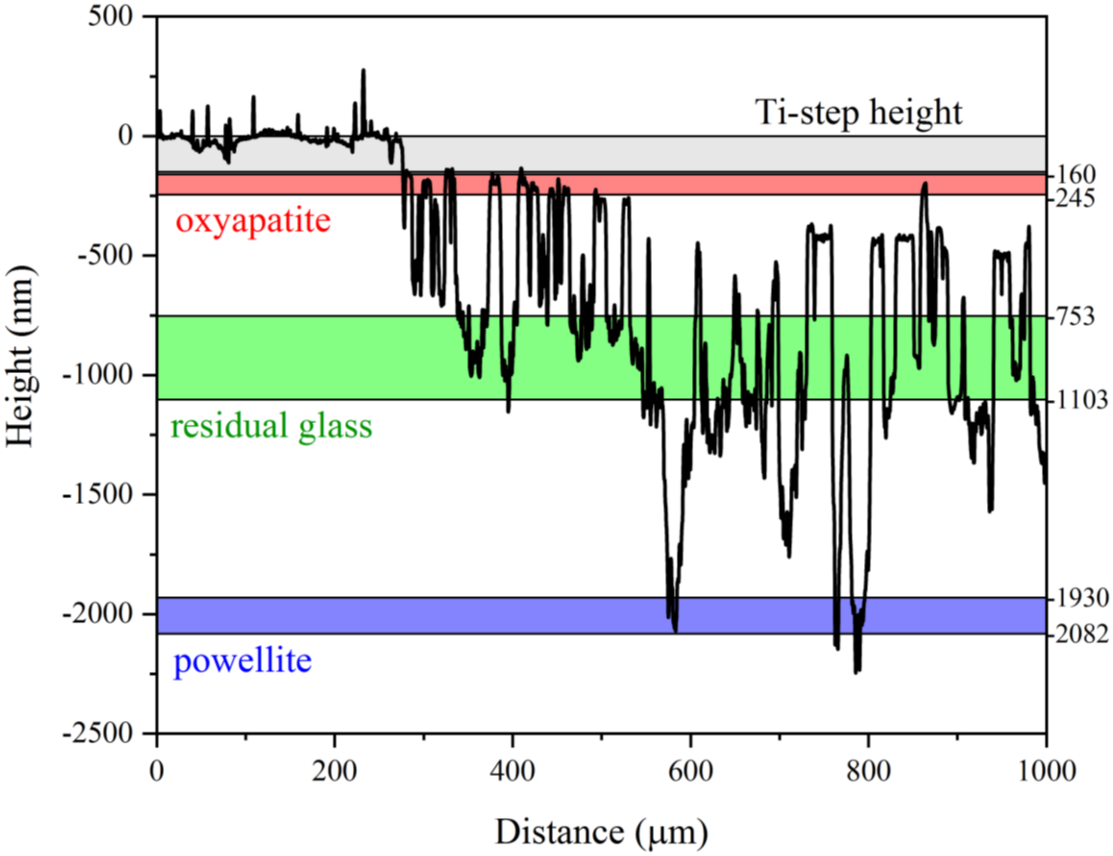

Figure 12. Profilometry scan of the CCC sample after 7 days in 90°C DI water.

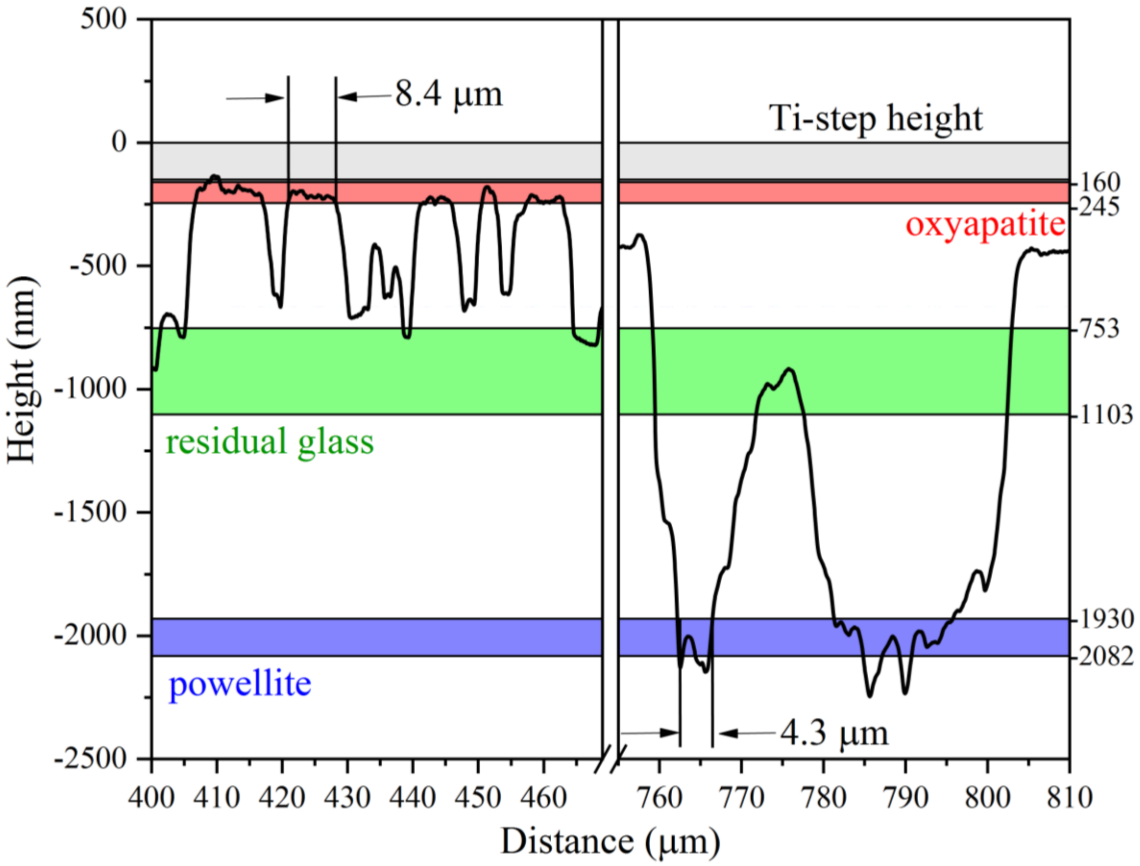

Figure 13. Expanded regions from Figure 12.

Nd has that lowest relative release rates, Figure 4, in these samples suggesting the oxyapatite phase to be more chemically durable than the other phases. As a function of quench rate, the release of Nd did not appear to change much, if any at all due to the release rates being near the detection limit of the ICP-OES, even in the sample where Nd was situated in the residual glass, Figure 14. Due to Nd also not releasing into solution even when incorporated in the less durable residual glass, the release rate of Nd would be most likely low compared to the actual release rate of oxyapatite, confirmed by Asmussen et al [15] The release rate of ions from the oxyapatite crystal may not be congruent with each other, allowing certain elements to preferentially dissolve out resulting in an increased dissolution rate of oxyapatite compared to Nd release rate. AFM scans, Figure 6, and SEM micrographs, Figure 5 and Figure 11 of oxyapatite crystals post dissolution clearly show oxyapatite to be more durable than the residual glass. Also, it is believed that the profilometry scans show peaks where oxyapatite crystals are located, Figure 12 and Figure 13, suggesting this is the most chemically durable phase.

Aside from Nd, from the fast-cooled roller quenched glass sample to the sample cooled at 0.1°C/s, ion release rates were found to increase, described by the PCT (Figure 4). Also, Δh were found to increase, described by the profilometry experiment (Figure 9), and the mass loss was found to increase, described by the weight loss measurements (Figure 10). These three tests confirm that the chemical durability of the glass-ceramic decreases with decreasing quench rate. Results from the profilometry experiments suggests this trend continues with even slower release rates. However, the ion release rates and mass loss were found to decrease from the 0.1°C/s to the 0.008°C/s sample. This could partly due to the change in the components of the residual glass. For example, Crum et al. [16] found increases in MoO_3 and Ln_2O_3 in the glass to always increase the dissolution of B and Na, Table 3. Therefore, in comparing the decrease in ion release rates and mass loss with quench rate from the sample cooled at 0.1°C/s to the sample cooled at 0.008°C/s, as more Mo and lanthanides crystallize out into powellite and oxyapatite respectively, B and Na release rates would decrease.

The general trends discussed by Crum et al and summarized in Table 3 can be simplified by comparing the change in B_2O_3, Al_2O_3, and SiO_2 in the residual glass composition with the change in B ion-release rates [16]. Shown in Figure 14, the B ion release rate was found to increase with the increase in B_2O_3. As stated before, B is situated in the residual glass regardless of cooling rate as an indicator for the recession rate of the residual phase. The increase in the release rate from the PCT test can be described by the B_2O_3 ratio as a function of quench rate, listed in Table 7. From the roller quench to the 0.1°C/s sample the B_2O_3 concentration in the residual glass significantly increases which then attributes to the higher B release rate and less durable glass.

Table 7. Estimated compositions of the residual glass phase in glass-ceramic samples created with different quenching rates and the estimated composition reported by Asmussen et al. [15].

Oxide	**roller quench [At.%]**	**3.4°C/s [At.%]**	**0.1°C/s [At.%]**	**CCC [At.%]**	**Asmussen et al. [15] CCC [At.%]**
Al_2O_3	3.8	3.9 ± 0.1	3.8 ± 0.5	4.5 ± 0.2	4.7
B_2O_3	11.3	12.1 ± 0.2	14.5 ± 1.2	13.4 ± 0.5	14.2
BaO	2.2	2.2 ± 0.1	2.2 ± 0.5	2.5 ± 0.1	2.8
CaO	8.4	7.6 ± 0.3	5.7 ± 1.5	5.6 ± 0.9	4.3
Ce_2O_3	1.5	1.2 ± 0.1	1.2 ± 1.1	0.9 ± 0.2	0.5
Cs_2O	1.6	1.6	1.8 ± 0.2	1.9 ± 0.01	2
La_2O_3	0.8	0.64 ± 0.1	0.6 ± 0.5	0.6 ± 0.1	0.4
Li_2O	3.2	3.5	4.2 ± 0.4	3.9 ± 0.1	4.1
MoO_3	4.2	4.2 ± 0.1	3.6 ± 0.6	1.2± 0.9	0.0
Na_2O	4.1	4.3 ± 0.1	4.1 ± 1.6	4.7 ± 0.2	4.8
Nd_2O_3	2.4	2.0 ± 0.1	1.7 ± 0.5	1.3 ± 0.3	0.9
Pr_2O_3	0.7	0.6 ± 0.1	0.5 ± 0.5	0.3 ± 0.1	0.5
SiO_2	47.7	48.0 ± 1.0	47.7 ± 5.9	51.1 ± 2.1	52.5
SrO	1.5	1.5 ± 0.1	1.4 ± 0.5	1.0 ± 0.2	0.5
ZrO_2	3.8	3.9 ± 0.1	4.2 ± 0.4	4.4 ± 0.2	4.7
other	2.8	2.7 ± 0.1	3.0 ± 0.3	2.5 ± 0.2	3.1
TOTAL	100	100	100	100	100

A less durable glass would recede faster, increasing water exposure to the molybdate phases. This added exposure allows more molybdate phases to dissolve which were described by Crum et al. [16] to not be a durable phase. Due to the relatively high release rates of Mo ions into solution, Mo release rates can act as indicators of the release rate for the molybdate phase. Other components such as Ba and Sr are also located in the molybdate phases but not always. Ba molybdates were found in most continuous cooling experiments, except the CCC sample, the reason for the increase in Ba concentration in the residual glass from the 0.1°C/s to the CCC sample, Table 7.

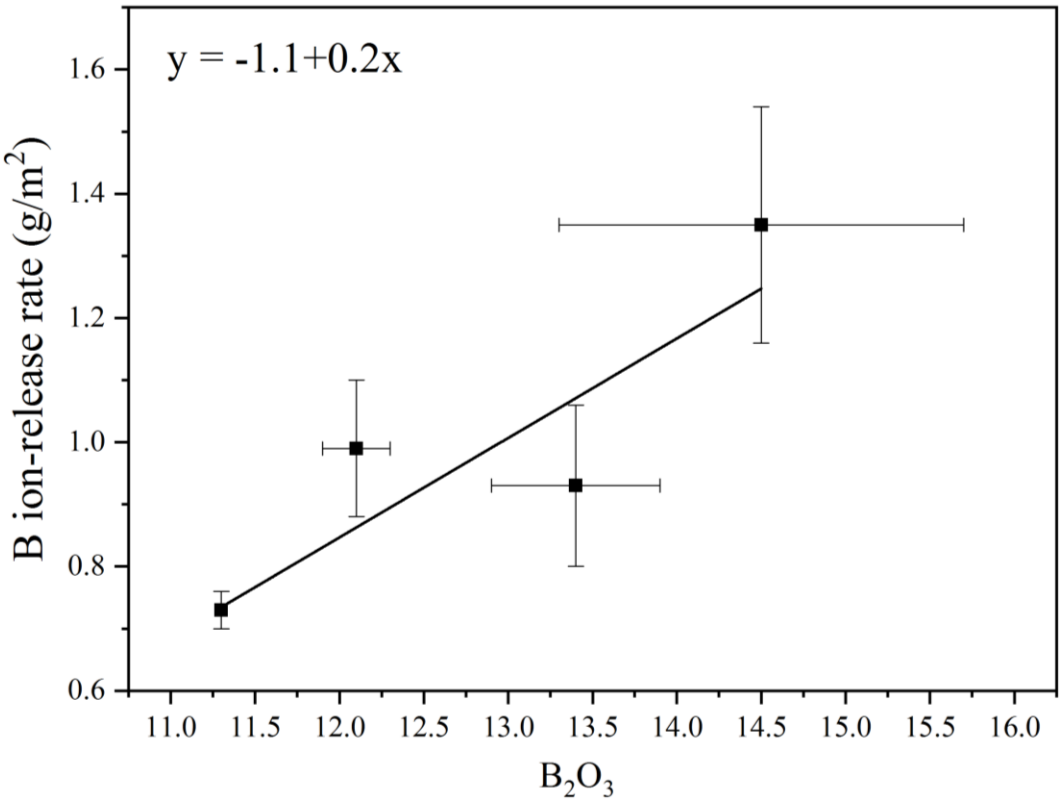

Figure 14. B ion release rate vs B_2O_3 concentration in the residual glass.

The reason for the decrease in the Mo ion-release rate from the 0.1°C/s to the CCC sample can be explained using the B_2O_3 concentration in the residual glass. With decreasing cooling rate, from 0.1°C/s to 0.008°C/s, the concentration of B_2O_3 greatly decreases which would cause an increase in the chemical durability. Slight differences in the morphologies and compositions of the molybdate phases between these samples could also attribute to changes in the dissolution behavior. However, it is believed that the composition of the residual glass, has the greatest influence on the chemical durability. In the CCC sample, the relatively durable residual glass does not recede as fast, limiting exposure of water to only the powellite crystals near the surface, which were found to completely dissolve out (Figure 11). Due to the powellite crystals being relatively large in the CCC sample, the dissolved particles left behind deep pits that greatly increased the step height measured with profilometry, Figure 9.

At quench rates, from the roller quench to the 0.1°C/s sample, ion-release rates increase due to the precipitation of oxyapatite crystals which increased the B_2O_3 concentrations by removing components like silica in the residual glass [16]. A decrease in the ion-release rates and sample mass is seen from the 0.1°C/s to 0.008°C/s samples described by composition of the residual glass having a reduced amount of B_2O_3.

This study provided additional information about the complex chemical durability of this borosilicate glass ceramic as a function of thermal history. The dissolution behavior of a wider range of quench rates and microstructures was examined. This study is intended to be used to help optimize the glass ceramic.

5. CONCLUSION

Ion release rates and recession rates were determined as a function of microstructure of a borosilicate high-level waste glass-ceramic. Eight samples were continuously cooled with quench rates ranging ~5 orders in magnitude. The residual glass was found to change as crystals precipitated resulting in differing dissolution behaviors described by the B_2O_3 concentration in the residual glass. Mo release rates increased from the roller quenched glass, to the sample cooled at 0.1°C/s but then decreased and was lowest in the CCC sample (~0.005°C/s). Results from this study clearly showed Nd was found to have very low release rates correlating the high relative chemical durability of oxyapatite, confirmed by SEM and AFM. SEM also found whole powellite crystals completely dissolved out in the CCC leading to believe the durability of powellite is less than the residual glass. Information from this experiment about the dissolution behavior of a borosilicate high-level waste glass-ceramic is intended to help assist in developing an optimized composition.

ACKNOWLEDGEMENTS

The authors thank the Department of Energy and the Nuclear Energy University Program (Project 15-8112) for supporting this work and Jarrod Crum for providing glasses and insight about the results. They would also like to thank the many Missouri S&T colleagues contributing to this work including Elizabeth Peterson for help with the wedge mold, Derek Seymour for help with sample preparation, Chuang Qu for help with depositing the titanium coatings, Eric Bohannon for help with XRD and AFM, Jenhsien Hsu for help with SEM and TEM.

REFERENCES

[1] "The Global Nuclear Energy Partnership: Greater Energy Security in a Cleaner, Safer World," (2018).

[2] "Review of DOE's Nuclear Energy Research and Development Program," The National Academies Press, Washington, DC, (2008).

[3] "Fuel Cycle Technologies Annual Review Meeting," Argonne Natioanl Laboratory, Argonne, IL (2011).

[4] "Waste Acceptance Product Specifications (WAPS) For Vitrified High-Level Waste Forms," *DOE/EM-0093 Revision 3*, (2012).

[5] M. J. Plodinec, "Borosilicate Glasses for Nuclear Waste Immobilization," *Glass Tech*, **41** 186-92 (2000).

[6] S. Gin, A. Abdelouas, L. J. Criscenti, W. L. Ebert, K. Ferrand, T. Geisler, M. T. Harrison, Y. Inagaki, S. Mitsui, K. T. Mueller, J. C. Marra, C. G. Pantano, E. M. Pierce, J. V. Ryan, J. M. Schofield, C. I. Steefel, and J. D. Vienna, "An international initiative on long-term behavior of high-level nuclear waste glass," *materials today* **16** [6] 243-248 (2013).

[7] ASTM, "Standard Test Methods for Determining Chemical Durability of Nuclear, Hazardous, and Mixed Waste Glasses and Multiphase Glass Ceramics: The Product Consistency Test (PCT)," *American Society for Testing and Materials International*, C 1285-14 (2008).

[8] C. M. Jantzen, "Nuclear Waste Glass Product Consistency Test Version 5.0 " Westinghouse Savannah River Company, Aiken, SC (1992).

[9] J. V. Crum, A. L. Billings, B. J. Lang, J. C. Marra, C. P. Rodriguez, J. V. Ryan, *et al.*, "Baseline Glass Development for Combined Fission Products Waste Streams," Pacific Northwest National Laboratory, Richland, WA, (2009).

[10] J. V. Crum, B. J. Riley, and T. L. R., "Summary Report: Glass-Ceramic Waste Forms for Combined Fission Products," Pacific Northwest National Laboratory, Richland, WA (2011).

[11] J. V. Crum, L. Turo, B. Riley, M. Tang, A. Kossoy, and C. Jantzen, "Multi-Phase Glass-Ceramics as a Waste Form for Combined Fission Products: Alkalis, Alkaline Earths, Lanthanides, and Transition Metals," *Journal of the American Ceramic Society*, **95** 1297-1303 (2012).

[12] J. Crum, V. Maio, J. McCloy, C. Scott, B. Riley, B. Benefiel, *et al.*, "Cold crucible induction melter studies for making glass ceramic waste forms: A feasibility assessment," *Journal of Nuclear Materials*, **444** 481-492 (2014).

[13] J. V. Crum, J. J. Neeway, B. J. Riley, Z. Zhu, M. J. Olszta, and M. Tang, "Dilute condition corrosion behavior of glass-ceramic waste form," *Journal of Nuclear Materials,* **482** 1-11 (2016).

[14] K. Brinkman, K. Fox, J. Marra, J. Reppert, J. Crum, and M. Tang, "Single phase melt processed powellite (Ba,Ca)MoO_4 for the immobilization of Mo-rich nuclear waste," *Journal of Alloys and Compounds,* **551** 136-142 (2013).

[15] M. R. Asmussen, J. J. Neeway, T. C. Kaspar, and J. V. Crum "Corrosion Behavior and Microstructure Influence of Glass-Ceramic Nuclear Waste Forms" *Corrosion Science Section*, **73** [11] 1306-1319 (2017).

[16] J.V. Crum, G.F. Piepel, C.C. Bonham, J.L. Mayer, J.J. Neeway, R.M. Asmussen, B.P. McCarthy, C.P. Rodriguez, C.L. Crawford and J.C. Marra. "Glass-Ceramic Matrix Study" U.S. Department of Energy Office of Nuclear Energy, (2017).

[17] N. Roberts, P. Porter, R. K. Brow, "Phase Development in a Complex Borosilicate Glass-Ceramic Waste Form," *Master's Thesis, Missouri University of Science and Technology* (2018).

SECTION

3. CONCLUSION

3.1. OVERALL SUMMARY

The objective of this study was to understand the effects of thermal history on the microstructural development and dissolution behavior of a borosilicate glass-ceramic loaded with waste from reprocessed spent nuclear fuel, and then to use this information to help optimize the design of these materials.

Continuous cooling and isothermal experiments provided data about the effects of thermal history on microstructure development, including the compositions, morphologies, and crystal percentages of the major crystalline phases. The major crystalline phase (up to 30 wt. %) was oxyapatite ($Ca_2LN_8Si_6O_{26}$) and its formation affected the development of the second most abundant (up to 10 wt. %) crystalline phase, powellite ($Ca_{1-x-y}Sr_xBa_yMoO_4$), and the composition of the residual glass. Insoluble heavy metal crystals, predominately Ru-rich, were also detected in trace amounts in the as-received and heat-treated composition.

On quenching from 1300°C, the waste-loaded melt first separates into aluminosilicate droplets and a matrix borosilicate liquid that contains high concentrations of lanthanides and transition metals, including Mo. This phase separated microstructure is clearly evident in glasses quenched from melts above about 1000°C at rates faster than about 4°C/s. Mo-rich droplets separate from the matrix liquid when melts are cooled slower than about 300°C/s, and these droplets grow in size with slower quenches and longer isothermal heat-treatment times. The droplets crystallize to form two types of powellite, a Ca-rich form ($Ca_{1-x}Sr_xMoO_4$) and a Ba-rich form ($Ba_{1-x}Sr_xMoO_4$). Needle-shaped lanthanide-rich molybdate crystals form in samples isothermally held at 1100°C, along with the drop-shaped alkaline earth molybdate crystals.

Oxyapatite crystals form in melts continuously cooled slower than about 4°C/s, or isothermally held for several minutes at temperatures between 700 and 1100°C. The growth of the oxyapatite crystals is accompanied by the evolution of the microstructure of the residual glass from a droplet-in-matrix morphology to a more homogeneous appearance. In addition, alkaline earth powellite ($Ca_{1-x-y}Sr_xBa_yMoO_4$) crystals with cross-like morphologies form with the oxyapatite crystals, although it is unclear if the cross-like powellite precipitates from the residual glass or results from the transformation of pre-existing powellite droplets. The cross-like powellite crystals were present only in samples held isothermally from 900°C to 1100°C, and in the sample cooled most slowly, following the canister centerline cooling (CCC) protocol. From the isothermal experiments, crystallization was fastest at 1000°C, where crystalline powellite and oxyapatite could be detected after a one-minute isothermal hold.

The effects of microstructure on dissolution behavior were characterized using several short-term static dissolution tests. By using the Product Consistency Test (PCT), method A, the leach rates for Na, B, Ca, Mo, and Ba were found to all increase from samples with cooling rates that decreased from about 100°C/s to 0.1°C/s. These rates then decreased for the sample cooled most slowly (~0.008°C/s), following the CCC protocols. The Si leach rates did not change significantly from samples cooled at different rates, although it was lowest from the CCC sample. The Nd leach rates were lowest from all samples, remaining near the detection limit of the analytical system used.

The relative ion release rates indicate that the powellite phases dissolve most quickly from the glass-ceramic microstructures, followed by the residual glass phase, and then the oxyapatite phase. Topological analyses of corroded surfaces using electron microscopy, atomic force microscopy, and profilometry were consistent with the trends in ion release rates. Changes in the composition of the residual glass with the precipitation of the powellite and oxyapatite phases affect the dissolution rate of the residual glass. As the B_2O_3 concentration in the residual glass was fond to increase, the chemical durability of the glass decreased.

3.2. FUTURE WORK

The following paragraphs describe technical issues identified in this work that require further study to resolve.

1. The distributions of boron in the residual glass and any crystalline phases need to be determined. B_2O_3 is a significant (11.329 mole%) component of the starting glass but does not appear in be present in any of the major crystalline phases and could not be detected in the residual glass using the EDS systems available for this research. Li also could not be detected using the EDS system.
2. The lanthanide-rich molybdate needles detected in the high temperature (>1000°C) isothermal experiments need to be fully characterized. No specific diffraction data has been associated with these needles, and Raman spectra are inconsistent with the spectra collected from the other molybdate phases, despite the presence of significant concentrations of Mo from the EDS data. To study this phase, samples should be heat

treated again ~1100°C in a platinum crucible to determine whether this phase is caused by the stainless-steel tubes.

3. More isothermal heat treatments should be performed, I would recommend making more samples near the crystallization curves. This would narrow the times and temperatures that the phase transformations occur. I would also recommend performing some isothermal tests for long times, >24 hours, to try to produce samples with the maximum amount crystals as possible. These tests will also confirm if there are any additional slow growing crystals. Samples should also be melted at 1300 in the stainless-steel for longer times than 90 seconds and quenched to determine if there are changes from the baseline sample.
4. A more in-depth analysis of Raman spectroscopy paired with a more in-depth analysis on the residual glass composition. This may explain local charge densities around the Mo units by shifts in the vibrational frequencies. With an understanding of the composition, this would provide reasoning for the phase transformations.
5. More ion-release tests should be completed. I would recommend performing an ion-release test on an isothermal sample at high temperatures. Firstly, the needle molybdate phase found to be much different correlating to a much different residual glass that would have different dissolution properties. Secondly, because at high temperatures much larger phases form which may be easy to measure exact recession rates. Understanding, quantitative dissolution data would be very helpful in comparing data.
6. More tests will also need to be performed to clarify whether Mo is being leached from the powellite crystals or the residual glass. This could be done by making samples of the predicated residual glass and understanding the ion-release rates.

7. It would also be helpful to understand the dissolution rates as a function of pH. The pH changes in static leach tests. Understanding the effects of pH on dissolution is needed in the case that differing samples had very different post dissolution pH measurements.

APPENDIX A.

SUPPLEMENTAL DATA FOR PAPER I

Measured Cooling Profiles

The measured cooling profile for the constant cooling experiments, except the roller quench are shown in Figure A.1. The measured cooling profiles never reach 1300°C, the temperature at which the samples were melted. This is because the samples cooled fast when the crucibles were moved from the furnace to the mold with the thermocouples. The cooling profile of the air-cooled sample was not as linear as the other cooling profiles. The uneven cooling profile in the first 25 seconds of the air-cooled sample is due to movement of the thermocouple in the sample. Figure A.2 shows the comparison between the furnace program temperature and the measured temperature of a thermocouple held closely to the glass surface of the CCC sample. The temperature appears to have fully converged with the program temperature after 20 minutes and at ~1050°C. The sharp jumps in temperature near ~1 min are from transferring the sample from the melting furnace to the cooling furnace. The sharp jumps are not associated with the temperature of the sample, just the temperature of the thermocouple since the thermocouple was brought away from the sample in order to transfer through the furnace door.

Differential Thermal Analysis

Differential Thermal Analysis, DTA, (Perkin Elmer DTA 7) was used to determine the glass transition temperature and exothermic transitions that occur upon heating. Figure A.3 shows the glass transition temperature (T_g) occurring at 590°C and the onset temperature three exothermic reactions (T_{x1}, T_{x2}, T_{x3}) occurring at 710°C, 815°C, and 915°C.

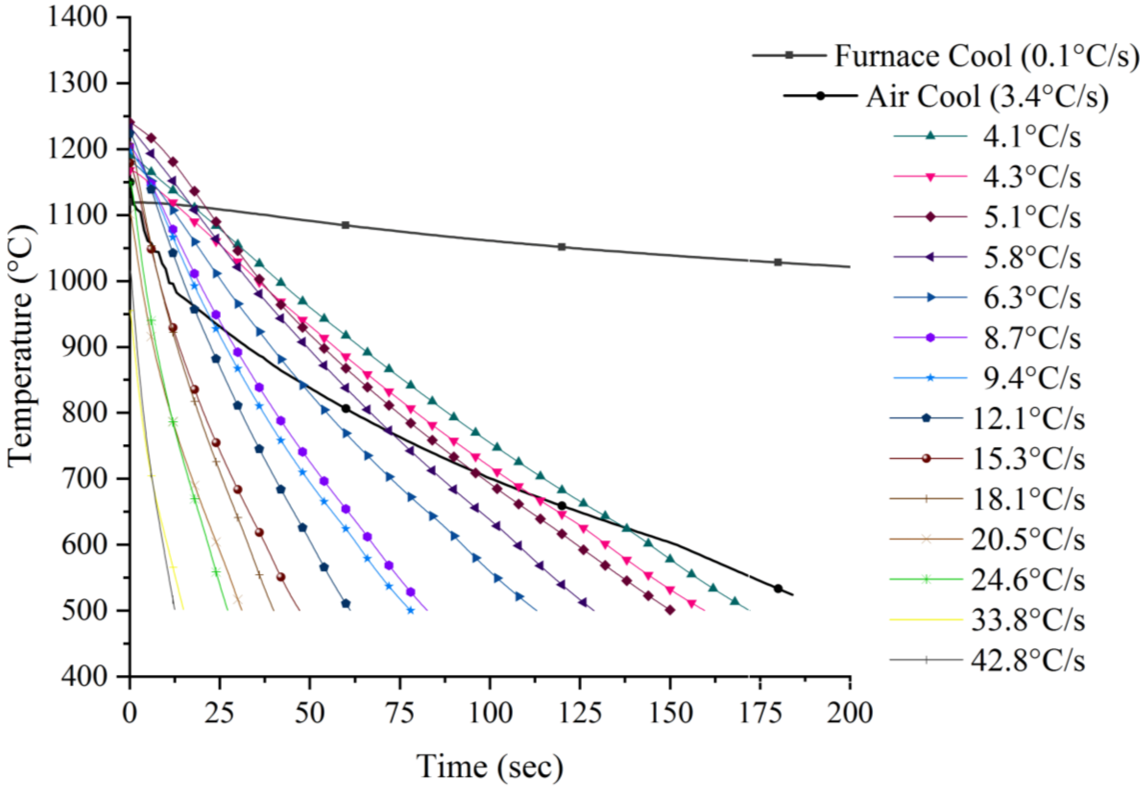

Figure A.1. Measured cooling profiles for the samples from the wedge mold, air cool, and furnace cool cooling methods.

X-ray Diffraction

Samples with fast quench rates (≥ 4.1°C/s) and short times in the isothermal experiments have a lone peak at 27.65° (2θ) making peak assignment difficult, Figure A.4. This peak is believed to be however associated with a molybdate phase instead of RuO_2 (the heavy metal crystal that do not dissolve in the glass). Additional shorter peaks at 29.58, 33.2, and 45.05° (2θ) align much closer with the molybdate phase (e.g., $Sr_{0.44}La_{0.39}(MoO_4)$, PDF# 04-002-4182) vs the RuO_2 phase (PDF# 00-040-1290) making this phase the assignment for the 27.65° (2θ).

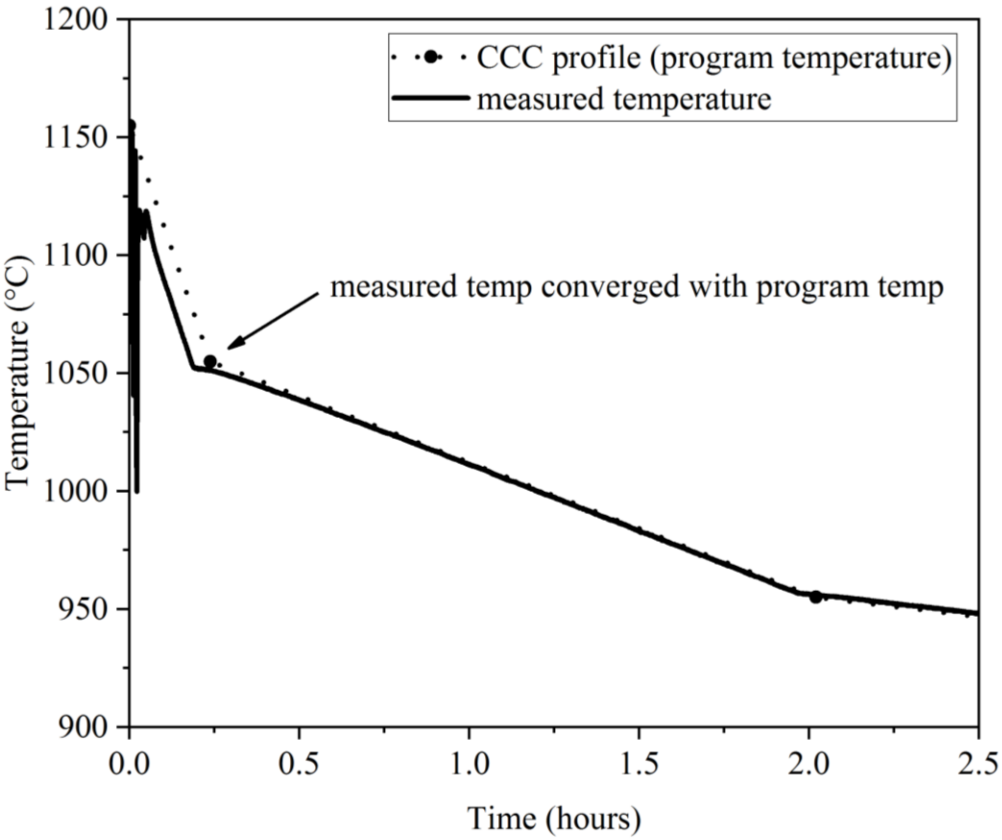

Figure A.2. Cooling profile comparison for the CCC sample between the (solid line) measured cooling profile from a thermocouple held above the sample and (dotted line) furnace program temperature set to follow the CCC profile.

The peak at 27.65° (2θ) also appears to grow in the isothermal samples heat treated at 600°C, also shown in Figure A.4. This peak could be associated with the Mo-rich droplets since the size of the Mo-rich droplets in the baseline sample was measured to be 0.07 ± 0.02 µm and measured to be 0.14 ± 0.03 µm after being held for 16 minutes at 600°C. The peak at 40.5° 2θ is believed to be due to contamination from melting the samples in stainless steel tubes.

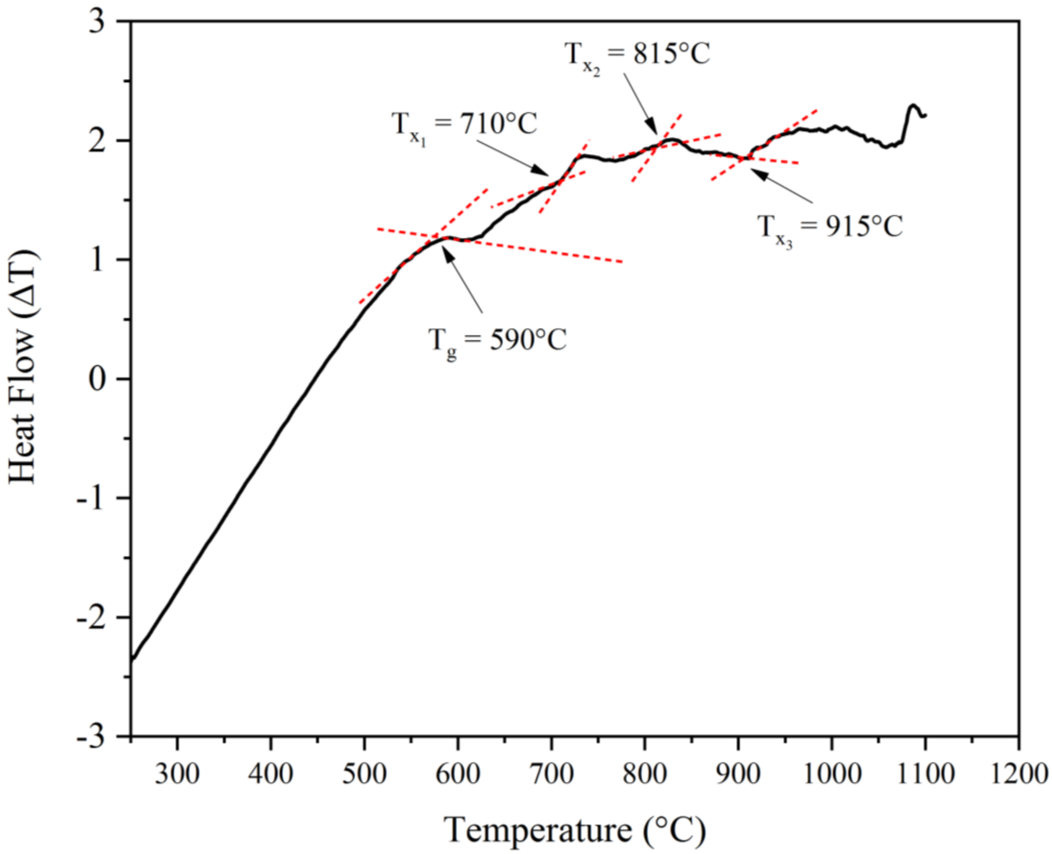

Figure A.3. DTA data collected of the as-received glass with labeled glass transitions (T_g) and onset of crystallization temperatures (T_x).

Tin Bath

Further tests were done to determine whether or not the microstructures were "reset" by only melting at 1300°C for 90 seconds in the isothermal experiments compared to 60 minutes in the continuous cooling experiments. XRD results of a quenched sample held at 1300°C for 90 seconds showed no additional peaks, actually showing less peaks than the as-received sample, Figure A.4. However, SEM did reveal that there Mo-rich droplets (Figure A.5) but image analysis determined the droplets to be smaller than the droplets in samples quenched at slower rates. There is a slight shift between the electron image and the molybdenum map in Figure A.5 due to surface charging from the electron beam. The droplets in the sample melted for 1300°C for 90 seconds and quenched at ~300°C/s were measured to be 0.07 ± 0.02 µm in diameter and a sample melted at 1300°C for 1 hour and quenched at 42.8°C/s was measured to be 0.17 ± 0.05 µm. The reduction in peaks from XRD and the smaller size Mo-rich droplets confirm that the microstructures in the samples quenched for 90 seconds at 1300°C were "reset".

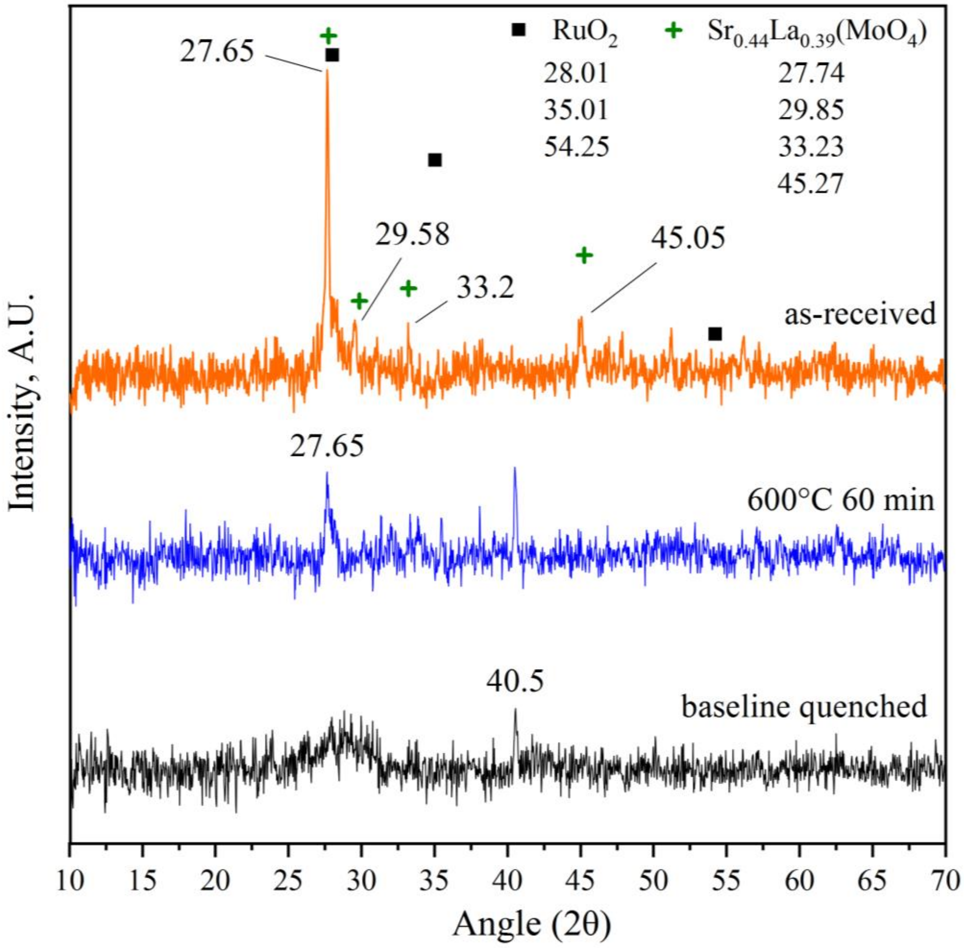

Figure A.4. XRD of the as-received glass, baseline sample, and sample heat treated at 600°C for 60 min with assements.

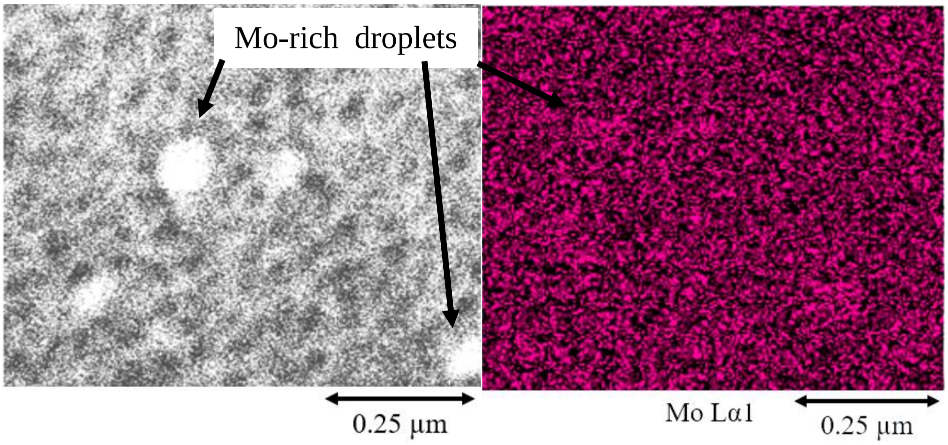

Figure A.5. SEM micrograph and molybdenum EDS maps for the baseline quenched (~300°C/s) sample.

It is believed that there was some contamination from the stainless-steel tubes since there is an extra peak in the XRD patterns from all the samples melted in stainless-steel verse samples melted in platinum. The small peak in the x-ray diffraction pattern at ~40.5 2Θ (Figure A.6) was found in all samples melted in stainless-steel and does not appear in the as-received or any samples from the continuously cooling experiments that melted in Pt crucibles. Although this phase does not correlate with XRD spectra from a used 304 stainless-steel tubes it could result from the stainless-steel species being in oxide form. Also, this contamination could be due to diffusion of Cr, Fe, and Ni into the glass. SEM EDS in the sample treated at 900°C for 24 hours, determined that these stainless-steel components diffused ~20 μm into the sample, Figure A.7.

With the use of three different tin baths, additional experiments were done to determine variability in the results. One noticeable difference between the tin baths was the fluctuations in temperature of the small tin bath upon quenching the stainless steel samples. Figure A.8 shows an example of the temperature fluctuation that occurred in the small volume tin bath (~250 cm^3) when a quench tube was immersed from the 1300°C melting furnace. The temperature initially increased by 15°C upon immersion, then decreased over the course of this 32-minute experiment. Over the entire experiment, the average temperature was 712°C, and this is the temperature reported for this experiment. The thermal fluctuations in the large volume tin baths were typically less than 1°C. To compare tin baths, samples were repeated using the same times and temperatures in each tin bath. Despite the different tin baths set-ups, the crystalline percentages of each sample were similar with only ~2 wt.% stdev, Table A.1. Variability in the Rietveld analysis and quantitative XRD procedures was also tested by running the same sample twice. Table A.2 shows the wt.% of oxyapatite and powellite detected in the air cooled sample run twice using the same XRD and Rietveld analysis. Figure A.9 shows an example of the matched patterns in the reitveld analysis in the sample isothermally heat treated at 900°C fro 24 hours. The subtracted background shows very little peaks proving the Reiveld analysis provides a good fit with the measured pattern. Table A.3 summarises the quantitative data from all the samples that contained crystals produced with the tin bath.

Composition Check

Samples from the continuous cooling experiment were sent to Jake Amoroso at Savanah River National Laboratories to measure the compositions after remelting in Pt at 1300°C for 60 min. Compositions were measured using ICP-AES and ICP-MS and are compared to the nominal composition. Cs was measured to be lower due to it volatilizing upon melting.

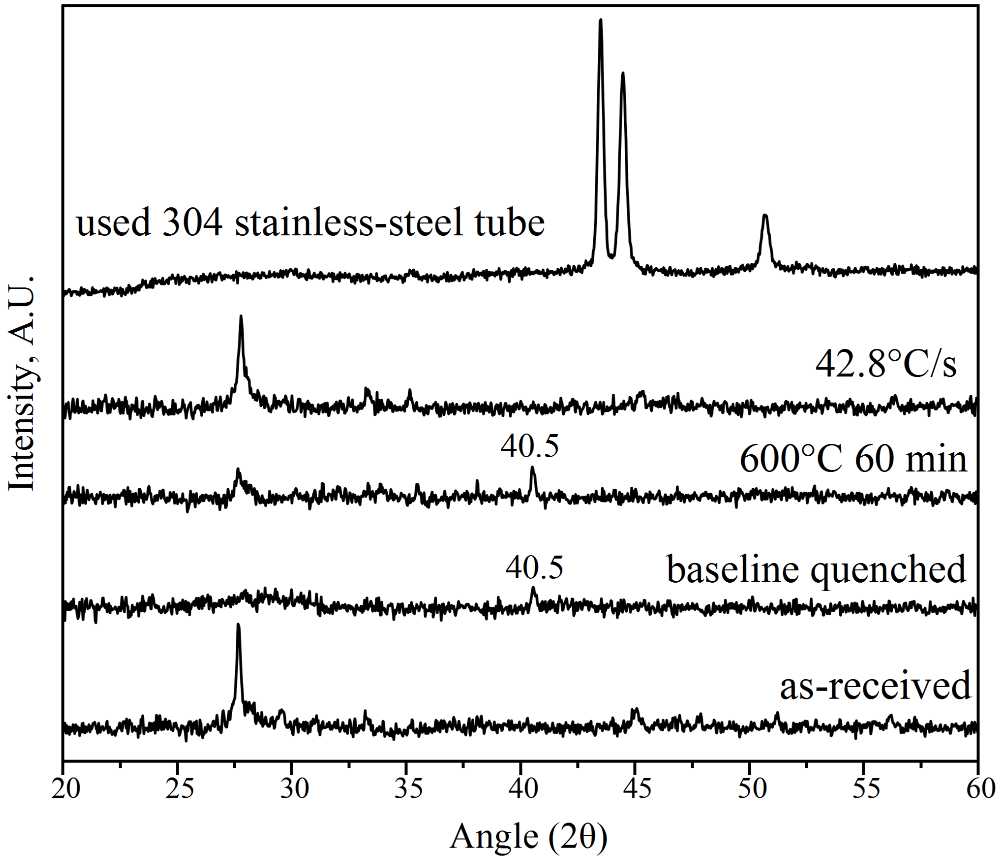

Figure A.6. XRD comparing the samples melted in stainles steel tubes, the baseline quenched sample and the sample heat treated at 600°C for 60 min, with the samples melted in Pt crucilbes, the as-received glass and sample cooled at 42.8°C/s. An XRD pattern from the used stainless steel tube is also shown for comparison.

Powellite Crystallization Kinetics

The crystal fraction, normalized to the crystal fraction in the sample heat treated at 900°C for 24 hours, was determined by quantitative XRD and is plotted vs time in Figure A13. The Johnson–Mehl–Avrami–Kolmogorov (JMAK) model described in Section 3.4.3. was again used to determine the crystallization kinetics of the powellite crystals within the glass. The average slope of the double log Avrami plot was determined to be 0.52 ± 0.08 Figure A.14. A slope of -17.2 ± 9.2 was determined for ln(k_n) vs 1000/T plot from which the activation energy was calculated to be 143.0 ± 76.8 kJ/mol, Figure A.15. Large error in the powellite activation energy correlates to the lower crystalline amounts, around the detection limits of the XRD and Rietveld analysis in most samples. The highest crystal percentage for powellite was measured to be only 6.7 wt.% by quantitative XRD for the isothermal samples. Also, there is a large increase in the size of powellite after the formation of oxyapatite further suggesting a change in mechanism for the growth of powellite with time. There also appears to be a change in growth mechanism with temperature due to the change in morphologies discussed in Paper I. Due to the lower crystal percentages and variations in growth mechanism the crystallization of powellite most likely cannot be described using the JMAK model.

TEM Diffraction Analysis

Fully indexed diffraction patterns of the 2 different zone axes of the Mo-rich droplets in the 4.1°C/s are shown in Figure A.16 and A.17. Figure A.18 compares the diffraction pattern with $Sr_{0.44}Ln_{0.39}(MoO_4)$ (blue), $Ba_{0.75}Sr_{0.25}(MoO_4)$ (green), and $CaMoO_4$ (red) which were assigned to the XRD patterns (Section 3.3.1.). The c/a lattice parameter ratios between the diffraction patterns are listed in Table A.4. These crystals all belong to the tetragonal crystal system (I 4_1/a space group). The deviations in the lattice parameters most likely correlate to differences in alkaline earth and LN amounts within the crystal.

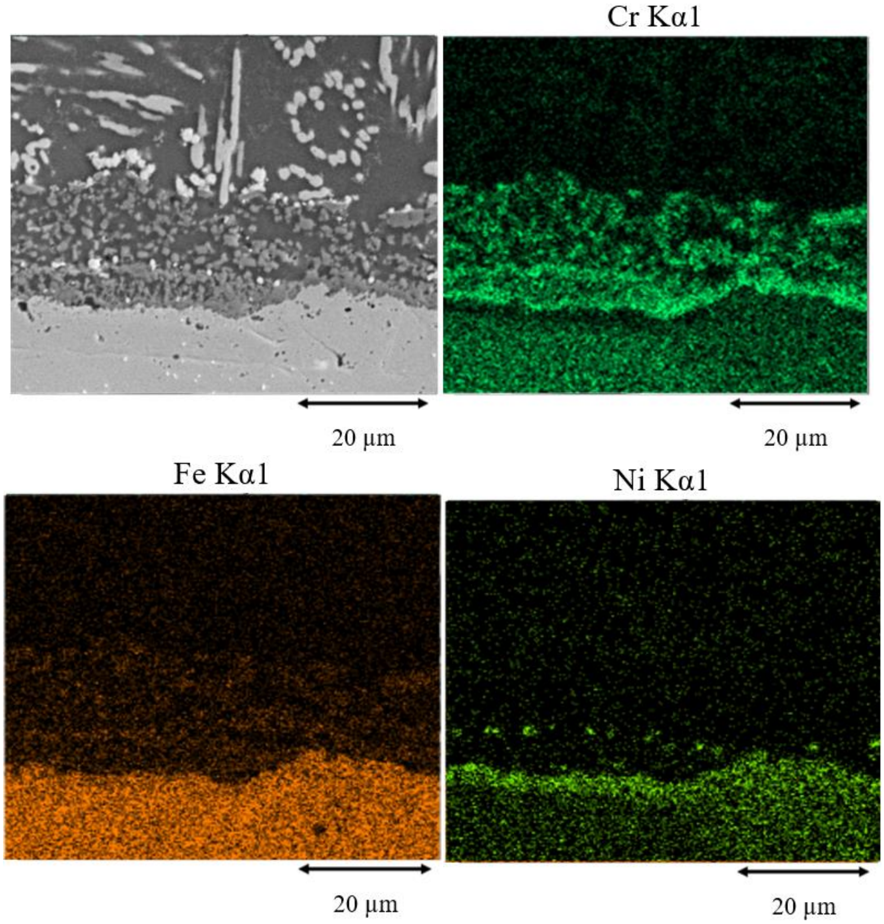

Figure A.7. SEM micrograph and EDS maps of the stainless steel diffusion into the glass in the sample heat treated at 900°C for 24 hours.

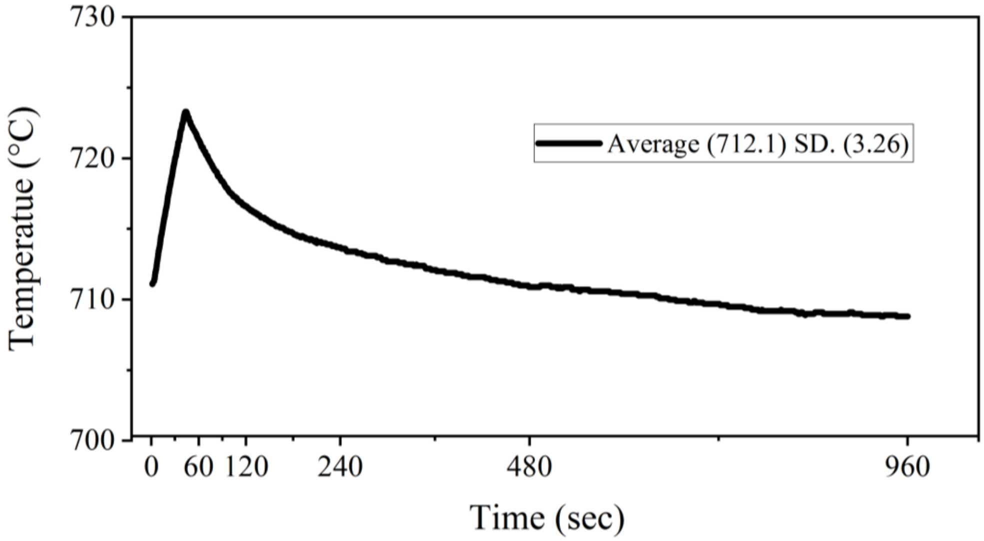

Figure A.8. Temperature-time profile during a quenching experiment in the low temperature tin bath.

Table A.1. Wt.% for oxyapatite and powellite for a sample held at ~800°C for 16 min in each tin bath.

Tin Bath	**Oxyapatite [wt.%]**	**Powellite [wt.%]**	**Total [wt.%]**
	800°C for 2 min		
Small	8.7	1.4	10.1
Kiln	2.0	0.0	2.0
Average	5.4	0.7	6.0
Std. Dev.	4.7	1.0	5.7
	800°C for 16 min		
Small	18.7	4.2	22.8
Kiln	19.2	0.9	20.1
Annealer	22.5	1.3	23.8
Average	20.1	2.1	22.2
Std. Dev.	2.1	1.8	1.9

Table A.2. Wt.% for oxyapatite and powellite in the air-cooled sample re-run twice with the XRD and Rietveld analysis.

Sample	**Oxyapatite [wt.%]**	**Powellite [wt.%]**	**Total [wt.%]**
Air cooled -1	9.3	1.5	10.8
Air cooled -2	7.5	0.9	8.4
Average	8.4	1.2	9.6
Std. Dev.	1.3	0.4	1.7
900°C 4 min -1	20.3	3.9	24.2
900°C 4 min -1	11.8	2.5	14.3
Average	16.1	3.2	19.3
Std. Dev.	6.0	1.0	7.00

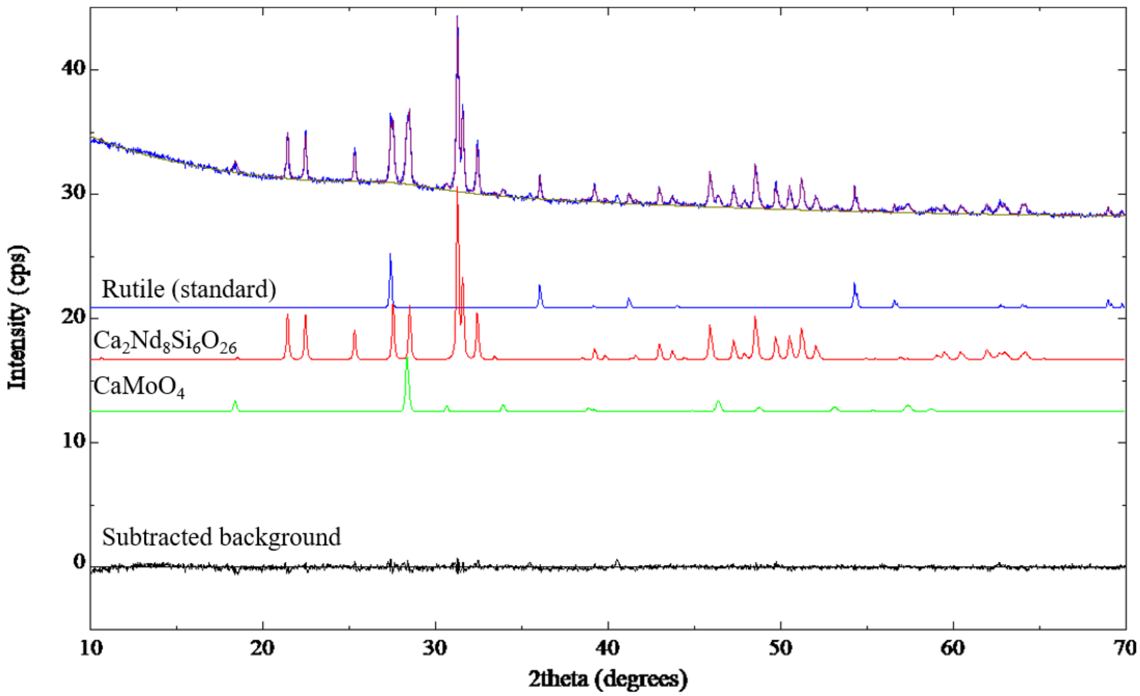

Figure A.9. Pattern matching and subtracted background from the Reitveld analysis.

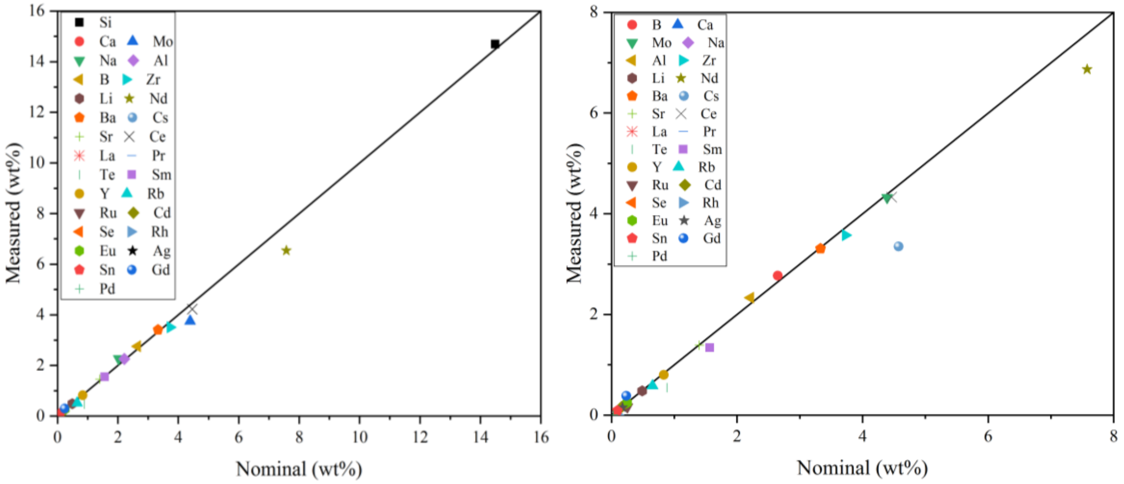

Figure A.10. Measured vs nominal composition of the roller quenched sample. Left) measured with ICP-AES and right) measured with ICP-MS

Table A.3. Quantitative XRD results.

Temperature (°C)	**Time (sec)**	**$Ca_2LN_8Si_6O_{26}$**	**Ca (MoO_4)**	**Amorphous Content**	**Crystal Content**
698.83	240	1.4	-	98.6	1.4
731.03	480	5.5	0.5	94.0	6.0
712.1	960	8.8	0.8	90.4	9.6
715.96	1920	12.2	1.2	86.6	13.4
698.83	3600	13.8	1.0	85.2	14.8
794.06	120	2.2	-	97.8	2.2
813.30	240	8.7	1.4	89.9	10.1
800	240	2.0	0.0	98.0	2.0
813.10	480	14.6	1.9	83.5	16.5
812.240	960	18.7	4.2	77.1	22.9
800	960	22.50	1.30	76.2	23.8
800	960	19.20	0.90	79.9	20.1
805.90	1920	20.6	4.1	75.3	24.7
794.28	3600	18.7	4.0	77.3	22.7
900	60	1.6	-	98.4	1.6
900	120	4.4	0.7	94.9	5.1
900	240	8.1	3.5	88.4	11.6
900	480	20.3	3.9	75.8	24.2
900	480	11.8	2.5	85.7	14.3
900	960	19.1	1.6	79.3	20.7
900	1920	24.3	5.5	70.2	29.8
900	3600	22.0	4.9	73.1	26.9
900	86400	28.5	6.7	64.8	35.2
1000	30	0.6	0	99.4	0.6
1000	60	4.3	0.6	95.1	4.9
1000	120	5.1	0.9	94.0	6.0
1000	240	13.9	2.9	83.2	16.8
1000	480	22.2	5.1	72.7	27.3
1000	960	22.8	5.5	71.7	28.3
1000	3600	25.9	3.9	70.2	29.8
1100	240	4.3	-	95.7	4.3
1100	480	7.6	-	92.4	7.6
1100	960	10.1	-	89.9	10.1
1100	1920	11.3	-	88.7	11.3
1100	3600	10.6	-	89.4	10.6

Sample	**Cooling rate [°C/s]**	**$Ca_2LN_8Si_6O_{26}$**	**Ca (MoO_4)**	**Amorphous Content**	**Crystal Content**
Air cooled	3.5	7.5	0.9	91.6	8.4
Furnace Cooled	0.1	21.4	3.2	75.4	24.6
CCC	0.005	15.2	8.5	76.3	23.7

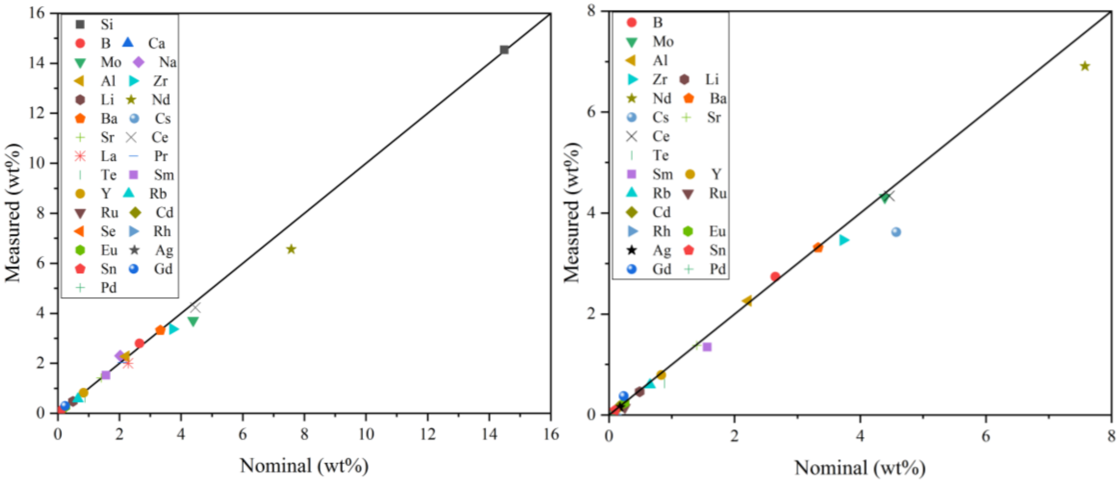

Figure A.11. Measured vs nominal composition of the 0.1°C/s sample. Left) measured with ICP-AES and right) measured with ICP-MS

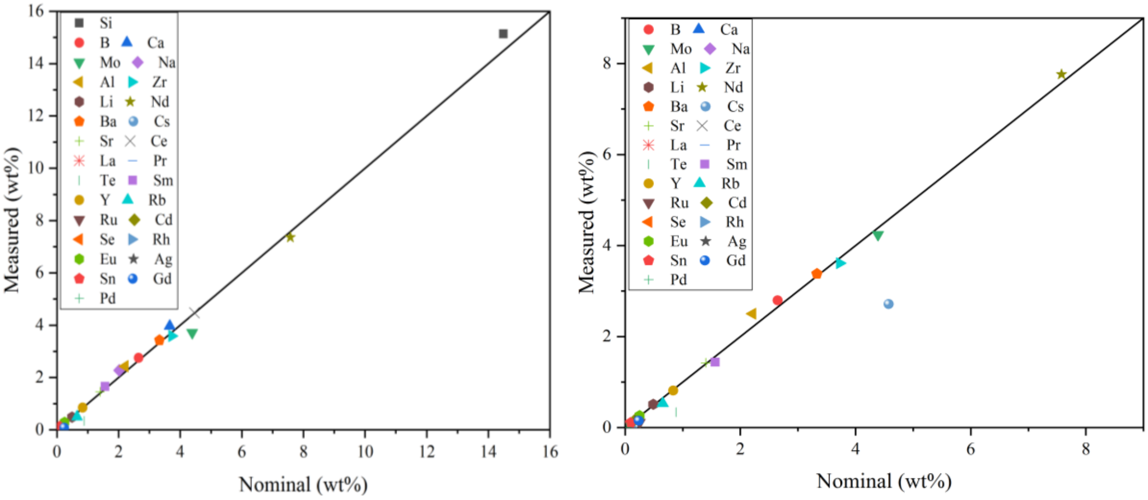

Figure A.12. Measured vs nominal composition of the CCC sample. Left) measured with ICP-AES and right) measured with ICP-MS

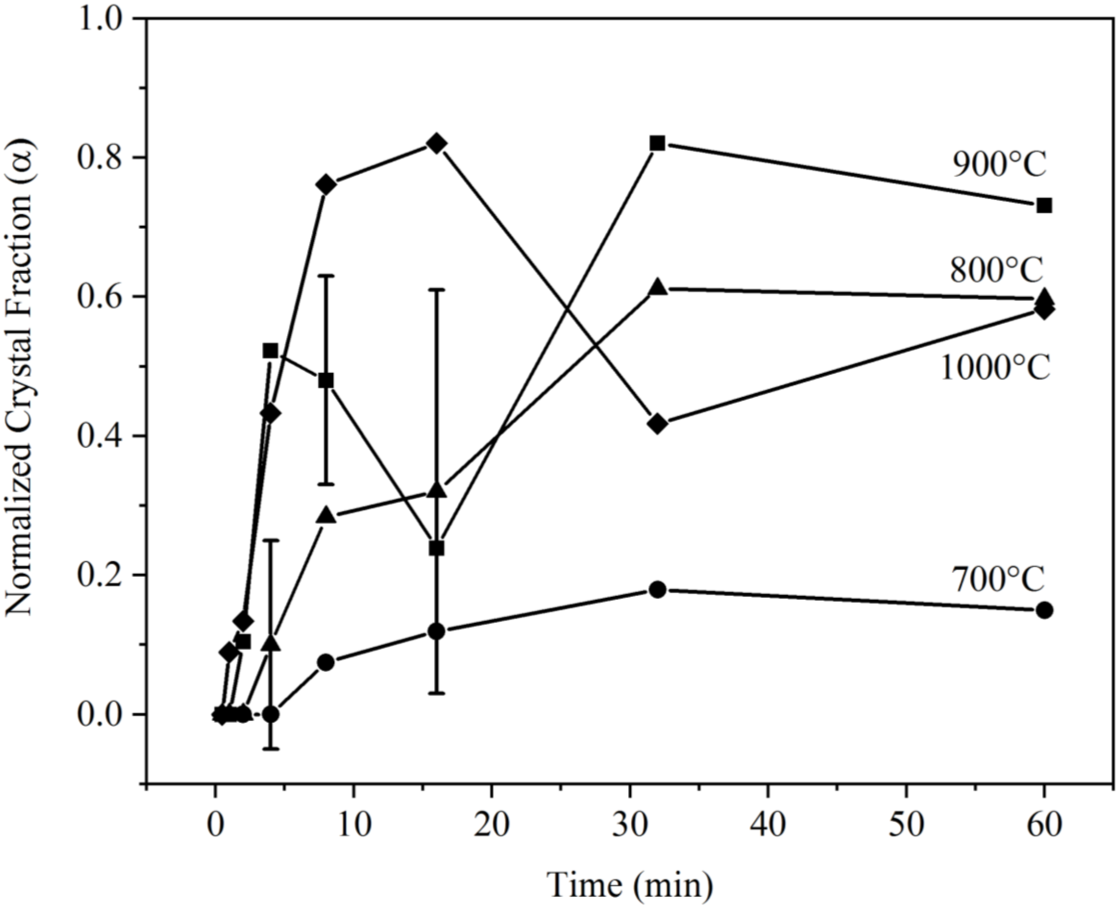

Figure A.13. Normalized crystal fraction vs time for powellite determined by XRD.

Table A.4. Measured composition of the furnace cool, CCC, and roller quench samples from Savanah River National Laboratories.

	Furnace Cool (0.1°C/s)		CCC (0.05°C/s)		Roller Quench (>100°C/s)	
	ICP-AES	ICP-MS	ICP-AES	ICP-MS	ICP-AES	ICP-MS
Si	14.54		15.14		14.69	
B	2.80	2.74	2.75	2.80	2.76	2.77
Ca	6.14		3.97		6.28	
Mo	3.72	4.31	3.71	4.24	3.75	4.32
Na	2.31		2.27		2.27	
Al	2.28	2.26	2.43	2.50	2.25	2.33
Zr	3.37	3.46	3.59	3.61	3.51	3.58
Li	0.48	0.46	0.48	0.51	0.49	0.48
Nd	6.56	6.91	7.36	7.76	6.54	6.87
Ba	3.32	3.32	3.43	3.38	3.41	3.31
Cs		3.62		2.71		3.35
Sr	1.42	1.38	1.45	1.42	1.46	1.39
Ce	4.23	4.34	4.47	4.65	4.22	4.33
La	2.00	1.99	2.10	2.08	2.04	1.98
	2.04	2.08	2.12	2.13	2.08	2.09
Te	0.61	0.62	0.34	0.34	0.47	0.55
Sm	1.52	1.35	1.66	1.44	1.56	1.34
Y	0.82	0.79	0.84	0.82	0.82	0.80
Rb	0.58	0.60	0.50	0.53	0.52	0.58
Ru		0.15		0.11		0.17
Cd	0.16	0.17	0.16	0.16	0.16	0.17
Se						
Rh		0.00		0.00		0.00
Eu	0.27	0.24	0.29	0.26	0.27	0.25
Ag		0.15		0.15		0.15
Sn	0.11	0.09	0.12	0.11	0.10	0.09
Gd	0.30	0.37	0.08	0.15	0.29	0.38
Pd		0.01		0.01		0.01

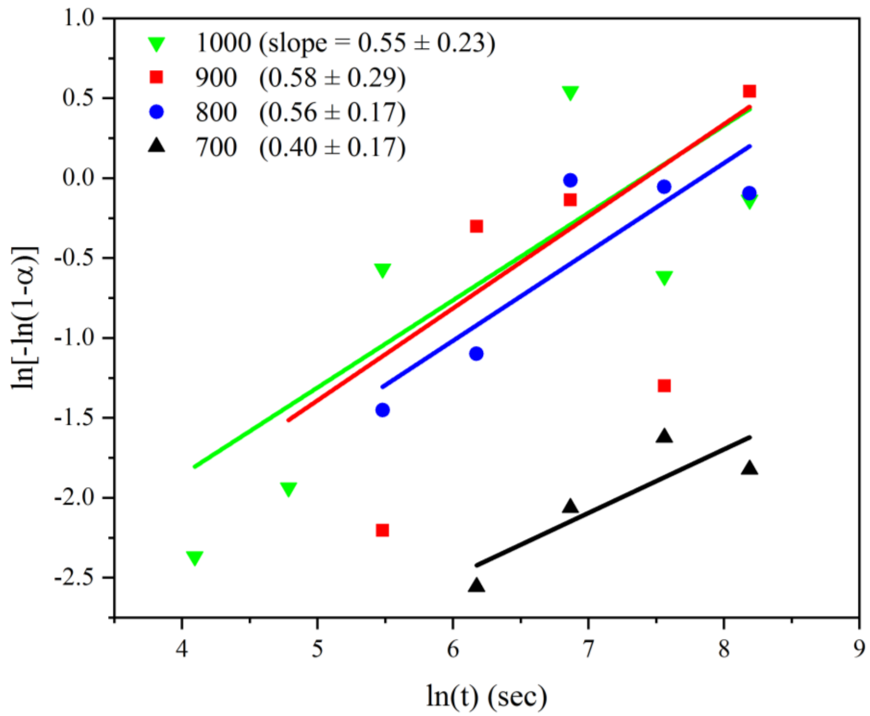

Figure A.14. Avrami plot for powellite formation in the isothermal experiments ln(k_n) vs 1000/T for powellite formation in the isothermal experiments.

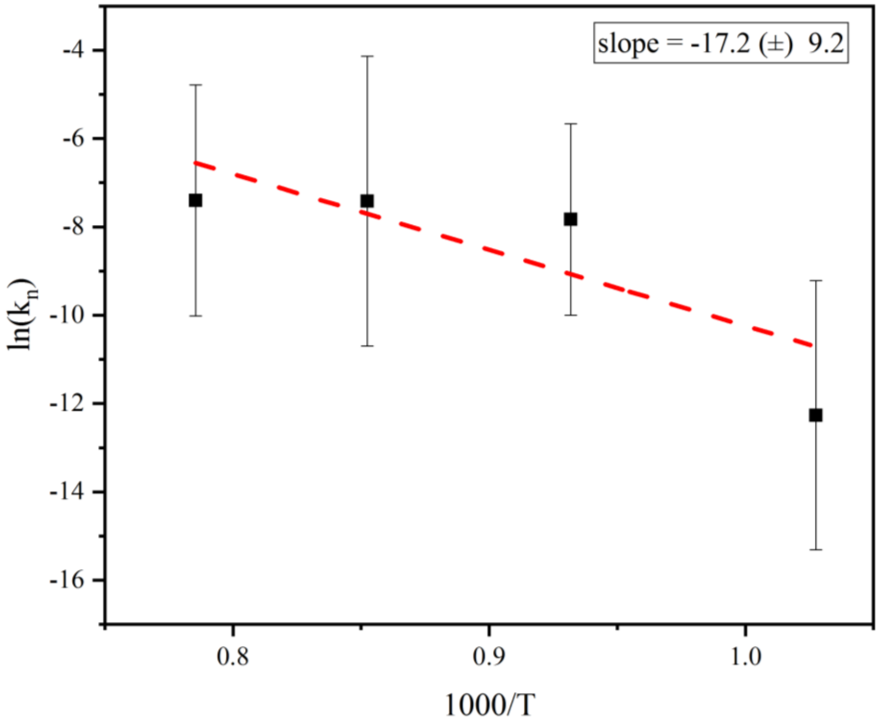

Figure A.15. ln(k_n) vs 1000/T for powellite formation in the isothermal experiments.

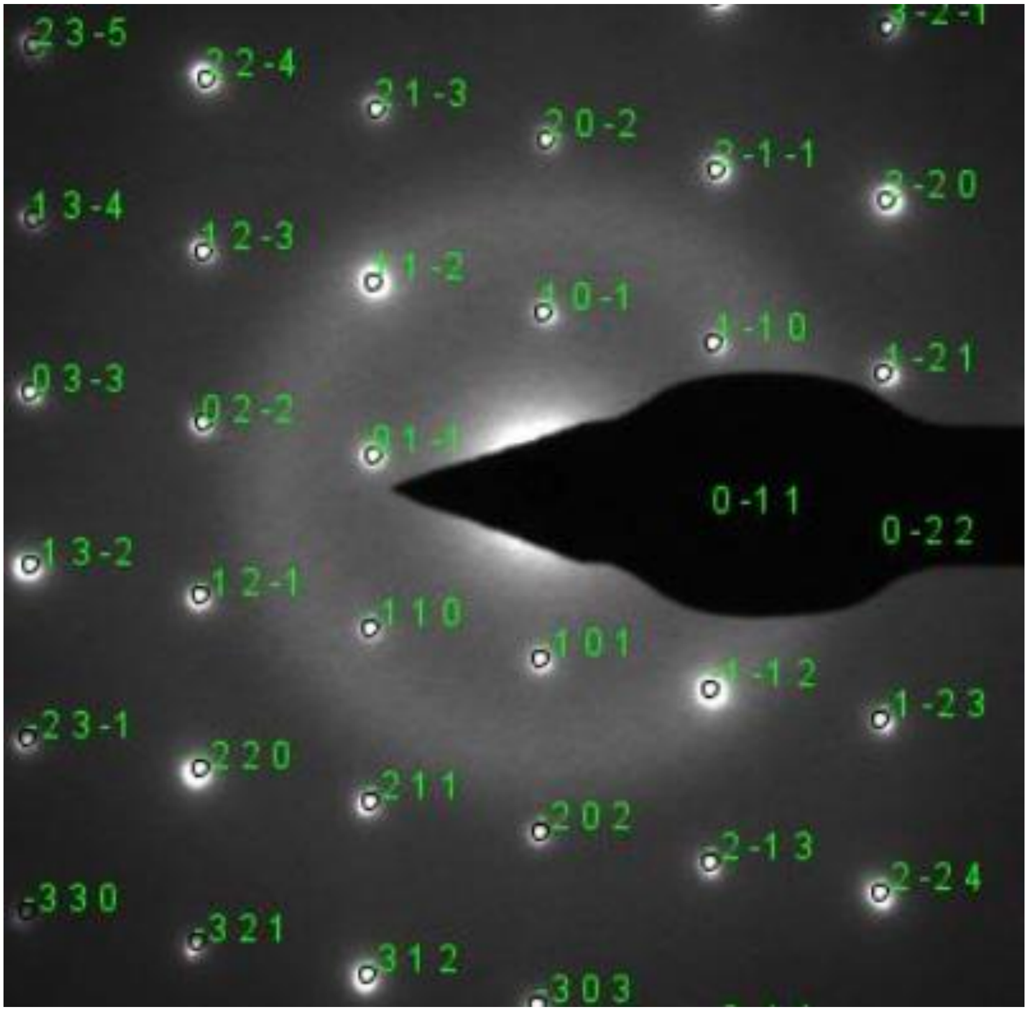

Figure A.16. Fully indexed SAD pattern from the Mo-rich droplet in the 4.1°C/s sample along zone 1

Table A.5. Comparison of the lattice parameters (c/a) for the various crystal.

$Sr_{0.44}Ln_{0.39}(MoO_4)$ (c/a)	$Ba_{0.75}Sr_{0.25}(MoO_4)$ (c/a)	$CaMoO_4$ (c/a)	Measured (c/a)
2.22	2.28	2.20	2.26 ± 0.01

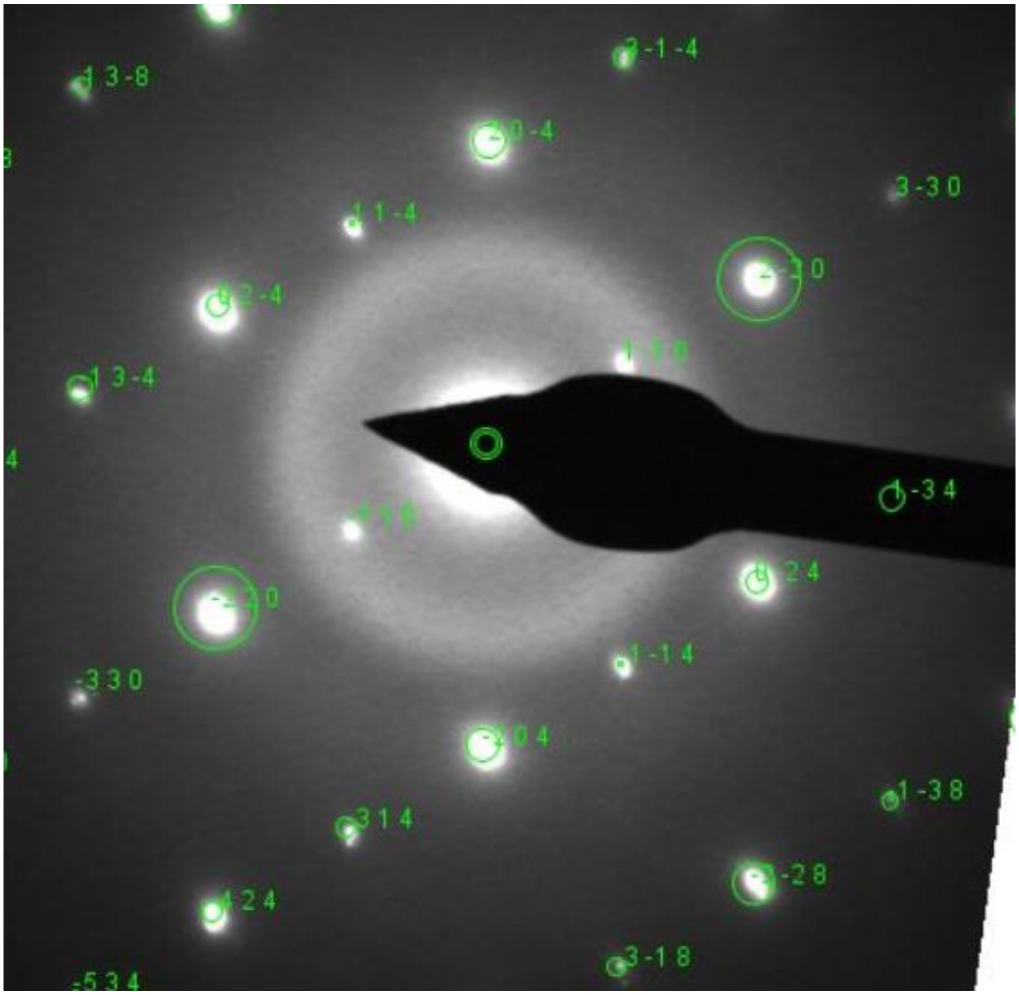

Figure A.17. Fully indexed SAD pattern from the Mo-rich droplet in the 4.1°C/s sample along zone 2

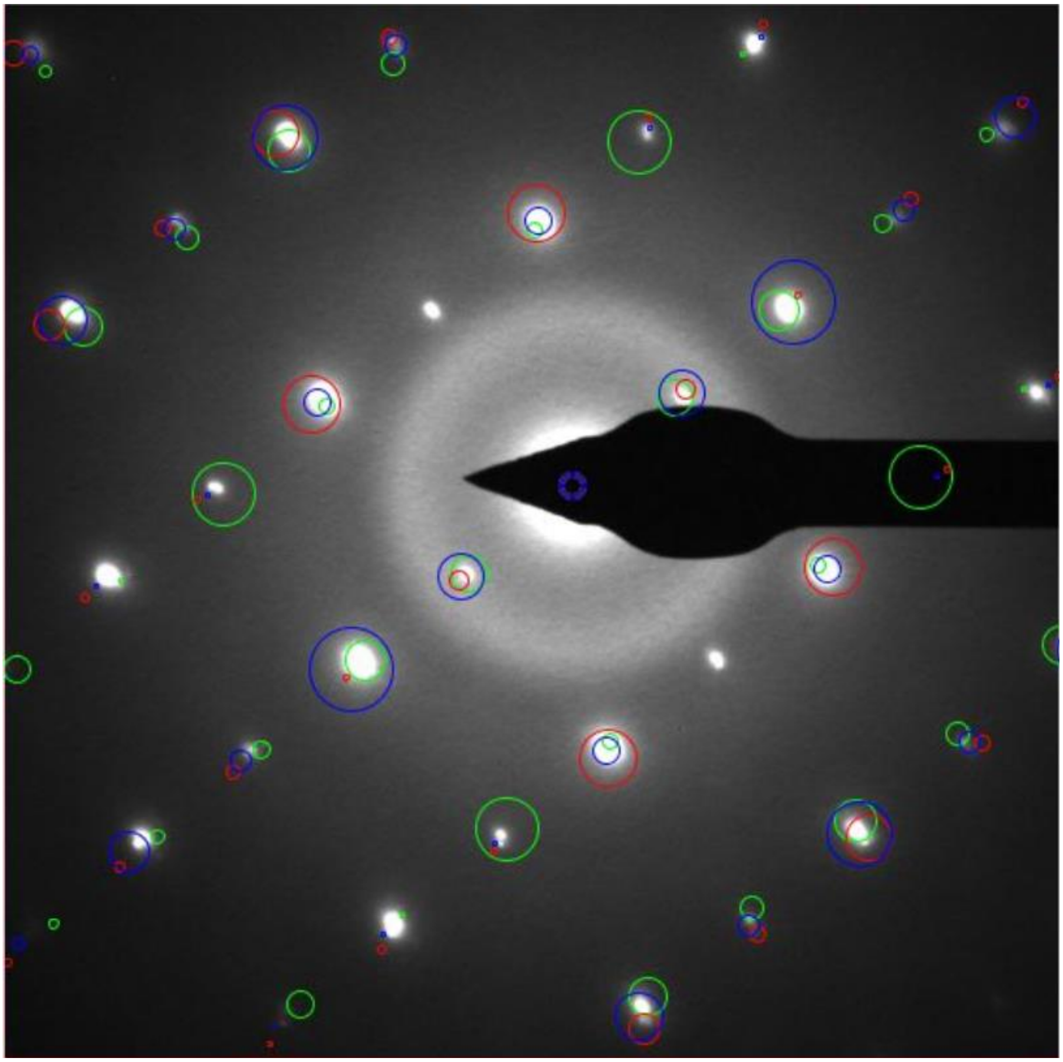

Figure A.18. Comparison to with $Sr_{0.44}Ln_{0.39}(MoO_4)$ (blue), $Ba_{0.75}Sr_{0.25}(MoO_4)$ (green), and $CaMoO_4$ (red) diffraction patterns.

APPENDIX B.

SUPPLEMENTAL DATA FOR PAPER II

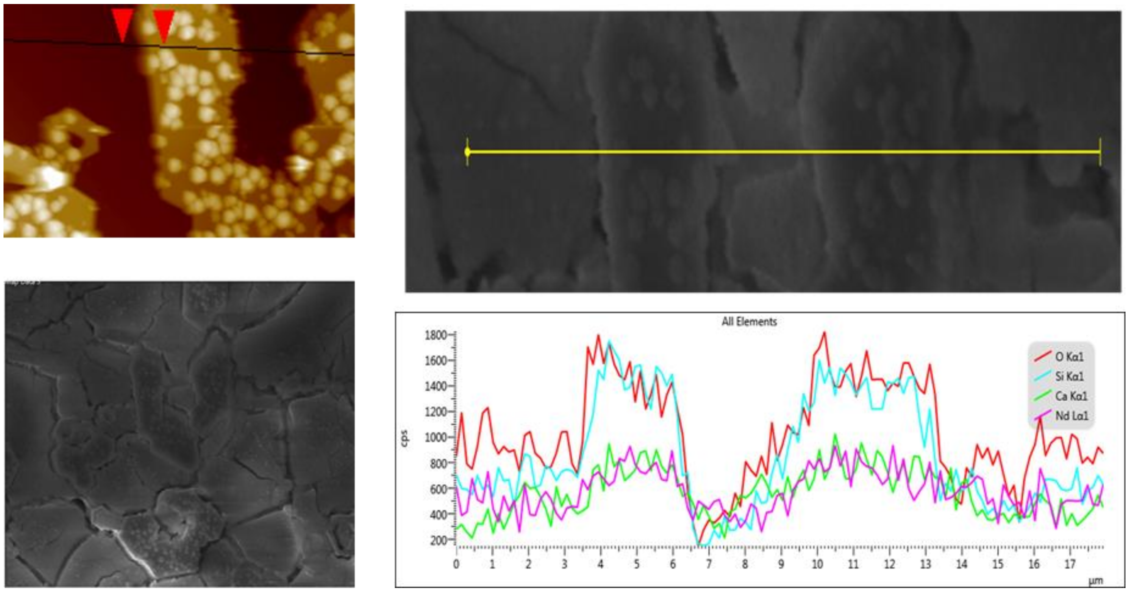

Figure B.1. Air cooled sample SEM micrographs and EDS line scan of the same area scanned with the AFM.

Table B.1. Normalized release rates for PCT dissolution experiments also including results reported by Crum et al. [16].

	Roller Quench [g/m^2]	**Air Cool [g/m^2]**	**Furnace Cool [g/m^2]**	**CCC [g/m^2]**	**Crum et al. [16] CCC [g/m^2]**
B	0.73 ± 0.03	0.99 ± 0.11	1.35 ± 0.19	0.93 ± 0.13	0.179
Ca	0.53 ± 0.02	0.52 ± 0.01	0.68 ± 0.07	0.19 ± 0.05	0.032
Na	1.42 ± 0.14	1.37 ± 0.03	1.80 ± 0.22	0.80 ± 0.12	0.172
Nd	-	-	0.01	-	NR*
Mo	0.47 ± 0.02	1.29 ± 0.01	1.93 ± 0.15	0.31 ± 0.11	0.172
Ba	0.03 ± 0.01	0.24 ± 0.02	0.50 ± 0.03	0.07 ± 0.01	0.070
Si	0.49 ± 0.03	0.42 ± 0.01	0.49 ± 0.03	0.25 ± 0.02	0.051

* NR – value is not reported

Table B.2. Normalized release rates for PCT dissolution experiments from Savanah River National Laboratories [16].

Sample	**Furnace Cool (0.1°C/s) [g/m^2]**	**CCC (0.05°C/s) [g/m^2]**	**Roller Quench (>100°C/s) [g/m^2]**
Si	1.01E-01	8.03E-02	1.05E-01
B	3.04E-01	1.97E-01	1.30E-01
Ca	6.36E-02	4.14E-02	3.86E-02
Mo	3.42E-01	6.51E-02	4.97E-02
Na	1.68E+00	1.47E+00	1.51E+00
Al	1.88E-02	3.19E-02	3.77E-02
Zr	7.80E-05	8.44E-04	1.10E-04
Li	4.68E-01	2.25E-01	2.32E-01
Nd	7.80E-05	4.25E-04	6.90E-05
Ba	7.50E-02	1.36E-02	8.30E-03
Cs	2.68E-01	1.14E-01	1.60E-01
Sr	1.15E-01	3.66E-02	3.43E-02
Ce	7.60E-05	4.41E-04	7.50E-05
La	7.60E-05	5.27E-04	5.90E-05
Pr	7.30E-05	4.29E-04	6.00E-05
Te	6.15E-02	7.32E-03	3.81E-03
Sm	8.30E-05	3.93E-04	6.60E-05
Y	8.20E-05	4.67E-04	6.40E-05
Rb	2.61E-01	1.12E-01	1.37E-01
Ru	4.46E-04	4.60E-04	2.46E-04
Cd	4.00E-03	1.75E-03	6.72E-04
Se	<1.049325	<1.056108	<1.055529
Rh	2.39E-02	1.17E-02	1.69E-02
Eu	4.27E-04	4.93E-04	4.25E-04
Ag	1.52E-03	2.88E-03	2.74E-04

Table B.3. Δh measurements for profilometry and AFM test.

device	Sample	Cooling Rate [°C/s]	Time [days]	Δh [nm]	St. dev.
profiler	copper step 2	5.8	7	59	19
	copper step 1	5.1	7	91	19
	steel step 1	4.1	7	130	26
	air cool	3.4	1	56	17
	air cool	3.4	2	49	13
	air cool	3.4	7	148	30
	furnace cool	0.1	2	58	12
	furnace cool	0.1	3	67	15
	furnace cool	0.1	4	115	24
	furnace cool	0.1	4	106	11
	furnace cool	0.1	7	201	31
	furnace cool	0.1	7	195	24
	furnace cool	0.1	7	195	34
	furnace cool	0.1	8	245.2	29
	CCC	0.008	7	841	181
	CCC	0.008	7	714	174
AFM	air cool (oxyapatite – glass)	3.4	12.5	243	90
	air cool	3.4	12.5	264	68
	air cool	3.4	18.75	378	181

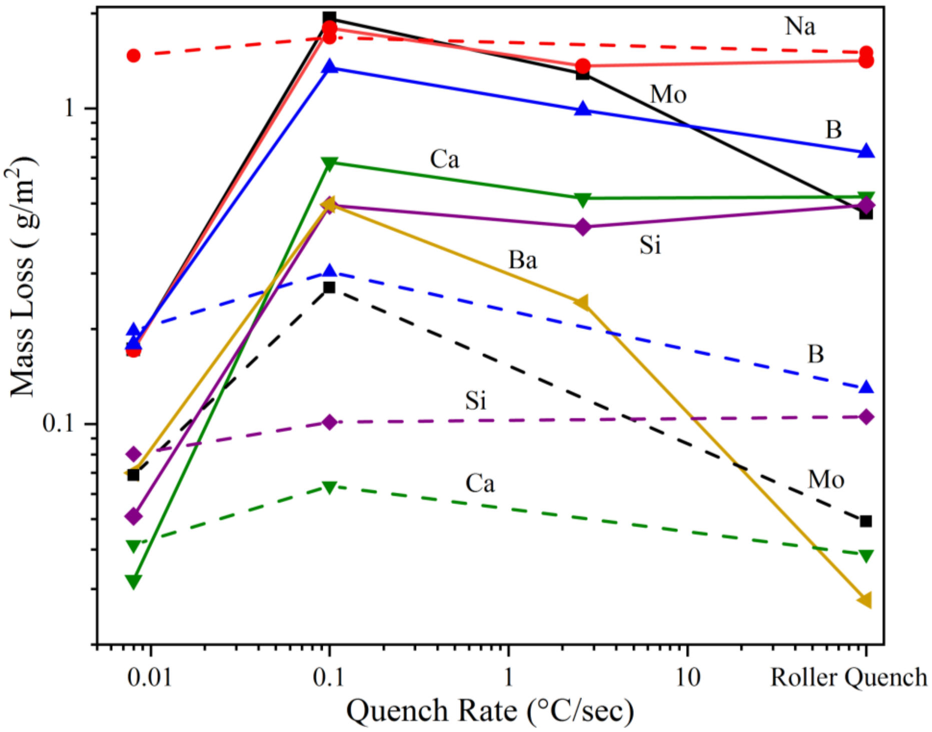

Figure B.2. PCT results vs quench rates coming this study (solid lines) and results from Savanah River National Laboratories (dotted line).

Table B.4. Mass loss measurements normalized to surface area.

Sample	**Cooling Rate [°C/s]**	**Time [days]**	**Weight loss [g/m^2]**
copper step 2	5.8	7	1.7
copper step 1	5.1	7	2.1
steel step 1	4.1	7	2.9
air cool	3.4	1	1.1
air cool	3.4	2	3.1
air cool	3.4	4	1.8
air cool	3.4	7	4.1
furnace cool	0.1	1	3.6
furnace cool	0.1	2	2.0
furnace cool	0.1	2	4.7
furnace cool	0.1	3	2.9
furnace cool	0.1	4	6.6
furnace cool	0.1	7	7.0
furnace cool	0.1	7	5.4
furnace cool	0.1	7	3.9
furnace cool	0.1	8	7.7
CCC	0.008	7	2.7
CCC	0.008	7	3.6

BIBLIOGRAPHY

[1] M. L. F. Nascimento, "Brief history of X-ray tube patents," *World Patent Information.*, **37** 48-53 (2014).

[2] P. Radvanyi and J. Villain, "The discovery of radioactivity," *Comptes Rendus Physique.*,**18** 544-550 (2017).

[3] S. T. Brewer, "The First Reactor," U.S. Department of Energy, Washington, D.C., (1982).

[4] M. I. Ojovan and W. E. Lee, "An Introduction to Nuclear Waste Immobilization, 2 ed.," *Elsevier Science*, (2013).

[5] "Code of Federal Regulations, Title 40 - Protection of Environment, Part 261 - Identification and Listing of Hazadous Waste," E. P. Agency, (2017).

[6] "Code of Federal Regulations, Title 10 - Energy, Part 961 - Standard Contract for Disposal of Spent Nuclear Fuel andor High-Level Radioactive Waste," D. O. E., (2012).

[7] "Waste Acceptance Product Specifications (WAPS) For Vitrified High-Level Waste Forms," *DOE/EM-0093 Revision 3*, (2012).

[8] "Classification of Radioactive Waste, Genera Safty Guide," International Atomic Energy Agency, (2009).

[9] W. J. Weber, A. Navrotsky, S. Stefanovsky, E. R. Vance, and E. Vernaz, "Materials Science of High-Level Nuclear Waste Immobilization," *MRS Bulletin*, **34** 46-53 (2011).

[10] D. Sassani, L. Price, R. Rechard, R. Rogers, W. Walkow, A. Johnson, *et al.*, "Inventory and Waste Characterization Status Report," Sandia National Laboratories, Albuquerque, NM, (2017).

[11] "Evaluation of Options for Permanent Geologic Disposal of Used Nuclear Fuel and High-Level Radioactive Waste Inventory in Support of a Comprehensive National Nuclear Fuel Cycle Strategy," Sandia National Laboratories, Albuquerque, NM, (2014).

[12] T. A. Todd, and J. D. Vienna, "Separation and waste forms campaign implementation plan" FCRD-SWF-2012-00123, (2012).

[13] J. V. Crum, A. L. Billings, B. J. Lang, J. C. Marra, C. P. Rodriguez, J. V. Ryan, *et al.*, "Baseline Glass Development for Combined Fission Products Waste Streams," Pacific Northwest National Laboratory, Richland, WA, (2009).

[14] M. Magnin, S. Schuller, D. Caurant, O. Maje´rus, D. de Ligny, and C. Mercier, "Effect of compositional changes on the structure and crystallization tendency of a borosilicate glass containing MoO_3," *Ceram Trans*, **207** 59–68 (2009).

[15] J. V. Crum, J. J. Neeway, B. J. Riley, Z. Zhu, M. J. Olszta, and M. Tang, "Dilute condition corrosion behavior of glass-ceramic waste form," *Journal of Nuclear Materials,* **482** 1-11 (2016).

[16] J. V. Crum, L. Turo, B. Riley, M. Tang, A. Kossoy, and C. Jantzen, "Multi-Phase Glass-Ceramics as a Waste Form for Combined Fission Products: Alkalis, Alkaline Earths, Lanthanides, and Transition Metals," *Journal of the American Ceramic Society*, **95** 1297-1303 (2012).

[17] A. K. Varshneya, "Fundamentals of Inorganic Glasses". *Academic Press Inc.*, San Diego, CA, 27-60, 282 (1994).

[18] W. H. Zachariasen, "The Atomic Arrangement in Glass," *Journal of the American Chemical Society of Chemistry,* **54** 3841-3851 (1932).

[19] K. Sun, "Fundamental Condition of Glass Formation," *Journal of the American Ceramic Society*, **30** 277-281 (1847).

[20] D. A. Pierce, P. Hrma, J. Marcial, B. J. Riley, and M. J. Schweiger, “Effect of alumina source on ease of melting of glass batch,” Pacific Northwest National Laboratory, Richland, WA, (2012).

[21] A. Quintas, D. Caurant, O. Majérus, T Charpentier, and J. L. Dussossoy, "Effect of the nature of alkali and alkaline-earth oxides on the structure and crystallization of an aluminoborosilicate glass developed to immobilize highly concentrated nuclear waste solutions," Montpellier, France, (2009).

[22] L. A. Chick, G. F. Piepel, G. B. Mellinger, R. P. May, W. J. Gray, and C. Q. Buckwalter, "Effects of composition on properties in an 11-component nuclear waste glass system" Pacific Northwest National Laboratory, Richland, WA, (1981).

[23] I. S. Gutzow and J. W. P. Schmelzer, "The Vitreous State, second ed." *Berin Heidelberg: Springer-Verlag*, 219 -365 (2013).

[24] A.L. Billings T.B. Edwards, "Time - Temperature - Transformation (TTT) Diagrams for Future Waste Compositions," Savannah River National Laboratory, Aiken, SC, (2010).

[25] J.V. Crum, G.F. Piepel, C.C. Bonham, J.L. Mayer, J.J. Neeway, R.M. Asmussen, B.P. McCarthy, C.P. Rodriguez, C.L. Crawford and J.C. Marra. "Glass-Ceramic Matrix Study" U.S. Department of Energy Office of Nuclear Energy, Nuclear Technology Research & Development, Materials Recovery and Waste Forms Development Campaign, NTRD-MRWFD-2017-000418 (2017).

[26] E. I. Peterson, T. P. Sanders, J. Smith, R. J. O’Malley, "Investigation of Mold Flux Crystallization by Rapid Quenching and Isothermal Aging in Molten Tin," *AISTech,* Nashville, TN, (2017).

[27] M. Avrami, "Kinetics of Phase Change: I, General Theory," *J. Chem. Phys.,* **7** 1103–12 (1939).

[28] M. Avrami, "Kinetics of Phase Change: II, Transformation-Time Relations for Random Distribution for Nuclei," *J. Chem. Phys.,* **8** 212-24 (1940).

[29] M. Avrami, "Kinetics of Phase Change: III, Granulation, Phase Change, and Microstructure," *J. Chem. Phys.,* **9** 177-84 (1941).

[30] W. A. Johnson and R. F. Mehl, "Reaction Kinetics in Processes of Nucleation and Growth," *Trans. Am. Inst. Min. Metall. Pet. Eng.,* **135** 416-458 (1939).

[31] A. N. Kolmogorov, "A Statistical Theory for the Recrystallization of Metals," *Izv. Akad. Nauk USSR, Ser. Mathem.,* **1** (1937).

[32] J. Malek, "Kinetic analysis of crystallization processes in amorhpous materials," *Thermochinica Acta* **355** 239-253 (2000).

[33] A. Paul, "Chemical durability of glasses; a thermodynamic approach," *Journal of Materials Science* **12** 2246-2268 (1977).

[34] S. Gin, A. Abdelouas, L. J. Criscenti, W. L. Ebert, K. Ferrand, T. Geisler, M. T. Harrison, Y. Inagaki, S. Mitsui, K. T. Mueller, J. C. Marra, C. G. Pantano, E. M. Pierce, J. V. Ryan, J. M. Schofield, C. I. Steefel, and J. D. Vienna, “An international initiative on long-term behavior of high-level nuclear waste glass,” *materials today* **16** [6] 243-248 (2013).

[35] "Standard Test Methods for Determining Chemical Durability of Nuclear, Hazardous, and Mixed Waste Glasses and Multiphase Glass Ceramics: The Product Consistency Test (PCT)," *American Society for Testing and Materials International,* C1285-14 (2008).

[36] "Environmental Assessment-Waste Form Selection for SRP High-Level Waste" USDOE Report DOE/EA 0179, Washington, DC. (1982).

[37] C. M. Jantzen, N. E. Bibler, and D. C. Beam, "Characterization of the Defence Waste Processing Facility (DWPF) Environmenental Assessment (EA) Glass Standard Reference Material (U)" WSRC-TR--92-346, Westinghouse Savannah River, SC, (1992).

[38] J. H. Hsu, J. Bai, C. W. Kim, R. K. Brow, J. Szabo, A. Zervos, "The effect of crystallization and residual glass of the chemical durability of iron phosphate waste forms contaning 40 wt% of a high MoO_3 Collins CLT waste," *Journal of Nuclear Materials* **500** 373-380 (2018).

[39] D. Gombert, S. Piet, T. Trickel, J. Carter, J. Vienna, and B. Ebert, "Combined Waste Form Cost Trade Study," Idaho National Laboratory, Idaho Falls, ID, (2008).

[40] J. V. Crum, B. J. Riley, and T. L. R., "Summary Report: Glass-Ceramic Waste Forms for Combined Fission Products," Pacific Northwest National Laboratory, Richland, WA (2011).

[41] J. Crum, V. Maio, J. McCloy, C. Scott, B. Riley, B. Benefiel, *et al.*, "Cold crucible induction melter studies for making glass ceramic waste forms: A feasibility assessment," *Journal of Nuclear Materials,* **444** 481-492 (2014).

[42] M. R. Asmussen, J. J. Neeway, T. C. Kaspar, and J. V. Crum "Corrosion Behavior and Microstructure Influence of Glass-Ceramic Nuclear Waste Forms" *Corrosion Science Section*, **73** [11] 1306-1319 (2017).

[43] D. Caurant, O. Majérusa, E. Fadela, A. Quintasa, C. Gervaisb, T. Charpentierc, D. Neuvilled "Structural investigations of borosilicate glasses containing MoO_3 by MAS NMR and Raman spectroscopies" *Journal of Nuclear Materials* **396** 94–101 (2010).

[44] N. Chouard, D. Caurant, O. Majerus, J. L. Dussossoy, S. Klimin, D. Pytalev, R. Baddour-Hadjean, J. P. Pereira-Ramos. "Effect of MoO_3, Nd_2O_3, and RuO_2 on the crystallization of soda–lime aluminoborosilicate glasses," *J. Mater. Sci.,* **50** 219–241 (2015).

[45] A. Brehault, D. Patil, H. Kamat, R. E. Youngman, L. M. Thirion, J. C. Mauro, C. L. Corkhill, J. S. McCloy, and A. Goel. "Compositional Dependence of Solubility/Retention of Molybdenum Oxides in Aluminoborosilicate-Based Model Nuclear Waste Glasses," *The Journal of Physical Chemistry B* **122** [5] 1714-1729 (2018).

[46] K. Brinkman, K. Fox, J. Marra, J. Reppert, J. Crum, and M. Tang, "Single phase melt processed powellite $(Ba,Ca)MoO_4$ for the immobilization of Mo-rich nuclear waste," *Journal of Alloys and Compounds,* **551** 136-142 (2013).

VITA

Nicholas Stephen Roberts, son of Andrew and Julia Roberts, was born December 4, 1993 in New Hartford, NY. He earned a diploma from Holland Patent Central High School in June 2012. He enrolled at Alfred University in August 2012. He was a member of Materials Advantage, Keramos, and served on the American Ceramic Society's President's Council of Student Advisors from 2014-2015. He graduated with Honors in May 2016 with a B.S. in Materials Science and Engineering from Alfred University.

In June of 2016, he joined the research group of Dr. Richard K. Brow at Missouri University of Science and Technology in Rolla, MO, to pursue his M.S degree in Materials Science and Engineering. His work concentrated in characterizing borosilicate glass-ceramics for waste vitrification which was funded by the Department of Energy and the Nuclear Energy University Program (Project 15-8112). He presented his work at three international conferences and was awarded the Summer Graduate Research Fellowship in 2018. Nicholas received his M.S. in Materials Science and Engineering in December 2018 from Missouri University of Science and Technology.